APPLICATION OF PHASE ESTIMATION ALGORITHMS TO IMPROVE DIAMOND SPIN MAGNETOMETRY

by

Naufer Mohamed Nusran

BSc, University of Colombo, 2006

MS, University of Pittsburgh, 2008

Submitted to the Graduate Faculty of

the Dietrich School of Arts and Sciences in partial fulfillment

of the requirements for the degree of

Doctor of Philosophy

University of Pittsburgh

2014

UNIVERSITY OF PITTSBURGH

DEPARTMENT OF PHYSICS AND ASTRONOMY

This dissertation was presented

by

Naufer Mohamed Nusran

It was defended on

February 24, 2014

and approved by

Gurudev Dutt, Ph.D. (Physics)

Brian D'Urso, Ph.D. (Physics)

Paul Shepard, Ph.D. (Physics)

Robert Coalson, Ph.D. (Chemistry)

Robert Griffiths, Ph.D. (CMU)

Dissertation Director: Gurudev Dutt, Ph.D. (Physics)

APPLICATION OF PHASE ESTIMATION ALGORITHMS TO IMPROVE DIAMOND SPIN MAGNETOMETRY

Naufer Mohamed Nusran, PhD

University of Pittsburgh, 2014

Precision measurements of weak magnetic fields with nanoscale spatial resolution is an outstanding challenge in many fields including medicine, biology, material science and physical science. It has already been demonstrated that a single electronic spin formed by a defect color center in diamond, known as the nitrogen-vacancy (NV) center, can serve as a highly sensitive magnetometer with nanoscale resolution, even under ambient conditions. However, standard quantum sensing methods have significant drawbacks. These include the limited dynamic range due to quantum phase ambiguity, the non-linearity in sensitivity over the detectable field range, the requirement of prior knowledge of a working point for accurate deconvolution, etc. This thesis explores novel quantum control techniques such as the use of phase estimation algorithms (PEA) for magnetic field detection to address these issues. Unlike in the standard approach, PEA readout is linearly dependent on the field being sensed. PEA employed on oscillating (AC) magnetic fields can not only detect unknown field amplitudes but also allows detection of the field phase. The thesis also compares the performance of nonadaptive-PEA (NAPEA) with that of adaptive-PEA (QPEA) and conclude that NAPEA is superior to QPEA due to (a) better sensitivity on average, (b) consistency in sensitivity throughout the full field range, (c) comparatively less demanding measurement fidelity, and (d) for simplicity in its experimental realization. The techniques developed here can potentially have broad applicability to a wide variety of solid-state quantum systems and in the field of quantum control and measurement.

TABLE OF CONTENTS

LIST OF TABLES

LIST OF FIGURES

ACKNOWLEDGEMENT

Foremost, I would like to express my sincere gratitude to my advisor Dr. Gurudev Dutt for the continuous support for my PhD research, for his motivation, enthusiasm, and guidance. I am very lucky to be his first doctoral student and hence was privileged to learn and gain tremendous experience when it comes to setting up a new research laboratory.

I would like to thank my respectable thesis committee: Dr. Brian D'Urso, Prof. Paul Shepard, Prof. Robert Coalson, and Prof. Robert Griffiths. Their insightful comments, valuable suggestions, encouragement, and hard questions have greatly improved my abilities and my research.

I thank my fellow lab-mates including Kai, Peng, Bradley, and Jonathan and all my friends at the University of Pittsburgh, for the stimulating discussions and for all the joy we have had in the last few years. I also thank my father Mr. S.M. Naufer, my mother Mrs. Haleemath Sahithiya, my wife Safwa Faiz, and my siblings for all the encouragement and the spiritual support rendered during my PhD. Without the company of my family and friends, I cannot imagine how tough it would be to cope with difficult and stressful times.

And last but not the least, I thank the administration of the Physics department at the University of Pittsburgh for being supportive in all administrative matters. I cannot forget to mention the support from the graduate secretary Ms. Leyla Hirschfeld, for ensuring my progress towards the PhD in many different ways.

LIST OF PREVIOUSLY PUBLISHED WORK

A portion of chapter 2 and most of chapter 3 has been submitted to Phys.Rev.B for publication, and is available in arXiv.org

"Optimizing phase estimation algorithms for diamond spin magnetometry", N. M. Nusran and M. V. Gurudev Dutt, http://arxiv.org/abs/1403.4506

Chapter 4 and Appendix D appeared entirely in the following paper and its supplementary on-line material.

"High-dynamic-range magnetometry with a single electron spin in diamond", N. M. Nusran and M. Ummal Momeen and M. V. Gurudev Dutt, Nature Nanotech. **7**, 109 (2012)

Chapter 5 and Appendix E appeared entirely in the following paper and its supplementary on-line material.

"Dual-channel lock-in magnetometer with a single spin in diamond", N. M. Nusran and M. V. Gurudev Dutt, Phys. Rev. B, **88**, 220410 R (2013)

LIST OF ACRONYMS AND SYMBOLS

AFM : Atomic force microscope

AO : Atomic orbital

CCD : Charged-coupled device

CLT : Central limit theorem

CVD : Chemical vapour deposition

CW : Continuous wave

DC Magnetometry : Sensing static magnetic fields

DNP : Dynamic nuclear polarization

DR : Dynamic range

ESR : Electron spin resonance

IR : Irreducible representation

LAC : Level anti-crossing

MLE : Maximum likelihood estimate

MO : Molecular orbital

MOKE : Magneto-optic Kerr effect

MRFM : Magnetic resonance force microscope

MW : Microwave

MZI : Mach-Zehnder interferometer

NA : Numerical aperture

NAPEA : Non-adaptive phase estimation algorithm

NMR : Nuclear magnetic resonance

NV : Nitrogen-vacancy

ODMR : Optically detected magnetic resonance

PEA : Phase estimation algorithm

QNM : Quantum network model

QPEA : Quantum phase estimation algorithm

SIL : Solid immersion lens

SPDM : Scanning diamond probe microscope

SQUID : Superconducting quantum interference device

SEM : Scanning electron microscope

SMS : Standard measurement sensitivity

SNR : Signal to noise ratio

TEM : Transmission electron microscope

Ω : Rabi frequency

Φ : Control phase

ϕ : Quantum phase

θ : AC magnetic field phase

η : Magnetic field sensitivity

T_2^* : Dephasing time in the Ramsey experiment

T_2 : Decoherence time in the Hahn-echo experiment

χ^2 : Chi-squared value

χ^2_{red} : Reduced chi-squared (goodness of fit)

1.0 INTRODUCTION

Quantum sensors in robust solid-state systems offer the possibility of combining the advantages of precision quantum metrology with nanotechnology. Quantum electrometers and magnetometers have been realized with superconducting qubits[1], quantum dots[2], and spins in diamond[3, 4, 5, 6]. These sensors could be used for fundamental studies of materials, spintronics and quantum computing as well as applications in medical and biological technologies. In particular, the electronic spin of the nitrogen-vacancy (NV) color center in diamond has become a prominent quantum sensor due to optical transitions that allow for preparation and measurement of the spin state, stable fluorescence even in small nanodiamonds[7], long spin lifetimes[8], biological compatibility[9, 10] as well as available quantum memory that can be encoded in proximal nuclear spins[11, 12]. This chapter gives an overview to on-going research and achievements on NV center based nanotechnology, and compares with other nanoscale magnetometry technologies. The organization of the rest of the thesis is described in the end of the chapter.

1.1 DIAMOND SPIN BASED NANOTECHNOLOGY

Due to the atomic length scale in size, the NV color center is promising for sensitive measurements with nanoscale spatial resolution. In fact, nanoscale electrometry[6], thermometry[13, 14, 15] and magnetometry[3, 5, 16, 17] applications have already been demonstrated with NV center. Here, we exclusively discuss the improvement in nanoscale magnetometry while other metrological applications are beyond the scope of this thesis.

The first demonstrations of NV center for magnetometry applications were performed

in 2008, by Balasubramanian *et al* (Ref.[5]) for the static (DC) field, and by Maze *et al* (Ref.[3]) for oscillatory (AC) fields. Since then, significant focus towards improving the magnetic field sensitivity has been made, by either by use of high-quality diamond probes[8], or by application of dynamic-decoupling (DD) techniques[18, 19, 20, 1, 21, 22, 23]. For instance, in Ref.[8], an AC magnetic field sensitivity of $\sim$ 4 nT/$\sqrt{Hz}$ was demonstrated with the use of ultra-pure isotopically controlled single-crystal chemical vapor deposition (CVD) diamond probes.

Another direction of NV magnetometry research, focuses on 'engineering' improved diamond probes[8, 24, 25, 26, 27, 28]. A significant direction has been towards enhancing the photon detection efficiency, which can in turn improve the sensitivity of the diamond sensor. For instance, improved photon detection efficiency was achieved by 'side-collection' optical waveguide technique[28], fabrication of solid immersion lenses (SIL)[29, 30, 31], fabrication of diamond nano-pillars[32, 33, 34], and fabrication of plasmonic aperture[35].

The ultimate goal is, however, to achieve nanoscale magnetic imaging of unknown entities. As a step towards this goal, several attempts have been made in realizing a scanning diamond probe microscope (SDPM)[17, 36]. Figure 1 depicts a typical schematic of such an imaging system. The diamond probe tip could either be fabricated out of diamond[37] or simply formed by gluing a diamond nano-crystal onto a tip of an atomic force microscope (AFM)[38]. In Ref.[17], magnetic imaging of a target NV electronic spin, was demonstrated with use of an SPDM. The distance between target spin and the probe spin here was $\sim$ 50 nm, whereas the best sensitivity achieved was $\sim$ 18 nT/$\sqrt{Hz}$. Sensing the existence of 'dark' electron spins was recently demonstrated in Ref.[39].

Other interesting works include nuclear magnetic resonance (NMR) on a nanoscale volume[40, 41], tracking of fluorescent nanodiamonds inside living cells[10], optical magnetic imaging of living cells[42], magnetic field imaging with NV ensembles[43], and stray-field imaging of magnetic vortices[44]. However, when it comes to quantum sensing, the best precision typically demands a limited dynamic range, i.e.: the maximum possible field strength (B_{max}) has to be less than the sensor's spectral linewidth[45, 46]. Otherwise, a trade-off with the precision occurs, caused by increasing the measurement bandwidth and thus reducing the signal to noise ratio (SNR). This thesis explores the use of phase estimation algorithms

(PEA) with NV centers, in order to address these problems and thereby achieve improved magnetometry. The results of this work have been published in Refs.[16, 47, 48].

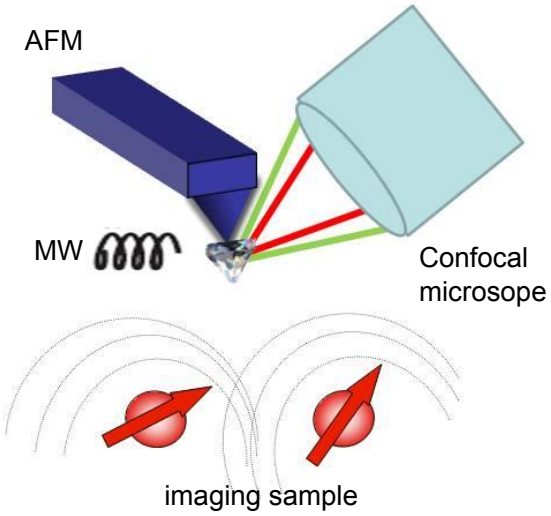

Figure 1: Schematic of a SPDM. A diamond nanocrystal with a NV is attached to the AFM tip. Confocal microscope is used for initialization and readout of the NV spin while microwave for NV spin manipulation. The diamond-probe can sense the magnetic fields from other spins in the sample and thereby construct a magnetic image with nano-scale spatial resolution.

1.2 COMPARISON BETWEEN EXISTING TECHNOLOGIES

Vapor-based atomic magnetometers are currently the most sensitive devices ($\sim$ fT/$\sqrt{Hz}$) when it comes to centimeter and longer length scale[49, 50, 51]. The basic principle here is the detection of the Faraday rotation of linearly polarized light through a magneto-optic vaporous medium. However, nano-scale spatial resolution is not possible with vapor-based technique, due to thermal motion of the atoms. The optimal operation of atomic magnetometers requires them to be heated to well above room-temperature, and hence limits the range of applications. A solid state version of a similar principle have also been explored wherein magneto-optic Kerr effect (MOKE) causes Faraday rotation of the reflected light from a magneto-optic medium[52, 53]. The sensitivity of MOKE is not as good as the vapor

based method, however, a spatial resolution of micrometer length scale is possible. Nano-scale spatial resolution is not possible with MOKE technique because it is fundamentally limited by the optical resolution. Electron microscopies have also been explored for magnetic imaging[54, 55, 56, 57, 58]. The scanning electron microscope (SEM) gives information of the sample surface whereas transmission electron microscope (TEM) gives information of the sample volume. Spin polarization of secondary electrons from the magnetic sample in SEM can give topographic information of ferromagnetic samples whereas deflection analysis of transmitted electrons in TEM can give information on magnetic domains of the sample. However electron microscopic techniques are relatively invasive due to the bombardment of energetic electrons. Also due to charging effect and the requirement of vacuum, the range of applications is highly limited.

Currently explored most sensitive solid-state devices make use of quantum interference in superconducting quantum interference devices (SQUIDs)[60, 61, 62, 63, 1], the Hall effect in semiconductors[64] and novel avenues such as magnetic resonance force microscopy (MRFM)[65, 66, 67, 68]. In the case of SQUIDs, although better sensitivity than $\sim$nT/$\sqrt{Hz}$ is possible, the operating temperature is however cryogenic, limiting the range of applications. MRFM, a combination of magnetic resonance imaging and scanning probe microscopy, is currently the leading nano-scale magnetic sensing device with impressive spatial resolution and yet requires cryogenic environments making impractical for the most biological applications. Figure 2 shows the state of the art for current implementations of solid-state magnetometers. The diamond spin sensor is competitive with the current leader in the area with the additional advantage of being able to operate under a wide range of temperature including ambient conditions.

1.3 THESIS OVERVIEW

The thesis is organized as follows:

Chapter 2 provides an overview on the Nitrogen-Vacancy (NV) defect centers in diamond, confocal microscopy for localizing NV centers, the application of conventional electron spin

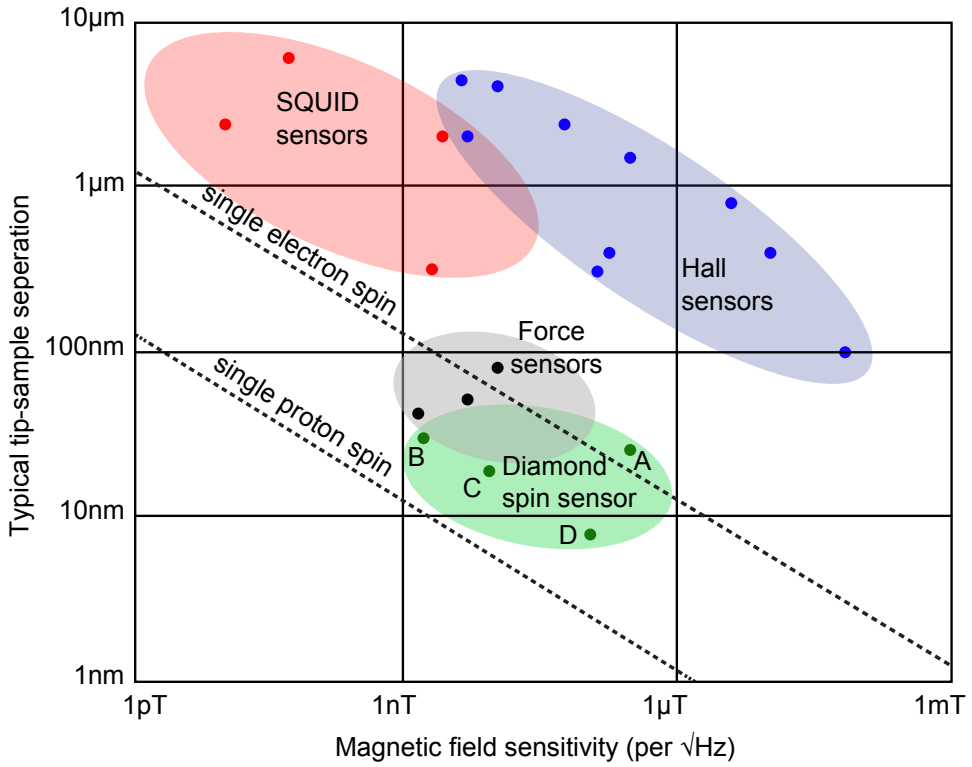

Figure 2: Comparison between magnetic field sensing techniques. The dots correspond to different experimental works. The two dashed lines show magnetic fields due to single electron and proton respectively. For the time being, only the force sensors and the diamond spin sensors have reached the capability to sense single electron spins. Labels A,B,C, and D correspond to values obtained from Refs.[59],[8],[17], and [41] respectively.

resonance (ESR) techniques for quantum control of NV, and magnetometry with NV.

Chapter 3 presents a detailed theoretical and numerical optimization of phase estimation algorithms (PEA) for diamond spin magnetometry. We study the importance of control phases and their effect on the magnetic field sensitivity, as well as the dependence of sensitivity on dynamic range. The impact of dynamic range on nanoscale magnetic imaging is also described. We compare the non-adaptive phase estimation algorithm with a weighted quantum phase estimation algorithm incorporating error-checking. Finally, we introduce the application of PEA to oscillating field magnetometry, and demonstrate the usefulness in measuring both amplitude and phase of the AC magnetic field.

Chapter 4 describes implementation of PEA with the NV center in diamond to achieve high dynamic range DC magnetomtery while preserving the decoherence-limited sensitivity.

In chapter 5, we presents an experimental method to perform dual-channel lock-in magnetometry of time-dependent magnetic fields using NV centers. We incorporate multi-pulse quantum sensing sequences with PEA to achieve linearized field readout and constant, nearly decoherence-limited sensitivity over a wide dynamic range. Furthermore, we demonstrate unambiguous reconstruction of the amplitude and phase of the magnetic field.

Finally, chapter 6 provides a summary and concludes the thesis with a brief outlook to future directions.

2.0 BACKGROUND

2.1 NITROGEN-VACANCY DEFECT CENTER IN DIAMOND

The nitrogen-vacancy (NV) center is a point defect in the diamond lattice. It consists of a nearest neighbor pair of a substitutional nitrogen atom and a lattice vacancy (Figure 3a). When the center acquires an extra electron from other defects, it forms a $S = 1$ (spin triplet) system in its ground state. In this thesis, we exclusively consider the negatively charged NV and simply refer to it as the NV center.

The energy energy level structure is shown in Figure 3b. The labeling of these energy levels is due to standard notations in C_{3V} group symmetry operations[69]. Even in the absence of a background magnetic field, the $m_S = \pm 1$ levels are 2.87 GHz higher in energy than the $m_S = 0$ level. This is known as the zero field splitting and arises due to the zeroth order spin-spin interactions. A detailed review of the NV and its properties can be found in Refs.[70, 71, 72]. See Appendix A for a group theoretical approach to label the energy levels of NV by considering the C_{3V} symmetry.

The optical properties exhibited by the NV center includes a zero-phonon line (ZPL) at 637 nm associated with $A \leftrightarrow E$ dipole transition and a broad phonon emission side-band from 650 nm to 800 nm (Figure 3c). When subject to off-resonant optical excitation (532 nm laser), all the spin states exhibit mostly spin preserving cyclic transitions between $A \leftrightarrow E$. However, relaxation can also occur via the metastable singlet levels ($^1A_1$ and ^1E). The decay rate of the metastable state is slower ($\sim$ 300 ns) compared to the $A \leftrightarrow E$ transition rate ($\sim$ 10 ns), and the $m_S = \pm 1$ is relatively more probable to undergo relaxation via the metastable states. Therefore, $m_S = \pm 1$ give less fluorescence compared to the $m_S = 0$ level in the beginning of an optical excitation (Figure 4). Further because the $^1A_1$ level relaxes directly to $m_S = 0$

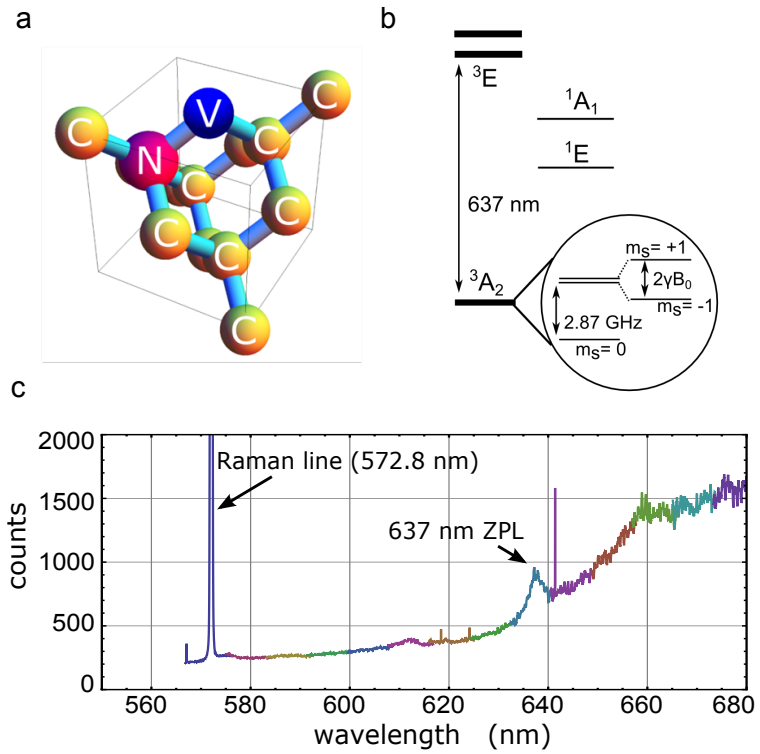

Figure 3: **a,** Crystal structure of diamond with (111) NV center **b,** Level structure of NV **c,** Photo-luminescence spectrum of NV.

level, through continuous optical excitation, the NV could be fully populated to the $m_s = 0$ level. This enables the ability for optical readout of the spin as well as optical initialization of the spin. Added to this, the fact that having longer spin life times ($T_1 \sim 10$ ms, $T_2^* \sim 2$ μs, $T_2 \sim 400$ μs) as a solid-state system, makes the NV a promising candidate for realizing the spin qubit concept in quantum information[73, 74, 12, 11]. Figure 4 data also allows to calculate fluorescence counts per optical measurement pulse, α_0 (α_1) corresponding to the sate $|m_S = 0\rangle$ ($|m_S = -1\rangle$) by integrating the counts over the shaded region.

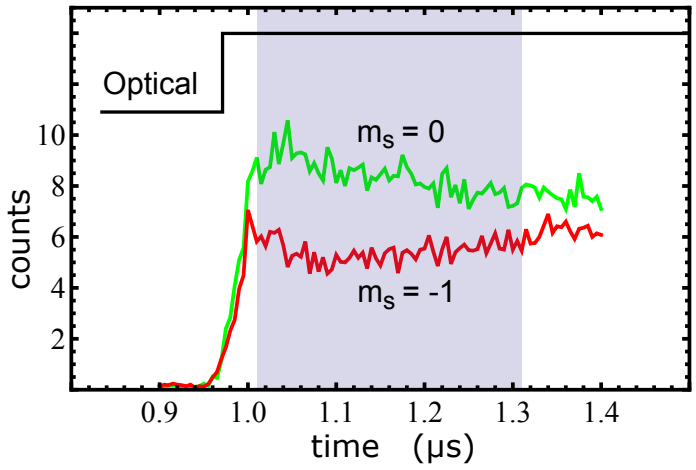

Figure 4: Photons in the wavelength range $600 - 800$ nm are counted with respect to the duration of optical excitation, for initial spin states $m_S = 0$ and $m_S = -1$. Total counts in the shaded region, known as the "signal window", is highly dependant on the spin state.

2.2 CONFOCAL MICROSCOPY AND DETECTION OF NV CENTERS

The conventional method of isolating NV centers is achieved by obtaining an image of a diamond sample through a confocal fluorescence microscope. The key idea of a confocal microscope is to use point illumination and a spatial pinhole to eliminate out-of-focus light in specimens and thereby increases the contrast of weakly fluorescing points. The action of the pinhole in our confocal set-up (Figure 5) is performed by an optical fiber in the collection path. A 532 nm green laser is used for illumination and galvanometer scanning mirrors could scan the beam direction, thereby illuminating different regions on the diamond sample. A high numerical-aperture (NA) objective is held on a piezoelectric stage which controls the depth of focus. The function of dichroic beam splitter in Figure 5 is to reflect the 532 nm excitation laser but transmit the rest of the light. However, there could be some leakage of the 532 nm through the dichroic beam splitter which can result in a poorer signal to noise ratio (SNR) of the fluorescence image. In order to further suppress this leaked light, we introduce a 532 nm notch filter in the collection path. Other optical filters (600-800 nm band pass) can also be introduced in the collection path to select light in the NV emission

spectrum in order to improve the SNR of our fluorescence image. More details on the design of the confocal microscope including various calibration/test schemes can be found in Appendix B. See Appendix F for a detailed list of instruments/components used in the overall experimental apparatus.

The illumination laser beam has a Gaussian cross section in intensity given by,

$$I(r) = I_0 e^{-2r^2/w^2} \tag{2.1}$$

where r, and w are the radial distance, and the beam waist size respectively[75]. The optimum waist size for the illumination beam is when it equals the objective pupil radius. An over-filled pupil loses much of the illumination light and also introduces some diffraction pattern on the focusing plane whereas an under-filled pupil spoils the resolution at the focusing plane. At the optimum condition where the beam waist matches the objective pupil radius[76], the radial r and depth z diffraction limited resolution due to the objective lens is given by,

$$\Delta r = 0.61\lambda/NA \tag{2.2}$$

$$\Delta z = 1.5\lambda n/NA^2 \tag{2.3}$$

where λ is the illumination wavelength, n is the refractive index of the medium of focus and NA is the numerical aperture of the objective. This is basically the dimension of the diffraction limited illumination spot. The overall resolution of a confocal system is however, slightly better than the above limit, because it is effectively a convolution of the point spread functions of the objective lens with of a pinhole[76].

Because NV is a single photon emitter, identifying single NV centers could be done by performing an auto-correlation measurement on a Hanbury-Brown and Twiss setup (Figure 6). The second order auto-correlation function is given by

$$g^{(2)}(\tau) = \frac{\langle n_1(t) n_2(t+\tau)\rangle}{\langle n_1(t)\rangle \langle n_2(t+\tau)\rangle} \tag{2.4}$$

where τ is the time interval between the both detection. For a single-mode in a number state $|n\rangle$, the auto-correlation function at $\tau = 0$ could be reduced to $g^{(2)}(0) = 1 - 1/n$ where n is input photon number[77]. Therefore ideally, a single photon state gives $g^{(2)}(0) = 0$ whereas

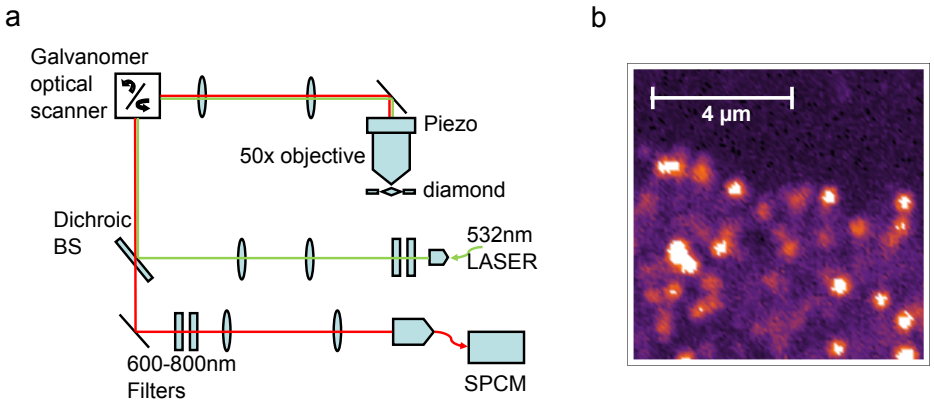

Figure 5: **a,** Schematic of confocal microscope. See Appendix F for more details on the components. **b,** A confocal microscopic image. Bright spots show more florescence. A single NV in our system, typically gives 60-70 kHz photon counts.

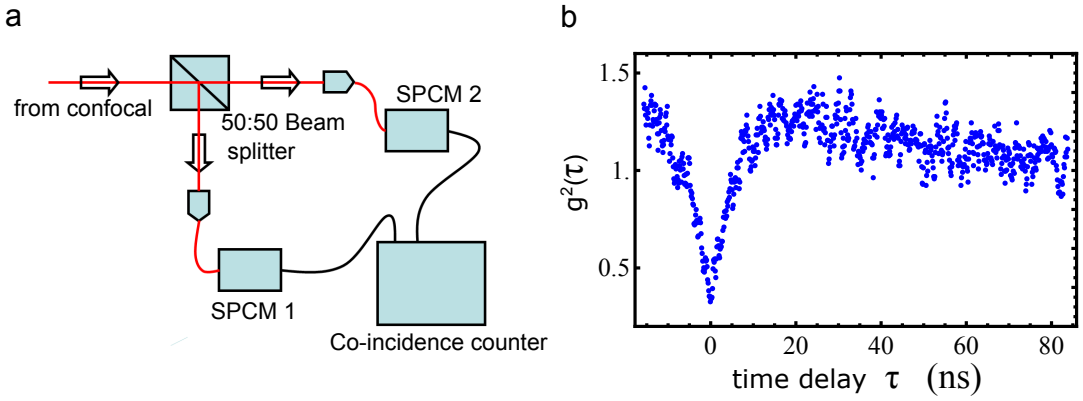

Figure 6: **a,** Schematic of Hanbury-Brown and Twiss setup **b,** Photon anti-bunching is observed at zero delay time from a single NV center.

as two-photon state gives $g^{(2)}(0) = 1/2$. However the thermal background emission may cause an additional contribution to the measured $g^{(2)}(0)$ value. Therefore, a measurement of $g^{(2)}(0) < 0.5$ is sufficient to identify a single NV center.

2.3 OPTICALLY DETECTED MAGNETIC RESONANCE (ODMR)

Recall that $m_S = \pm 1$ states show less fluorescence compared to the $m_S = 0$ level and continuous off-resonant optical excitation fully polarizes the NV into $m_S = 0$ level. Also one could introduce a background constant magnetic field to Zeeman split the $m_S = \pm 1$ levels. Continuous optical and microwave (MW) excitation but varying the MW frequency allows to map out the energy levels, because the maximum change in fluorescence occur at resonant conditions for the transitions: $m_S = 0 \leftrightarrow m_S = -1$ and $m_S = 0 \leftrightarrow m_S = +1$. Figure 7a shows an example of such a continuous-wave (CW) ESR spectrum when the background magnetic field along NV axis is ~ 23 G. A zoomed-in view of the dip corresponding to the transition $m_S = 0 \leftrightarrow m_S = -1$ ($f_0 \approx 2.806$ GHz) is given in the inset figure. This clearly shows additional splitting which arises due to hyperfine interaction between electronic spin and the ^{14}N nuclear spin. The red solid line gives the best fit of three Lorentzian curves centered on $\sim f_0$, and $\sim f_0 \pm 2.2$ MHz respectively. The effective ground state Hamiltonian of the NV here can be written as,

$$H = \Delta S_z^2 - \gamma_e \vec{S}.\vec{B} + \vec{S}.\overleftrightarrow{A}.\vec{I} \tag{2.5}$$

$$\approx \Delta S_z^2 - \gamma_e S_z B_0 + A_\parallel S_z I_z + A_\perp (S_x I_x + S_y I_y) \tag{2.6}$$

where $\Delta = 2.87$ GHz is the zero-field splitting, $\gamma_e \approx 28$ GHz/T and $\overleftrightarrow{A}$ is a tensor that quantifies the hyperfine interaction between the electronic spin state and the nitrogen nuclear spin states. The axial and transverse hyperfine constants are $A_\parallel \approx -2.2$ MHz and $A_\perp \approx -2.7$ MHz respectively[78, 79]. The axial hyperfine constant $A_\parallel$ is what causes the hyperfine structure in the Figure 7a inset.

In order to recover the hyperfine structure, it is required that resonance linewidth (δf) be smaller than the hyperfine energy gap; i.e., $\delta f < 2.2$ MHz. Such sharp line widths can be easily obtained by pulsed ESR techniques. Figure 7b (top) illustrates the typical experimental procedure for a pulsed ESR experiment with NV. Here, a MW pulse sequence is sandwiched between two optical excitation pulses. The initial optical excitation polarizes the NV into $|m_S = 0\rangle$ while the final excitation is for the spin readout. The counting for photons are performed at two different times known as the counting windows. The photon

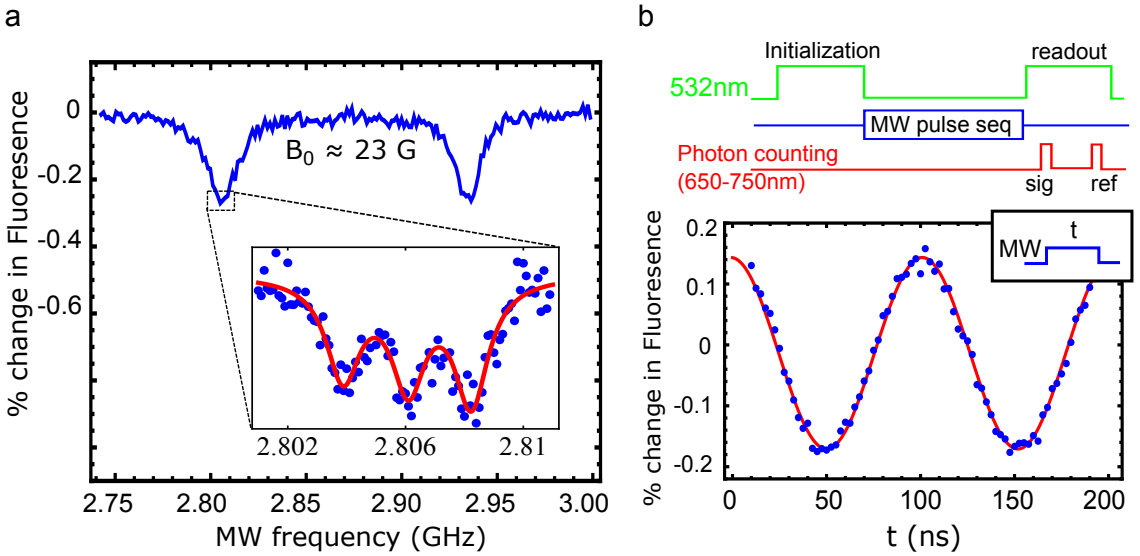

Figure 7: **a,** CW-ESR signal. The two dips correspond to transitions $m_S = 0 \leftrightarrow m_S = \pm 1$ of an NV. The inset shows the additional splitting due to hyperfine interaction. **b,** (top) Procedure for pulse-ESR experiments.(bottom) MW tuned to transition between $m_S = 0 \leftrightarrow m_S = -1$ induces Rabi oscillations between those states.

counts in the 'sig' window is highly dependent on the NV spin state just before the readout optical excitation. Photon counting in the 'ref' window has two functions; Firstly, taking the percentage difference of 'sig' counts with respect to 'ref' counts can minimize the effect of laser power fluctuations on the spin readout. Secondly, 'ref' counts enables to detect sample drifts which causes significant reduction in the photon counts. This indicates that the data collection should be temporarily paused until the NV is brought back to focus. The data in the bottom shows an example of a pulse-ESR experiment where a single MW pulse resonant with the transition $m_S = 0 \leftrightarrow m_S = -1$ is used here. The signal as a function of MW pulse duration shows Rabi nutations in which the florescence oscillates between two fixed levels corresponding to $|m_S = 0\rangle$ and $|m_S = -1\rangle$ states respectively. This allows to calibrate our MW π-pulse[1].

[1]The data in Figure 7b correspond to a Rabi frequency $\Omega \sim 10$ MHz. Such Rabi frequencies in our system could be achieved with a MW power $\sim 30 - 40$ dBm (~1-10 W) delivered to the micro-wire, depending on the proximity of the NV to the micro-wire. Caution should be taken in handling such high MW powers. Note that, even a MW power of 1 Watt, can still cause harm to the circuit, if it is in the CW mode.

In general, pulsed mode ESR experiments lead to better signal-to-noise ratio (SNR) compared to experiments with CW mode, because the noise contribution from the optical and MW driving sources are minimized. The inset figure in Figure 7a was in fact obtained in the pulse mode. First we perform on resonance Rabi oscillations with frequency $\Omega << 2.2$ MHz that corresponds to a long π-pulse time, $t_\pi = \pi/2\Omega$. Then we perform the experiment as in Figure 7b as the MW frequency is varied but the duration of the MW pulse is fixed to t_π. This allows to recover the superfine splitting because the linewidth of signal spectrum is given by the Rabi frequency Ω and is chosen to be far less than 2.2 MHz. To understand the exact origin of this linewidth, consider the dynamics of an ideal two level system which is initially in state 1. The transition probability from the initial state to the second state is given by,

$$P_{1\to 2}(t) = \frac{\Omega^2}{\Omega^2 + \delta^2} \sin^2 \left[\frac{\sqrt{\Omega^2 + \delta^2}}{2} t\right] \tag{2.7}$$

where $\delta = \omega - \omega_0$ is the detuning of the MW frequency ω with respect to the resonant frequency ω_0 between the two levels. If the MW duration time is fixed to t_π the signal as a function of the MW frequency is roughly proportional to

$$S(\omega) \sim \frac{\Omega^2}{\Omega^2 + (\omega - \omega_0)^2} \tag{2.8}$$

This is in fact a Lorentzian function with linewidth Ω. The data in Figure 7a inset was achieved with a $t_\pi = 800$ ns that lead to a linewidth ~ 1 MHz[2].

2.3.1 Optically induced nuclear spin polarization

The excited state of the NV has a Hamiltonian similar to equation 2.5, however with a different zero field splitting $\Delta_{es} = 1.42$ GHz[80, 81]. Therefore, upon a background axial magnetic field $B_0 \approx 500$ G, the spin states $|m_S = 0\rangle$ and $|m_S = -1\rangle$ become almost degenerate. Moreover, the non-axial component of the hyperfine interaction $H_A^{ff} = A_\perp(S_x I_x + S_y I_y)$ could be identified in terms of ladder operators: $H_A^{ff} = A_\perp(S_+ I_- + S_- I_+)/2$ known as the flip-flop term, where $S_\pm = (S_x \pm iS_y)/2$ and $I_\pm = (I_x \pm iI_y)/2$. The flip-flop action combined with electronic spin polarization process via off-resonant optical pumping allows for

[2]A $t_\pi = 800$ ns corresponds to a Rabi frequency $\Omega = 0.625$ MHz, and could be achieved with a MW power ~ 10 dBm (~ 10 mW) delivered to the micro-wire.

the polarization of ^{14}N nuclear spin to $I_z = +1$ state. This is known as the dynamic nuclear polarization (DNP)[82] and is further clarified below.

Consider a nuclear spin state $|I_z = -1\rangle$. Due to the action of H_A^{ff}, electron-nuclear combined system will oscillate back and forth between $|m_S = 0, I_z = -1\rangle_{es} \leftrightarrow |m_S = -1, I_z = 0\rangle_{es}$ at the excited state. Off-resonant optical pumping however, will polarize the electron spin to $|m_S = 0\rangle$ while conserving the nuclear spin state; i.e., $|m_S = -1, I_z = 0\rangle_{es} \rightarrow |m_S = 0, I_z = 0\rangle_{gs} \rightarrow |m_S = 0, I_z = 0\rangle_{es}$. Again due to hyperfine flip-flop action the $|m_S = 0, I_z = 0\rangle_{es}$ oscillates back and forth with $|m_S = -1, I_z = +1\rangle_{es}$ whereas optical pumping brings $|m_S = -1, I_z = +1\rangle$ to $|m_S = 0, I_z = +1\rangle$. Therefore at magnetic fields near 500 G, continuous optical excitation can initialize the system to $|m_S = 0, I_z = +1\rangle_{gs}$ state. In Figure 8 we notice complete DNP under a magnetic field of 414 G.

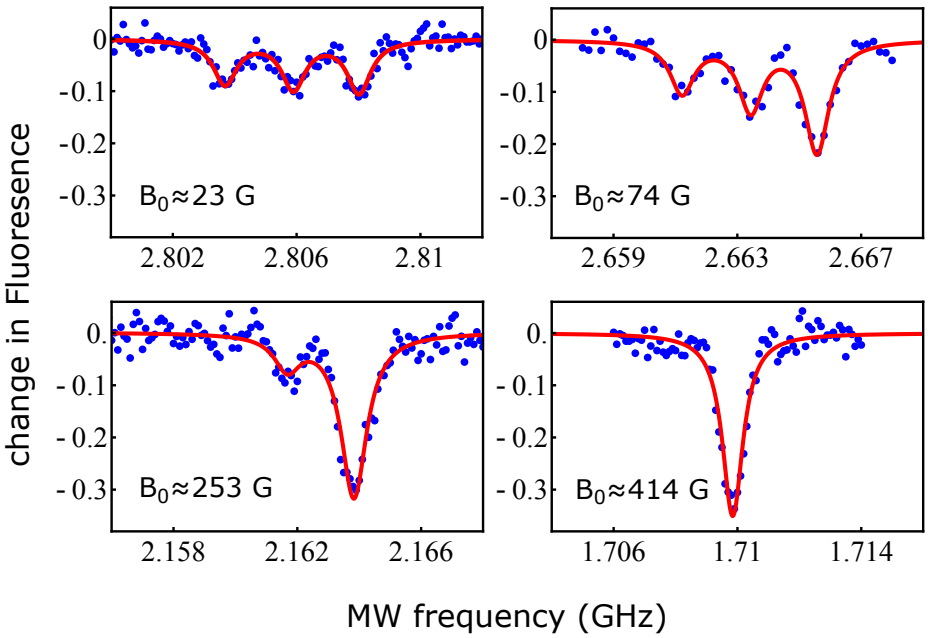

Figure 8: The hyperfine splitting in transition between $m_S = 0 \leftrightarrow m_S = -1$ at different axial background magnetic fields. At $B_0 \approx 23$ G the three nuclear spin state $I_z = 0, \pm 1$ are almost equally populated. At $B_0 \approx 253$ G $I_z = -1$ is completely suppressed. $I_z = +1$ is more populated than $I_z = 0$. At $B_0 \approx 414$ G, system completely polarizes to $I_z = +1$.

2.4 REALIZING QUANTUM GATES WITH THE NV

In previous section, we observed Rabi nutations wherein the florescence oscillates between two fixed levels (corresponding to $|m_S = 0\rangle$ and $|m_S = -1\rangle$ states) as the duration (t) of a MW-pulse (resonant with the transition between $|m_S = 0\rangle \leftrightarrow |m_S = -1\rangle$) is varied. Because this is a two level quantum problem, spin-1/2 physics could be used to describe the dynamics of the system. The overall Hamiltonian for the NV interacting with a dc bias magnetic field B_0, and the MW field B_{MW} is,

$$H \approx DS_z^2 - \gamma_e B_0 S_z + \gamma_e S_x B_{MW} \cos(\omega t + \Phi) \tag{2.9}$$

where, $D \approx 2.87$ GHz and $\gamma_e \approx 28$ GHz/T are the zero-field splitting and the gyromagnetic ratio of the spin respectively. Pulsed ESR experiments in such systems are best understood in the rotating frame of the MW rather than in the lab frame. In the rotating frame picture and rotating wave approximation (RWA), the Hamiltonian can be simplified to,

$$H^{RF} = \gamma_e \delta S_z + \gamma_e \Omega (S_x \cos\Phi + S_y \sin\Phi) \tag{2.10}$$

where Ω is the Rabi frequency, Φ is the phase of the MW field and $\delta = \omega - \omega_0$ is the detuning of the MW frequency ω with respect to the resonant frequency ω_0 between $|m_S = 0\rangle$ and $|m_S = -1\rangle$ levels. A Pauli-X gate on a the NV could be realized by simply introducing MW on resonantly ($\delta = 0$) with zero phase ($\Phi = 0$) for a half the period of Rabi oscillation, usually known as a MW π-pulse. MW switched-on for a quarter period of Rabi oscillation is a $\pi/2$-pulse and can be applied following the optical spin polarizing pulse, in order to transfer the NV spin population into an equal superposition between $|m_S = 0\rangle$ and $|m_S = -1\rangle$ states. In the presence of a non-zero detuning δ of the MW, free evolution on the state can cause rotations around the z-axis of the rotating frame[3], a Pauli-Z gate could also be also be realized. In fact the ability of X, Y and Z rotations allow for any single qubit gate operations. One could also employ the nuclear spin freedom of either the

[3]The detuning of the MW δ is typically chosen to be at least one-fifth smaller than the Rabi frequency Ω ie: $\delta < \Omega/5$

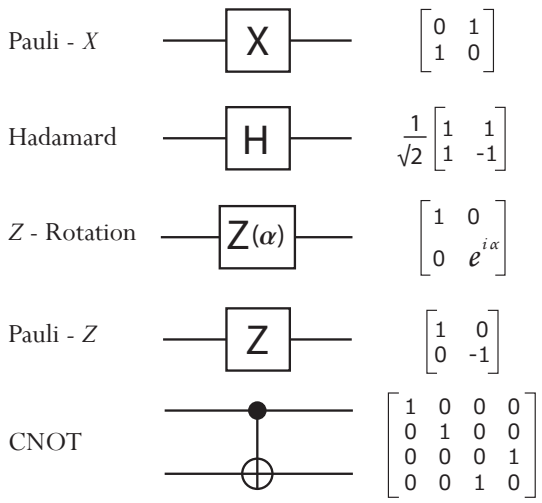

Figure 9: Some quantum gates realizable by the NV qubits and their matrix representation in the computational basis.

Nitrogen atom in the NV or a nearby ^{13}C that has a natural abundance $\sim 1.1\%$ for a second qubit. Selective resonance can now be performed for achieving two qubit conditional gates. For instance, a nearby ^{13}C will further split the $|m_S = -1\rangle$ level in Figure 3b into two sub levels (corresponding to $I_z = \pm 1/2$) due to the hyperfine interaction between NV electronic spin and the ^{13}C nuclear spin states. No splitting occurs at the $|m_S = 0\rangle$ level. Now, defining the NV electronic state and the ^{13}C nuclear spin state as the first and the second qubit respectively, one could constitute four computational states in the following way: $|m_S = 0, I_z = +1/2\rangle \equiv |00\rangle, |m_S = 0, I_z = -1/2\rangle \equiv |01\rangle, |m_S = -1, I_z = +1/2\rangle \equiv |10\rangle$, and $|m_S = -1, I_z = -1/2\rangle \equiv |11\rangle$. By applying a MW π-pulse resonant with the transition between $|m_S = 0, I_Z = -1/2\rangle \leftrightarrow |m_S = -1, I_Z = -1/2\rangle$ for instance, one achieves $|01\rangle \leftrightarrow |11\rangle$ but remaining states being off-resonant with the MW drive are unaffected by the MW pulse[4]. Therefore this selective MW excitation, functions as a CNOT gate on the first qubit conditioned by the second. A two-qubit conditional quantum gate with a gate fidelity 0.9 was first demonstrated by F.Jelezko et al[11] and similar techniques have been used in many other

[4]Here, we assume that the energy gap due to hyperfine splitting Δ can be easily resolved given the Rabi frequency Ω. ie: $\Delta >> \Omega$

applications since then[12, 83, 84].

2.5 STANDARD TECHNIQUES OF MAGNETOMETRY WITH THE NV

2.5.1 Ramsey method for sensing static (DC) magnetic fields

The DC magnetic field sensing could be achieved by a Ramsey experiment which leads to a better sensitivity compared to other techniques such as absorption spectroscopy and modulation spectroscopy. This is because, the quantum system (NV electronic spin in this case) interacts with the external magnetic field in the absence of any optical or MW excitations and therefore the noise contribution from these sources on the overall signal is minimized. The first MW $\pi/2$-pulse (resonant with $|m_S = 0\rangle$ and $|m_S = -1\rangle$ transition) in the Ramsey sequence ($\pi/2 - \tau - \pi/2$) brings the state into a superposition:

$$|\Psi(0)\rangle = (|m_S = 0\rangle + |m_S = -1\rangle)/\sqrt{2} \tag{2.11}$$

This state evolves for a time τ under the influence of the Hamiltonian $H = -\mu.B_{ext}$.

$$|\Psi(\tau)\rangle = (|m_S = 0\rangle + e^{i\gamma_e B_{ext}\tau}|m_S = -1\rangle)/\sqrt{2} \tag{2.12}$$

The second $\pi/2$-pulse in the sequence transforms the relative phase into a population difference in $|m_S = 0\rangle$ and $|m_S = -1\rangle$ that could be optically detected. The occupational probability of $|m_S = 0\rangle$ is given by:

$$P(0) = [1 - D(\tau)\cos(\gamma_e B_{ext}\tau)]/2 \tag{2.13}$$

where, $\gamma_e \approx 28$ GHz/T is the gyromagnetic ratio of NV and $D(\tau)$ takes the dechorence into account. Therefore, by measuring the population in the state $|0\rangle$ allows to estimate the external DC magnetic field.

2.5.2 Echo based method for sensing oscillatory (AC) magnetic fields

Sensing the AC magnetic field can be performed by a spin-echo (Hahn-echo) sequence, which is essentially a Ramsey sequence with a π pulse in the very middle ($\pi/2 - \tau/2 - \pi - \tau/2 - \pi/2$). As before the action of the first $\pi/2$-pulse brings the state into a superposition, $(|m_S = 0\rangle + |m_S = -1\rangle)/\sqrt{2}$ and in the free evolution of the first half $|m_S = -1\rangle$ picks up a phase ϕ relative to $|m_S = 0\rangle$ due to the external magnetic field resulting in $(|m_S = 0\rangle + e^{i\phi}|m_S = -1\rangle)/\sqrt{2}$. Since the π-pulse in the middle flips the spin resulting in $(e^{i\phi}|m_S = 0\rangle - |m_S = -1\rangle)/\sqrt{2}$ after the second free evolution interval the system will be in $(e^{i\phi}|m_S = 0\rangle - e^{i\phi'}|m_S = -1\rangle)/\sqrt{2}$ where ϕ' is the relative phase accumulation in the second half of the interval. Therefore, the spin always ends up in the same state $(|m_S = 0\rangle - |m_S = -1\rangle)/\sqrt{2}$ provided that external magnetic field remains constant through out the spin-echo sequence and final $\pi/2$-pulse brings system back to $|m_S = 0\rangle$. Hence, for a completely static environment, the spin-echo signal would be unity regardless of the free interval time in an ideal system. This behavior enables to detect AC magnetic fields. For instance, choosing the wait time τ to be the period of the AC magnetic field and with careful choice of the initial phase of the AC field $b(t) = b_{ac}\sin(2\pi t/\tau)$, spin-echo signal becomes proportional to the probability of the NV being in $|m_S = 0\rangle$ state[3].

$$P(0) = (1 + D(\tau)\cos(2\gamma_e b_{ac}\tau/\pi))/2 \tag{2.14}$$

2.6 PHASE ESTIMATION ALGORITHM (PEA)

2.6.1 Quantum phase estimation algorithm (QPEA)

The quantum circuit diagram for the QPEA is given in Figure 10a. The Algorithm requires b number of unitaries $(U^p, p = 2^0, 2^1, ..., 2^{b-1})$ to be applied in order to obtain an estimation ϕ_{est} for the classical phase parameter ϕ , with b bits of precision. $e^{i\phi}$ is an eigenvalue of the unitary operator U. Each application of U is controlled by a different qubit which is initially prepared in the state of $|+\rangle = (|0\rangle + |1\rangle)/\sqrt{2}$ and the control introduces a phase

shift $e^{ip\phi}$ on the $|1\rangle$ component. Measurement takes place in the σ_x basis (X) and the results control the additional phase shifts (control phases Φ) indicated by $R(\Phi) = |0\rangle\langle 0| + e^{i\Phi}|1\rangle\langle 1|$ on subsequent qubits. This basically enables performing the quantum Fourier transforms without using two-bit or entangled gates[85, 86, 87].

The QPEA could be realized with the NV as follows: An initial green pulse polarizes followed by a MW $\pi/2$-pulse prepares the the NV to the desired superposition state, $|+\rangle = (|m_S = 0\rangle + |m_S = -1\rangle)/\sqrt{2}$. The unitary phase operation U^{2^k} is simply achieved by a free precession interval t_k: $t_k = 2^{k-1} \times t_{min}$ where $k = 1, 2, ..., K$. The phase accumulated is proportional to the external magnetic field: $\phi_k = \gamma_e B_{ext} t_k$. The last $\pi/2$ will transform the information of the phase accumulated in $|m_S = -1\rangle$ with respect to $|m_S = 0\rangle$ into a population difference of the states. By comparing the measured signal level with a predefined threshold value, the bit u_m is determined to be either "0" or "1". This is equivalent to the X-basis measurement in the QPEA. The feedback rotations Φ are simply achieved by controlling the phase of the last MW $\pi/2$-pulse.

2.6.2 Non-adaptive phase estimation algorithm (NAPEA)

Figure 10b illustrates the quantum circuit diagram for the NAPEA. Here, the control phase Φ does not dependant on the previous measurement results. However the number of measurements vary as a function of k: $M(K, k) = M_K + F(K - k)$. Further the control phase alternates between $\Phi = \{0, \pi/2, \pi, 3\pi/2\}$ after each measurement. The conditional probability of the measurement is given by:

$$P(u_m|\phi, k) = \frac{1 \pm e^{-(t_k/T_2^*)^2} \cos(\phi_k - \Phi)}{2} \tag{2.15}$$

Now, the Bayes' rule can be used to find the conditional probability for the phase given the next measurement result:

$$P(\phi|\vec{u}_{m+1}) \propto P(u_{m+1}|\phi) P(\phi|\vec{u}_m) \tag{2.16}$$

where, $P(\phi|\vec{u}_m) \equiv P_m(\phi)$ is the likelihood function which is flat initially but gets updated after each measurement. Finally, the maximum likelihood estimator of the latest likelihood

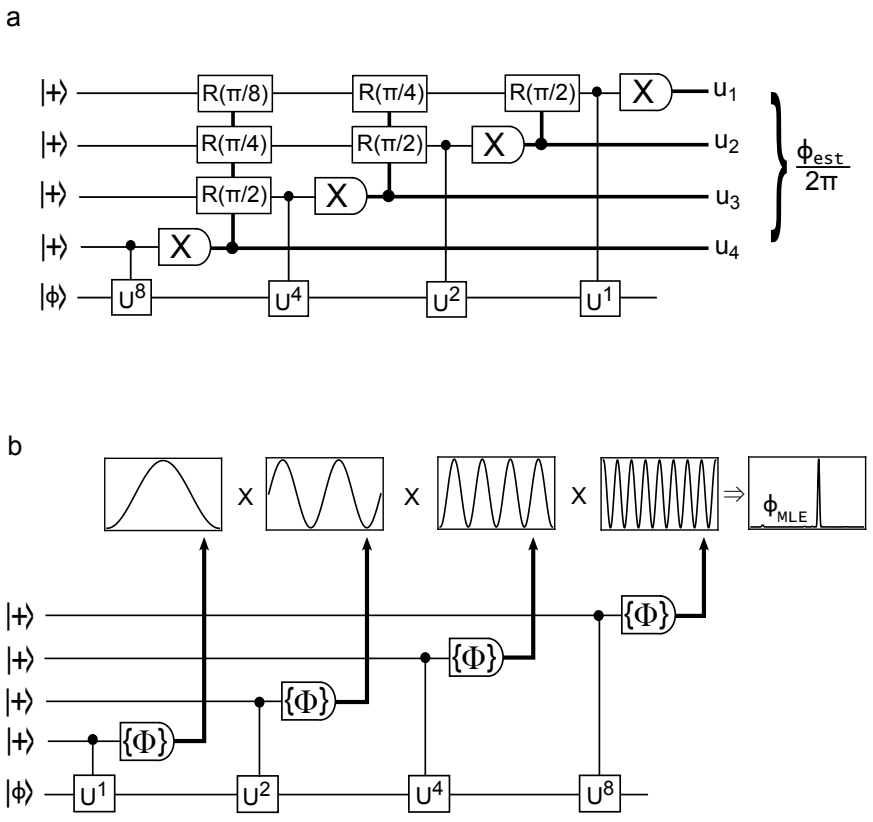

Figure 10: **Quantum circuit diagrams: a,** QPEA **b,** NAPEA for the case K=4. The dark lines represent the classical bits. The measured bit string in QPEA it self gives an estimate ϕ_{est} for the unknown phase with u_1 being the least significant bit. The control rotations $R(\Phi)$ in QPEA depends on preceding measurement results. In contrast, measurements in NAPEA are performed with a pre-defined set of control phases $\{\Phi\}$ and Bayes' method is used to obtain ϕ_{MLE}.

function (ϕ_{MLE}) is obtained as the best estimator for the unknown phase[88, 89, 90]. A detailed study with Monte-Carlo simulations on both types of PEA is presented in Chapter 3.

3.0 OPTIMIZING PHASE ESTIMATION ALGORITHMS FOR DIAMOND SPIN MAGNETOMETRY

3.1 INTRODUCTION

The essential idea of quantum probes is to detect a frequency shift $\delta\nu$ in the probe resonance caused by the external perturbation to be measured. The standard method to do this with maximum sensitivity is the Ramsey interferometry scheme, which measures the relative phase $\phi = \delta\nu \times t$ accumulated by the prepared superposition of two qubit states $(|0\rangle + |1\rangle)/\sqrt{2}$. These states will evolve to $(|0\rangle + e^{-i\phi}|1\rangle)/\sqrt{2}$, and subsequent measurement along one of the two states will yield a probability distribution $P(\phi) \sim \cos(\phi)$ that is sinusoidally dependent on the phase, and hence the frequency shift $\delta\nu$ can be obtained. For NV centers the detuning $\delta\nu = \gamma_e B$ where $\gamma_e \approx 28$ GHz/T is the NV gyromagnetic ratio and B is the field to be measured.

The phase (or field) sensitivity is obtained by assuming that the phase has been well localized between the values $(\phi - \pi/2, \phi + \pi/2)$, where ϕ is the actual quantum phase value, and in practice to much better than this by making a linear approximation to the sinusoidal distribution. Thus, prior knowledge of the "working point" of the quantum sensor is key to obtaining the high sensitivity that makes the sensors attractive. When the actual phase ϕ is allowed to take the full range of values, then the quantum phase ambiguity (i.e. the multi-valued nature of the inverse cosine function) results in much larger phase variance than predicted by the standard methods. To overcome the quantum phase ambiguity, we require an estimator $\hat{\phi}$ that can achieve high precision (small phase variance) over the entire phase interval $(-\pi, \pi)$ without any prior information. In terms of field sensing, this translates to a high dynamic range for magnetometry, i.e. to increase the ratio of maximum field strength

(B_{max}) to the minimum measurable field (δB_{min}) per unit of averaging time. This would be a typical situation in most applications of nanoscale magnetometry and imaging, where unknown samples are being probed. In fact, as we show in Section 3.2.2, as the sensitivity increases, it will be increasingly difficult to image systems where there is more than one type of spin present, and errors in the NV position will result in significant errors in the mapping. Further, since Ramsey imaging results in only one contour of the field being mapped out in a given scan, the acquisition time is greatly reduced, and thus several images must be made to accurately reconstruct the position of the target spins.

Recently, phase estimation algorithms (PEA) were implemented experimentally with both the electronic and nuclear spin qubits in diamond to address and resolve the dynamic range problem. While we note that the theory for the nuclear spin qubit has been presented in Ref. [88], our work supplements this by applying the theory to the electronic spin qubit which is more commonly used for magnetometry. Some of the questions that we address in this work, and have not been studied earlier, include: (i) the importance of control phases in the PEA, (ii) the dependence of sensitivity on the control phases, (iii) the dependence of sensitivity on the dynamic range, (iv) the impact of measurement fidelity on the PEAs. We have also studied the application of the PEA to fluctuating field magnetometry, and demonstrate the usefulness in measuring both amplitude and phase of the AC magnetic field.

In Section 3.2, we present a brief introduction to the Ramsey interferometry and the importance of dynamic range in magnetic imaging. Section 3.2.3 introduces the two types of PEAs that we have compared in this work. Section 3.4 shows some of the important results we obtain through the simulations. This includes a discussion on the importance of control phases, weighting scheme, required measurement fidelity and the possibility of implementing PEA for phase-lockable AC magnetic field detection. Finally, Section 3.5 summarizes the conclusions.

Our theoretical simulations below assume typical numbers from the experiments of Ref. [16], but we shall discuss the consequences of improved experimental efficiency where appropriate. For clarity purpose, we shall use the notations $|0\rangle \equiv |m_S = 0\rangle$ and $|1\rangle \equiv |m_S = -1\rangle$ to describe the qubit basis states from here on-wards.

3.2 BACKGROUND

3.2.1 Standard measurement limited sensitivity

The standard model for phase measurements in quantum metrology is depicted in Figure 11. The equivalence of Mach-Zehnder interferometry (MZI) depicted in Figure 11a, the quantum network model (QNM) in Figure 11b[91], and Ramsey interferometry (RI) Figure 11c for phase estimation allows us to treat all three problems in a unified framework. Thus, it was pointed out by Yurke et al [92] that the states of photons injected into the MZI can be rewritten through application of Schwinger double-ladder operators to represent spin states. They showed that the number phase uncertainty relation for photons could be derived from the angular momentum commutation relations. Similarly, in the quantum network model [91], auxiliary qubits (or classical fields) are prepared in an eigenstate of the operator U such that $U|\phi\rangle = e^{-i\phi}|\phi\rangle$. The controlled-U operations on the system results in the following sequence of transformations on the qubits,

$$|+\rangle|\phi\rangle \xrightarrow{c-U} \frac{|0\rangle + e^{-i\phi}|1\rangle}{\sqrt{2}}|\phi\rangle \xrightarrow{H} \left(\cos(\frac{\phi}{2})|0\rangle + i\sin(\frac{\phi}{2})|1\rangle\right) e^{-i\phi/2}|\phi\rangle \tag{3.1}$$

where, H is the Hamiltonian governing the evolution. The state of the auxiliary register, being an eigenstate of U, is not altered along the network, but the eigenvalue $e^{-i\phi}$ is "kicked-out" in front of the $|1\rangle$ component of the control qubit. This model has allowed for application of ideas from quantum information to understand the limits of quantum sensing (see Refs.[93, 94, 95]).

Quantum metrology shows that the key resource for phase estimation is the number of interactions of n spins with the field prior to measurement (n measurement passes). Classical and quantum strategies differ in the preparation of uncorrelated or entangled initial states, respectively. Parallel and serial strategies differ in whether after the initial preparation, all spins are treated identically in terms of evolution and measurement. Thus, a serial strategy can trade-off running time with number of spins to achieve the same field uncertainty. In either case, the limiting resources can be expressed in one variable: the total interaction time $T = nt$. While quantum strategies can in principle achieve the Heisenberg phase uncertainty

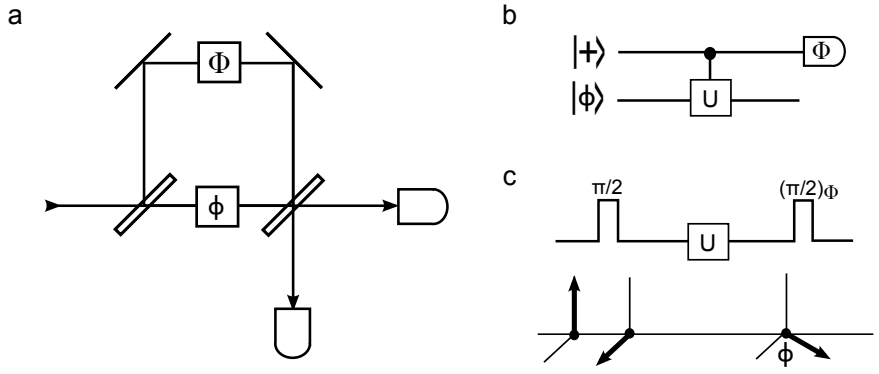

Figure 11: **Quantum metrology: a,** Mach-Zehnder interferometer senses the relative phase shift between two beams paths. **b,** Quantum circuit representation of the process and **c,** The analogous realization via Ramsey interferometry. The first $\pi/2$-pulse brings the spin vector from $|0\rangle$ to $(|0\rangle + |1\rangle)/\sqrt{2}$. The free precession interval introduces a phase ϕ on $|1\rangle$ relative to $|0\rangle$. Measurement after the second $\pi/2$-pulse senses this phase with respect to the control phase Φ.

$\langle(\Delta\phi)^2\rangle \propto 1/n^2 \propto 1/T^2$, classical strategies (whether parallel or serial), however, can at best scale with the phase uncertainty $\langle(\Delta\phi)^2\rangle \propto 1/n \propto 1/T$. This limit, known as the standard measurement sensitivity (SMS) arises from the combination of two causes: the probabilistic and discrete nature of quantum spin measurements, and the well-known central limit theorem for independent measurements[94, 95].

However, in obtaining the phase from the number of spins found to be pointing up or down after a measurement, there is an ambiguity. Because of the sinusoidal dependence of the phase accumulated, the above expression for the SMS assumes the phase has already been localized to an interval $(-\pi/2, \pi/2)$ around the true value. But for unknown fields, the entangled states typically accumulate phase $\sim n$ times faster than a similar un-entangled state. Thus, the working point must be known much more precisely for such strategies to be successful, which may defeat the original purpose of accurate field estimation. Thus, such quantum entangled strategies are better suited for situations where there are only likely to be small changes from a previously well-known field.

Consider the case of the classical strategy: we can write the interaction time $T = nT_2$, where T_2 is the decoherence time, and since $\delta\phi \sim 1/\sqrt{n}$ we obtain the field uncertainty $\delta B \sim$

$\frac{1}{\gamma_e\sqrt{T_2 T}}$. This also implies that the field must be known to lie in the range $|B| \leq B_{max} = \frac{\pi}{2\gamma_e T_2}$. Putting these together, we have that the dynamic range $DR = \frac{B_{max}}{\delta B} \sim \frac{\pi}{2}\sqrt{\frac{T}{T_2}}$. Thus the dynamic range will decrease as the coherence time increases.

The above expressions for the SMS do not take into account the effects of decoherence, measurement imperfections and other types of noise in experiments. We use the density matrix approach to describe the state of the quantum system and take into account these effects. Any unitary interaction on a single spin is essentially a rotation in the Bloch sphere. If we assume that the Rabi frequency $\Omega \gg \delta\nu$, we can assume that the rotations are instantaneous, and neglect the effect of the free evolution during the time of the pulses. In numerical simulations, we could also include the effect of finite Ω and $\delta\nu$ easily. For instance, a simple Ramsey experiment could be simulated as follows: an initial density matrix $\rho_0 = |0\rangle\langle 0|$ is first brought to $\rho_1 = R_y(\pi/2)\rho_0 R_y(\pi/2)^\dagger$, where $R_n(\theta) = \exp(-i(\vec{\sigma}.\vec{n})\theta/2)$ is the rotation operator along the $\hat{n}$ direction. This is equivalent to the action of a $(\pi/2)_y$ pulse in the experiment. Letting the system to evolve freely under the external magnetic field leads to the state: $\rho_t = U(t)\rho_1 U(t)^\dagger$, where $U(t) = \exp(-i\delta\nu\sigma_z t)$ is the time evolution operator. The application of the final $(\pi/2)_\Phi$ pulse is achieved using a z-rotation followed by $R_y(\pi/2)$:

$$\rho_f = R_y(\pi/2)R_z(\Phi)\rho_t R_z(\Phi)^\dagger R_y(\pi/2)^\dagger$$

The effect of decoherence is introduced by multiplying the off-diagonal elements with the decay factor $D(t, T_2^*) = \exp(-(t/T_2^*)^2)$, where T_2^* is the dephasing time set in our simulations. The probability for the measurement of the state in the Ramsey experiment is then given by,

$$P(u_m|\phi) = \frac{1 + (-1)^{u_m} D(t, T_2^*)\cos(\phi - \Phi)}{2} \tag{3.2}$$

where measurement bit $u_m = 1(0)$ is applied to to state $|0\rangle(|1\rangle)$. The bit u_m is determined by comparing the measured signal level with a pre-defined threshold value. Further, feedback rotations Φ are simply achieved by controlling the phase of the second $\pi/2$ microwave pulse. Repeating the experiment n times, we obtain the fraction of spins $n_0(n_1)$ that actually point up or down, thereby inferring the probability, e.g. $P(u_m = 1|\phi) = \frac{n_0}{n}$. The last step is to take the inverse of this equation and obtain ϕ. Unfortunately, as pointed out earlier, the inverse

cosine is multi-valued, and thus we have the quantum phase ambiguity which requires us to have prior knowledge about the phase and the working point for the Ramsey experiments.

The SMS limit can be calculated for our Ramsey experiments with NV centers, using the definition $(\delta\phi)^2 = \frac{\langle(\delta S)^2\rangle}{|dS/d\phi|^2}$ i.e., by assuming that signal to noise ratio $SNR = 1$. Because the phase error $\delta\phi = \gamma_e \delta B t$, we can also calculate the sensitivity $\eta = \delta B\sqrt{T}$. Here, $S = \langle Tr(M\rho)\rangle$ represents the signal from Ramsey experiments, and the variance of the signal, $\langle(\delta S)^2\rangle = Tr(M^2\rho) - (Tr(M\rho))^2$. The optical measurement operator $M = a|0\rangle\langle 0| + b|1\rangle\langle 1|$, where a, b are Poisson random variables with means $\kappa\alpha_0$ ($\kappa\alpha_1$) that represent our experimental counts when the qubit is in the $|0\rangle$ ($|1\rangle$) state respectively. Here, α_0 and α_1 represent the photon counts per optical measurement shot and κ is the number of times the measurement is repeated till the qubit state can be distinguished with sufficiently high fidelity, f_d. For instance, standard quantum discrimination protocols imply that $f_d > 0.66$ is sufficient to distinguish unknown pure states from a random guess[96]. The value of κ can be tuned in the simulations and experiments, but after fixing κ for a given experiment, N is then simply the statistical repetitions needed to find the system phase ϕ, thus the number of resources $n = N \cdot \kappa$. In the limit of single-shot readout $\kappa = 1$ on the electronic spin state, it is clear that quantum projection noise limits for n and N are equivalent, and otherwise they are proportional by a scale factor that depends on experimental efficiency.

We can explicitly calculate the sensitivity (with $SNR = 1$) for Ramsey measurements for general working points (see Appendix C). From definitions, it can be shown analytically that

$$\eta^2 = \frac{\kappa_{th}}{\gamma_e^2 t D(t, T_2^*)^2 \sin^2(\phi - \Phi)} \tag{3.3}$$

with,

$$\kappa_{th} = 1 + 2\frac{\alpha_0 + \alpha_1}{(\alpha_0 - \alpha_1)^2} + \frac{2D(t, T_2^*)\cos(\phi - \Phi)}{\alpha_0 - \alpha_1} - D(t, T_2^*)^2 \cos^2(\phi - \Phi) \tag{3.4}$$

Similar results have also been derived by Refs.[4, 97]. This expression reduces to the ideal SMS $\eta_{ideal}^{SMS} = \frac{e^{0.5}}{\gamma\sqrt{T_2^*}}$ in the limit of perfect experimental efficiency ($\kappa_{th} = 1$), and assuming that $\phi = 0, \Phi = \pi/2$. The importance of the working point can clearly be seen in this derivation since small changes in ϕ from the working point result in quadratic increase of η. The factor κ may be thought of as a loss mechanism, i.e. when we repeat the experiment N times, we only gain information from $1/\kappa$ of the runs during measurement and hence we

must repeat the experiment κ times to achieve the same sensitivity. For ideal (single-shot) measurements, which could potentially be realized through resonant excitation and increased collection efficiency[33], the SMS is given by taking $\alpha_1/\alpha_0 \to 0$ and $\alpha_0 \gg 1$, resulting in $\kappa = 1$.

3.2.2 Impact of dynamic range on magnetic imaging

In the standard approach of magnetic imaging, the contour height (Ramsey detuning $\delta\nu$) is set by estimating what the expected field would be at the NV spin, and calculating the corresponding detuning. The resonance condition will be met when the field from the target spins projected on the NV axis is within one linewidth $\delta B/\gamma_e$ of the Ramsey detuning, and the corresponding pixel in the image is shaded to represent a dip in the fluorescence level. Thus, only a single contour line of the magnetic field is revealed as a "resonance fringe" and a sensitivity limited by the intrinsic linewidth $1/T_2^*$ could be achieved. However, a quantitative map of the magnetic field is impossible in a single run due to the restriction of a single contour[98]. In order to further illustrate the importance of dynamic range, we show in Figure 12 the contours obtained for Ramsey imaging with a single NV center placed at a distance of 10 nm above different types of spins that are separated by 10 nm. The contours are calculated by using the expressions for magnetic fields from point dipoles with magnetic dipole moments for the corresponding nuclear spin species. Our simulations do not take into account any measurement imperfections such as fringe visibility, and assume that the decoherence time of the NV spin can be made sufficiently long enough to detect the various species of spins, e.g. $T_2 = 100$ ms. From the figures, it is clear that when spin species of different types are present in the sample, the contours get greatly distorted and makes it difficult to reconstruct the position of the spin.

Using the same procedures, we find that an error in the NV spin position inside the diamond lattice will significantly affect both resolution and image reconstruction. First, the resolution of the image is set by the gradient of the field from the target spin ∇B and the line width δB, giving rise to a resolution $\Delta x_{res} = \delta B/\nabla B$. Here $\nabla B = \frac{3\mu_0 m}{4\pi r^4}$, where m is the magnetic dipole moment of target spin, μ_0 is the permeability in vacuum. From the prior

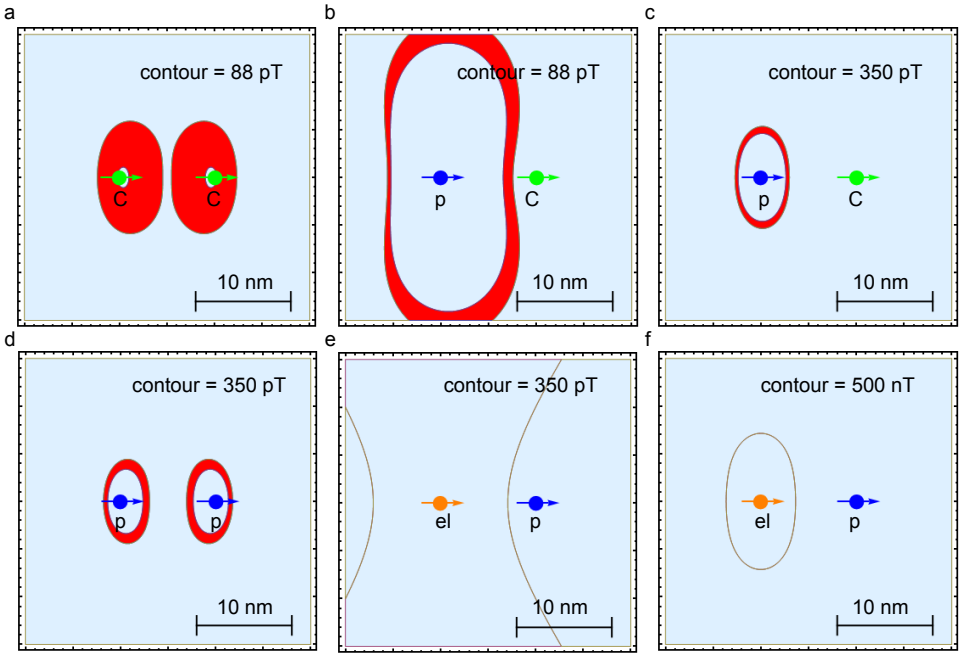

Figure 12: **Ramsey imaging: a-f,** Calculated resonant imaging contours by fixing the detuning of the Ramsey sequence at a value expected from the field of a single electron (el), proton (p) or carbon-13 (C) spin. The line width of the sensor is set to be 30 pT which could be achieved with coherence time $T_2 = 100$ ms and averaging time $T = 14$ s. The sample-probe height is 10 nm. The contour images do not sufficiently reveal the existence of different spins. For instance, existence of carbon-13 is not revealed in **b** and **c** whereas the existence of proton is not revealed in **f**.

expression for the line width, this becomes $\Delta x_{res} \sim \frac{\kappa}{\gamma_e \nabla B \sqrt{T_2 T}}$. For a line width $\delta B \approx 30$ pT and a target proton spin, we get $\Delta x_{res} \sim 0.75$ nm, which agrees well with the contour plots in Figure 12. Secondly, if the NV position has an error of δr, the working point will shift by $\nabla B\, \delta r$. When the shift is comparable to the field sensing limit of Ramsey measurements B_{max} defined earlier, $\frac{\pi}{2\gamma_e T_2}$, we will lose the sensitivity needed to reconstruct the position. Putting in the numbers used for our simulations, we obtain that position reconstruction will not be possible if $\delta r \sim \frac{2\pi^2 r^4}{3\gamma_e \mu_0 m T_2} \approx 3.7$ nm. In practice the error in working point should be a fraction e.g. 30 – 50% of the dynamic range B_{max} since the linewidth will be broadened otherwise. Under normal growth or implantation conditions for near-surface NV centers, the typical uncertainty in NV position is $\sim 1 - 10$ nm[40, 41, 26]. By increasing the dynamic range of the imaging technique, we can relax the requirement for knowing the NV position

more accurately.

3.2.3 Phase estimation methods

The quantum network model for quantum metrology allows us to apply ideas from quantum information to resolve the problem of dynamic range. To see how this works, let us consider the quantum phase estimation algorithm (QPEA) that utilizes the inverse quantum Fourier transform of Shor's algorithm. The QPEA (Figure 10a) requires K number of unitaries $(U^p, p = 2^0, 2^1, ..., 2^{K-1})$ to be applied in order to obtain an estimation

$$\phi_{est} = 2\pi(\frac{u_1}{2^0} + \frac{u_2}{2^1} \ldots + \frac{u_K}{2^{K-1}}) \equiv 2\pi(0.u_1u_2 \ldots u_K)_2$$

for the classical phase parameter ϕ , with K bits of precision. When the phase is expressible exactly in binary notation (i.e. a fraction of a power of two), the QPEA gives an exact result for the phase estimator ϕ_{est}[85, 86].

Each application of U is controlled by a different qubit which is initially prepared in the state of $|+\rangle = (|0\rangle + |1\rangle)/\sqrt{2}$. The control introduces a phase shift $e^{ip\phi}$ on the $|1\rangle$ component. Measurement takes place in the σ_x basis (X) and the results control the additional phase shifts (control phases Φ) on subsequent qubits. This basically enables performing the inverse quantum Fourier transforms without using two-bit or entangled gates [85, 86, 87].

As shown by Ref.[99], the QPEA does not achieve the SMS that we derived earlier for the Ramsey experiments. However, it solves the problem of needing prior information about the working point. The reason the QPEA does not reach the best sensitivity is due to the fact that for arbitrary phases, we can view the QPEA estimator $\phi_{est} = 2\pi(0.u_1u_2...u_K)_2$ as a truncation of an infinite bit string representing the true phase. However, in the QPEA, every control rotation Φ_k depends on the measurement results of all the bits to the right of the u_k bit. Thus, even if all measurements are perfect, the probabilistic nature of quantum measurements implies that there will be a finite probability to make an error especially for the most significant bits. Although the probability of error is low, the corresponding error is large, and therefore the overall phase variance is increased above the quantum limit. It was noted by Ref.[99] that by weighting (error-checking) the QPEA for the most significant bits

and using fewer measurements on the least significant bits, this problem could be reduced but not completely overcome.

A modified version of the QPEA was introduced by Berry and Wiseman in Ref.[100] which would work for all phases, not just those that were expressible as fractions of powers of two. This model required adaptive control of the phase similar to the QPEA depending on all previous measurements, but also increased the complexity of the calculations. Surprisingly, a simpler version of the Berry and Wiseman algorithm, referred to in Refs.[89, 88] as non-adaptive phase estimation algorithm (NAPEA) (Figure 10b) was also found to give nearly as good results, especially at lower measurement fidelities. In the NAPEA, the number of measurements vary as a function of k: $M(K,k) = M_K + F(K-k)$ and the control phase simply cycles through a fixed set of values typically $\Phi = \{\Phi_1, \Phi_2, \ldots \Phi_{M(K,k)}\}$ after each measurement.

Exactly as for the Ramsey measurements, the conditional probability of the u_m measurement is given by:

$$P(u_m|\phi,k) = \frac{1 + (-1)^{u_m} D(t, T_2^*)\cos(\phi_k - \Phi)}{2} \tag{3.5}$$

Now, with the assumption of a uniform *a priori* probability distribution for the actual phase ϕ, Bayes' rule can be used to find the conditional probability for the phase given the next measurement result:

$$P(\phi|\vec{u}_{m+1}) \propto P(u_{m+1}|\phi)P(\phi|\vec{u}_m) \tag{3.6}$$

where $P(\phi|\vec{u}_m) \equiv P_m(\phi)$ is the likelihood function after $u_1, u_2, \ldots u_m$ bit measurements, and gets updated after each measurement. In Refs.[89, 88], the best estimator is again obtained through an integral over this distribution. However, in our work, we simply use the the maximum likelihood estimator (ϕ_{MLE}) of the likelihood function[88, 89, 90].

In our work, we have chosen to compare the NAPEA with the standard QPEA for several reasons. Firstly, the adaptive algorithm of Refs.[88, 89, 90] is more difficult to implement experimentally, and in practice seems to offer only slight improvements over the NAPEA. Secondly, the QPEA is a standard PEA which has a simple feed-forward scheme based purely on the bit results. Unless otherwise stated, we set $t_{min} = 20$ ns and $T_2^* = 1200$ ns in our simulations. The necessary steps involved in the simulation of the both types of PEA are enumerated below.

3.2.4 Simulation of PEAs:

For both QPEA and NAPEA, the following steps are common:

1. Parameter initialization: $t_{min}, K, M_K, F, k = K, \Phi = 0$
2. Preparation of the initial superposition state: $\rho_0 = |+\rangle\langle+|$ where $|+\rangle = (|0\rangle + |1\rangle)/\sqrt{2}$.
3. The unitary phase operation $U^{2^{k-1}}$ on ρ_0: $\rho_k = U^{2^{k-1}}\rho_0(U^\dagger)^{2^{k-1}}$
   where $U = |0\rangle\langle 0| + e^{-i\phi}|1\rangle\langle 1|$ and $\phi = \gamma_e B_{ext} t_{min}$.
4. The feedback rotations Φ on ρ_k: $\rho_f = R\rho_k R^\dagger$, where $R = |0\rangle\langle 0| + e^{i\Phi}|1\rangle\langle 1|$.
5. POVM measurement to obtain the signal $S = Tr[M.\rho_f]$ where M is the imperfect measurement operator as described in the text: $M = a|0\rangle\langle 0| + b|1\rangle\langle 1|$.
6. Assignment of the bit u_m (0 or 1) by comparison of S with the threshold signal.

QPEA:

7. Repeat steps 2-6 $M(K,k)$ number of times.
8. Update the controls:
$$\Phi = \sum_{j>k} \frac{u_k}{2^{j-k}}\pi \ , \quad k = k-1$$
   where u_k is chosen by majority vote among $\{u_m\}$ for a given k.
9. Repeat steps 2-8 until $k = 1$.

NAPEA:

7. Update the control phase Φ from the list $\{\Phi_1, \Phi_2, \ldots \Phi_{M(K,k)}\}$
8. Repeat steps 2-7 $M(K,k)$ number of times.
9. Update $k = k-1$.
10. Repeat steps 2-9 until $k = 1$.

3.3 VERIFICATION OF THE SIMULATION METHOD

To verify our simulation method needed for the phase estimation algorithms, we first carried out Monte-Carlo simulation procedure for Ramsey fringes where we have the analytical results derived above for comparison. Figure 13 demonstrates first the measurement fidelity

for distinguishing $|0\rangle$ and $|-1\rangle$ states for two different sample sizes. The measurement fidelity is defined as

$$fd = \frac{\langle 0|\rho^0|0\rangle + \langle 1|\rho^1|1\rangle}{2}$$

where $\rho^{0(1)}$ corresponds to the state initially prepared in $|0\rangle(|1\rangle)$. The average photon counts per optical measurement for the state $|0\rangle$ ($|1\rangle$) $\alpha_0 = 0.010$ ($\alpha_1 = 0.007$) are set throughout our simulations to correspond with the experiments of Ref.[16]. The experimental sequence was run with initialization of the spin into the $|0\rangle$ state, followed either immediately by fluorescence measurement or by a π pulse and then measurement. The experimental threshold for the bit measurement u_m is usually chosen as the average of the means of the two histograms. Our results, shown in Figure 13a, show that by tuning the number of samples κ, we can achieve very high measurement fidelity.

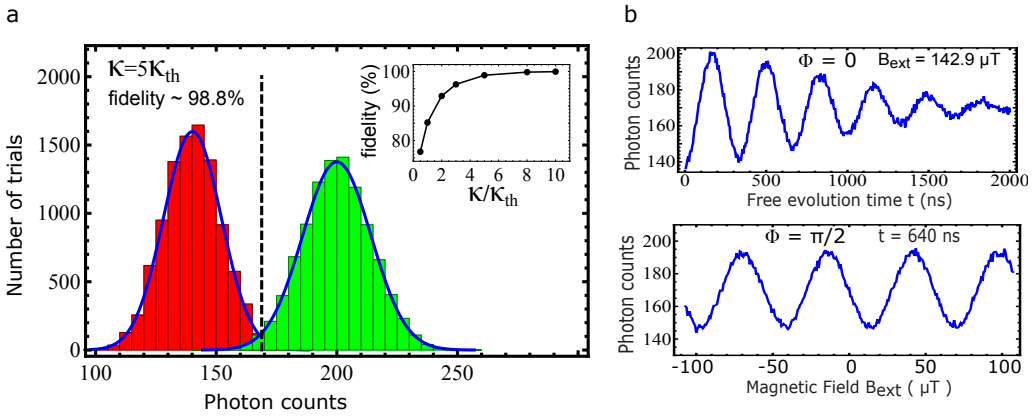

Figure 13: **Ramsey Simulations: a,** Measurement fidelity: The histogram obtained with $N = 10000$ measurement for both $|0\rangle$ and $|1\rangle$ states are shown. Lesser the overlap higher the fidelity in distinguishing the states. A sample number $\kappa = 5\kappa_{th}$ leads to a fidelity $\approx 98.8\%$. (inset) Fidelity improves with κ. **b,** Simulation of Ramsey Experiment: Ramsey signal after 50 averages when free time t is varied while $B_{ext} = 142.9\,\mu$T is fixed (top) and as B_{ext} varied while $t = 640$ ns is fixed (bottom). Here, $\kappa = 5\kappa_{th}$ was used.

3.4 SIMULATION RESULTS

Figure 14a shows the final phase likelihood distribution as parameter K is varied. The secondary peaks in the final likelihood distribution occurs due to the phase ambiguity of individual measurements. As more measurements are performed, these secondary peaks becomes further suppressed. Note that the figure is given in log scale in order to make the secondary peaks more visible. Recall in QPEA, the bit string itself represents a binary estimate for the unknown phase. However, in order to make a fair comparison between the QPEA and NAPEA, we use the Bayesian approach to analyze the QPEA results as well. The digitization in the phase estimate in QPEA is clearly observed in its phase likelihood distribution. A phase that is perfectly represented by the bit string can lead to a perfect estimate, provided sufficient measurement fidelity is available.

Figure 14b shows the histogram of ϕ_{MLE} when each PEA is performed 100 times. While QPEA shows only two possible outcomes for ϕ_{MLE}, the histogram of ϕ_{MLE} for NAPEA is approximately Gaussian around the system phase (blue line). Interestingly, the difference of the two ϕ_{MLE} outcomes in QPEA is equal to $2\pi/2^K$ where $K = 6$ in this simulation.

The phase readout ϕ_{MLE} is converted to a field readout by the linear relationship: $B_{MLE} = \phi_{MLE}/\gamma_e t_{min}$ in Figure 14c and agrees well with the external magnetic field B_{ext}. Hence PEA can be useful for sensing unknown magnetic fields in contrast to the standard Ramsey approach in which the readout is sinusoidally dependent on the external field.

3.4.1 Multiple control phases in NAPEA

To understand the choice of control phases in the NAPEA, one could imagine a simple version of NAPEA without multiple control phases, i.e., $\Phi = \{0\}$. The final phase likelihood distribution in this case will be symmetric about the origin $\phi = 0$ (see Figure 15a inset), because the likelihood distribution is a product of many even cosine functions. Introducing a second control phase i.e., $\Phi = \{0, \pi/2\}$ breaks this symmetry and result in a unique answer for ϕ_{MLE}(Figure 15b). However, introducing even more control phases can be useful for obtaining a consistent sensitivity throughout the full field range. Table 1 summarizes the

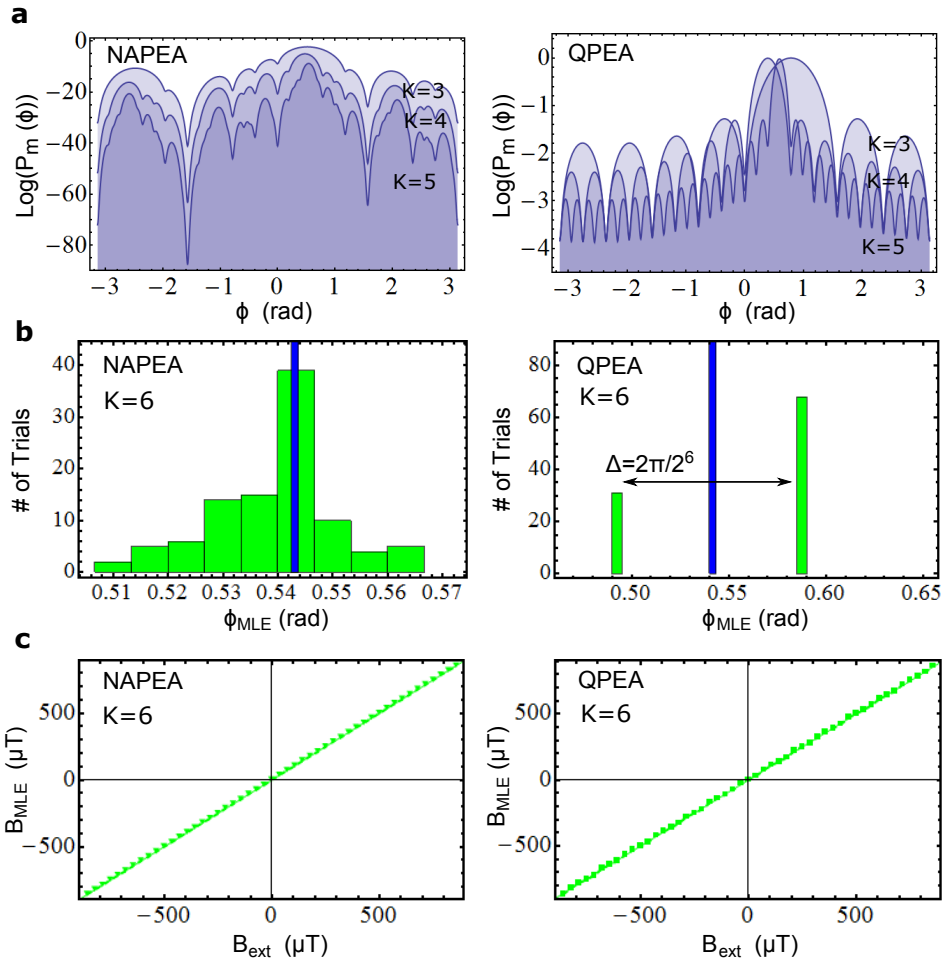

Figure 14: **Phase Likelihood distribution: a,** Phase likelihood distribution **b,** Distribution of MLE's **c,** Magnetic field readout of QPEA (right) with $\kappa = 10\kappa_{th}$, $M_K = 1$, $F = 0$, $K = 6$ and NAPEA (left) $\kappa = 5\kappa_{th}$, $M_K = F = 4$, $K = 6$.

terms that will be used in this thesis, in describing the different sets of control phases.

The variance of the phase readout $(\delta\phi_{MLE})^2$ with respect to the given quantum phase is plotted in Figure 15c. It is noteworthy that a QUAD set of control phases is no better than the DUAL set. While former case leads to X and Y basis measurements, latter case corresponds to X, Y, -X and -Y basis measurements. Therefore similarity in results of DUAL and QUAD sets could be explained as follows. Imagine a condition that resulted in a bit measurement u_m in the X(Y) basis. The same condition would have resulted a bit

Control phases $\{\Phi\}$	Term
$\{0, \frac{\pi}{2}\}$	DUAL
$\{0, \frac{\pi}{2}, \pi, \frac{3\pi}{2}\}$	QUAD
$\{0, \frac{\pi}{4}, \frac{\pi}{2}, \frac{3\pi}{4}, \pi, \frac{5\pi}{4}, \frac{3\pi}{2}, \frac{7\pi}{4}\}$	OCT
$\{0, \frac{\pi}{M(K,k)}, \frac{2\pi}{M(K,k)}, \ldots \frac{[M(K,k)-1]\pi}{M(K,k)}\}$	VAR

Table 1: List of control phases used in NAPEA and corresponding terms used in this thesis.

measurement $1 - u_m$ in the -X(-Y) basis which will eventually result in the same probability distributions. Because the DUAL and the QUAD sets implies measurement in $\{X, Y\}$ and $\{X, Y, -X, -Y\}$ basis respectively, they tend to the same final results, and are technically equivalent. As seen in Figure 15c, the DUAL and the QUAD cases have relatively worse phase variance at working points corresponding to $\phi \sim 0$ or $\pm\pi/2$. This effect is significantly suppressed in the case of eight control phases, the OCT set. Using the variable set of control phases (VAR) leads to further improvement in consistency because of the rapid increment in the number of control phases according to the weighting scheme. However, the VAR set can be comparatively difficult to implement in practice. The consistency of the various sets of control phases are summarized by calculating the standard deviation of the variance over the entire interval $(-\pi, \pi)$. Our calculation summarizes the trends described above by giving these numbers in ascending order: VAR(0.71), OCT(1.80), DUAL(4.13), QUAD(4.28) in units of $10^{-3}\,\mathrm{rad}^2$.

3.4.2 Weighting scheme and the measurement fidelity

In this section, we explore the effect of weighting scheme and the measurement fidelity on the NAPEA and QPEA.Figure 16 gives phase sensitivity scaling $(\delta\phi_{MLE})^2 N$ when K is increased from 1 to 9. Here N is equivalent to the number of unitary operations in [89, 88]

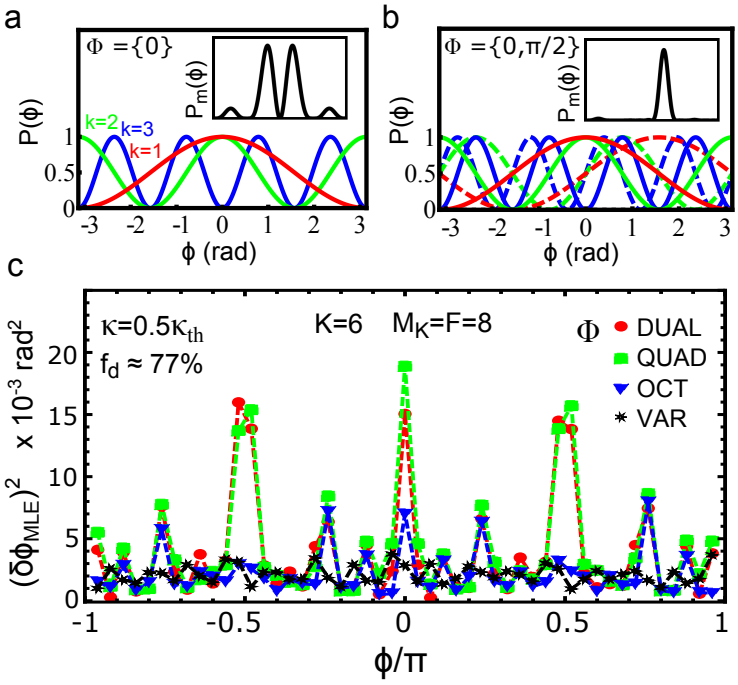

Figure 15: **Control phases in NAPEA: a,** A simplified form of PEA with a single control phase $\Phi = \{0\}$ leads to a final phase likelihood distribution which symmetric around "0" and consequently gives two possible MLE's. **b,** An additional control phase can solve this problem by suppressing the wrong MLE. Red, green and blue lines give the corresponding individual probability distributions for k=1, k=2 and k=3 measurement outcomes respectively. Dashed lines correspond to the case of $\Phi = 90^0$ **c** The red-circle, green-square, blue-triangle, and black-star represent the DUAL, QUAD, OCT, and VAR set of control phases respectively. DUAL and QUAD lead to similar result, and have large variance of the phase readout $(\delta\phi_{MLE})^2$ at points corresponding to $\phi \sim 0$ or $\pm\pi/2$. The OCT suppresses this effect and thus will maintain almost a constant sensitivity over the full field range. The VAR leads to further improvement in consistency because of the rapid increment in the number of control phases according to the weighting scheme. The standard deviation of the phase readout variances at all points $\sigma_{(\delta\phi_{MLE})^2}$, corresponding to DUAL, QUAD, OCT and VAR sets are 4.13, 4.28, 1.80 and 0.71, 10^{-3}rad^2 respectively.

and can be calculated as below.

$$N = \sum_{k=1}^{K} M(K,k)\, 2^{(k-1)} = [M_K(2^K - 1) + F(2^K - K - 1)] \tag{3.7}$$

Figure 16(a) shows the scaling of sensitivity with N for five different choices of quantum phases $\phi = (\pi/9.789, \pi/7.789, \pi/5.789, \pi/3.789, \pi/1.789)$, while the inset figure gives the average behavior. Here onward, we present only the average result in the scaling plots

for clarity. It is important to present the average behavior rather than the behavior for a particular quantum phase, because the sensitivity is not necessarily the same for all phases as shown in the previous section. From Figure 16(b) and (c), it is clear that although weighting can play a role in NAPEA, there also exist non-weighted choice of optimal results. However, the optimal non-weighted parameters are highly dependent on f_d. For instance, with $f_d =$ 98.8%, the optimum non-weighted parameters were found to be $\{K, M_K, F\}$={7,8,0} while the same parameters led to $\sim 10^3$ worse sensitivity when $f_d = 92.9\%$. On the other hand the weighted parameters {7,8,8} resulted in nearly same sensitivities in either case.

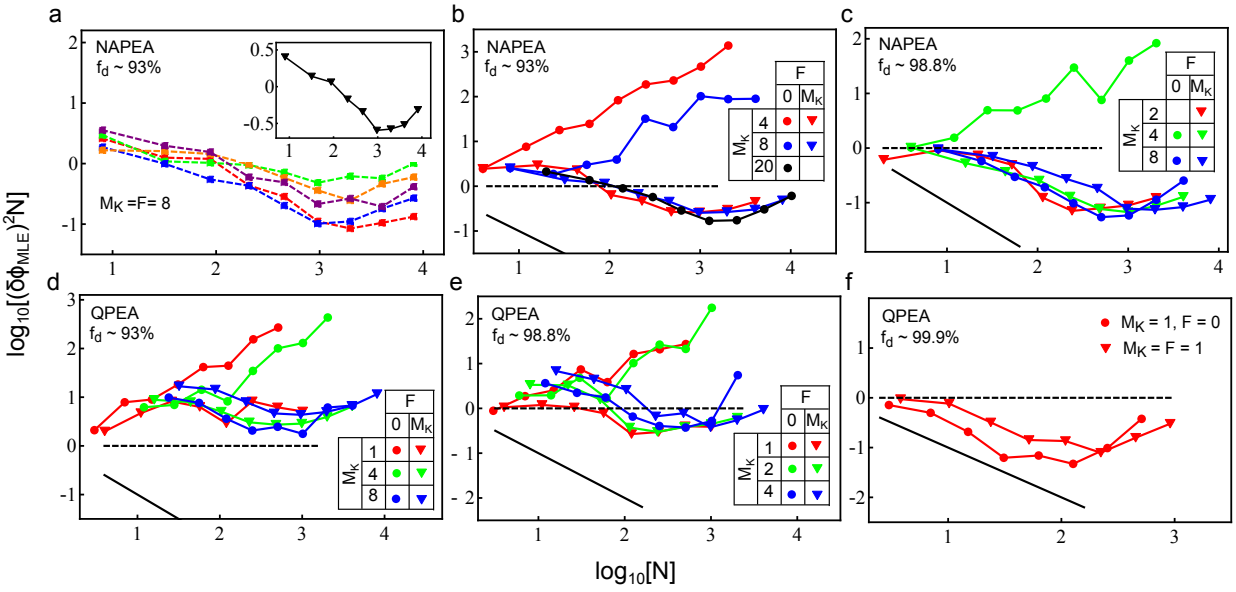

Figure 16: **Precision scaling of the phase measurement a,** The NAPEA sensitivity $(\delta\phi_{MLE})^2 N$ obtained as resource is increased by increment of K for different system phases. (inset) The average obtained for above system phases is shown. **b-f,** The precision scaling of average NAPEA (QPEA) phase sensitivity under different conditions of fidelity and PEA parameters are shown in **b-c,** (**d-f**). $F = 0$ implies no weighting. The best results in QPEA requires extremely high fidelity $> 99\%$ whereas for NAPEA a fidelity $\approx 90\%$ is sufficient. The black dashed (solid) line shows standard-quantum (Heisenberg) limit for phase measurement.

In QPEA, the change in control phase Φ occurs with the change in k. Moreover, only a single bit measurement result u_k is available for each k, unlike in the case of NAPEA where there exist $M(k, K)$ bit measurements. However, in order to make a fair comparison, we still perform the weighting scheme on QPEA as described in section 3.2.3 to obtain $M(k, K)$ bit measurements. We use majority voting of bit measurements for determination of the

PEA	Fidelity	$\{M_K, F, K\}$	$\sigma_{(\delta\phi_{MLE})^2}$ (rad^2)	η^2_{avg} ($\mu T^2/Hz$)	T (s)
NAPEA(OCT)	92.9% ($\kappa = 2\kappa_{th}$)	$\{20, 0, 6\}$	0.022×10^{-3}	1.58 ± 0.35	0.202
QPEA	99.9%($\kappa = 10\kappa_{th}$)	$\{1, 0, 7\}$	0.197×10^{-3}	3.67 ± 1.62	0.102

Table 2: Summery of best results from QPEA and NAPEA

control phases. It turns out that the best results in QPEA are obtained only with extremely high measurement fidelity ($f_d > 99\%$) and requires no weighting ($M_K = 1, F = 0$). Further, even after using Bayesian estimation, the sensitivity in QPEA is ultimately limited by the minimum bit error of the phase readout given by $\delta\phi_{est} = \pi/2^K$.

3.4.3 Field sensitivity and PEA performance

The corresponding scaling of field sensitivity $\eta^2 = (\delta B)^2 T$ for some of the data in Figure 16 is shown in Figure 17a. Here, $(\delta B)^2 = \langle (B_{MLE} - B_{ext})^2 \rangle$ is the variance of field with respect to the external magnetic field and $T = N t_{min} \kappa$ is the total evolution time of the PEA. The best sensitivity results from NAPEA was obtained with a fidelity 92.9% and an OCT set of control phases. QPEA's best results requires extremely high fidelity 99.9%, and furthermore show a significant fluctuation in the sensitivity over the full field range. The statistics obtained here along with PEA parameters used are summarized in the Table 2.

While NAPEA demands relatively lesser measurement fidelity than in QPEA, the total estimation time is larger. However, as shown in above table and Figure 17c, the sensitivity obtained from NAPEA is better and more consistent compared to QPEA. Although it is possible to enhance the dynamic range of PEA by reducing t_{min} and thereby achieving higher K, no significant improvement in sensitivity was observed because it is ultimately limited by the SMS at the longest evolution time. On the other hand reaching the best SMS in Ramsey limits the dynamic range.

Figure 18b show the total time and the dynamic range $DR = B_{max}/\delta B$ as a function of t_{min} for different choices of NAPEA parameters: M_K and F. The parameter K is chosen such that the longest evolution time interval is always the same i.e., $2^{K-1} t_{min} \approx T_2^*$. Here,

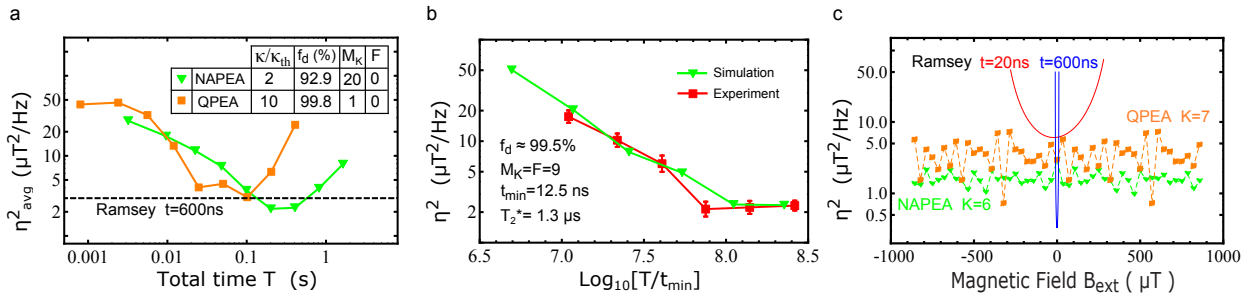

Figure 17: **Magnetic field sensitivity a,** Field sensitivity $\eta^2 = (\delta B)^2 T$ averaged over many different field with the number of resources. The resources is increased by the increment of K and given in units of time. The best cases obtained from QPEA and NAPEA is compared with the optimum Ramsey sensitivity averaged over its full field range. **b,** Field sensitivity with unitless number of resources $N = T/t_{min}$. The simulation here was performed with the exact experimental conditions and is in well agreement with experimental results. **c,** The NAPEA sensitivity is roughly constant throughout the full field range whereas QPEA sensitivity is not. The red (blue) curves show theoretical limits of Ramsey sensitivity for t=20 ns (t=600 ns).

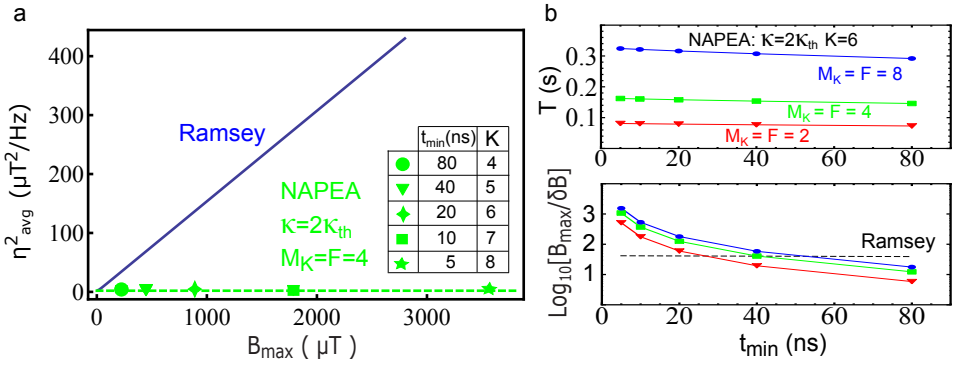

Figure 18: **Dynamic range and Time Constants a,** The standard Ramsey approach show a trade-off between the sensitivity and B_{max} whereas PEA can maintain the same sensitivity upto a wide field range. **b,** (top) The total time for the NAPEA as a function of minimum evolution time interval t_{min}. The parameter K is chosen such that the longest evolution time interval is always the same, 1280 ns. (bottom) The corresponding dynamic range $DR = B_{max}/\delta B$ is shown, where δB is the minimum detectable field change. The black dashed line is obtained from the Ramsey theoretical limit $\eta_{th}/\sqrt{T}$ for the same experimental conditions. Here, the total time for PEA with $M_K = F = 8$ is used for T.

δB is the minimum detectable field amplitude. The corresponding Ramsey DR obtained for an averaging time equal to that of NAPEA with $M_K = F = 8$ is also shown. Clearly, NAPEA gives better DR for smaller t_{min}. By a suitable choice of NAPEA parameters we can reduce the time constant without significant compromise between the sensitivity and DR. For instance, when t_{min}=10 ns, a change in the NAPEA parameters from $M_K = F = 8$ to $M_K = F = 4$ will reduce the time constant by 50% though the reduction in sensitivity and DR is only $\sim 28\%$.

In principle, t_{min} could be lowered to any value in order to achieve a desired dynamic range. However in practice, this is limited by the finite pulse length and gives a lower-bound; $t_{min} > t_\pi$. On the other hand, strong qubit driving can invalidate the RWA due to the effect known as the Bloch-Siegert shift[101, 102]. Here, the qubit resonance is shifted by a factor of $(1+\Omega^2/4\omega_0^2)$ in the rotating frame of the driving field where Ω is the Rabi frequency and ω_0 is the qubit resonance frequency in the Lab frame. However, the RWA can still be reasonably applicable upto a $\sim 1\%$ of a Bloch-Siegert shift[102] corresponding to $\Omega/\omega_0 \sim 1/5$. This suggests that, in our application where a background magnetic field of ~ 500 G leads to a qubit frequency $\omega_0 \approx 1.4$ GHz associated with $m_s = 0 \leftrightarrow m_s = -1$ transition, the Rabi driving could be made as strong as $\Omega \sim 300$ MHz resulting to lower bound of $t_{min} \sim 3.4$ ns. In case of driving the $m_s = 0 \leftrightarrow m_s = +1$ transition under the same conditions, qubit frequency is $\omega_0 \approx 4.3$ GHz and corresponds to a lower bound of $t_{min} \sim 1.2$ ns. Extrapolation from Figure 18b data gives the upper bound for the dynamic range in this case, $DR \sim 10^5$, which should be sufficient to simultaneously detect the fields from both electron and nuclear spins in a single magnetic field image.

3.4.4 PEA for AC Magnetometry

The best sensitivity in DC magnetometry is limited by the dephasing time T_2^* which is usually much less than the decoherence time T_2. Therefore, one could be interested in implementing the PEA for AC magnetometry in order to achieve improvement in the sensitivity: $\eta_{AC} \approx \eta_{DC}\sqrt{\frac{T_2^*}{T_2}}$. Here we show by simulations, how PEA could be applied for sensing AC magnetic fields, $b(t) = b_{ac}\cos(\omega t + \theta)$. Our approach can be used to sense an unknown field amplitude

b_{ac} as well as the phase θ of the field. Because our focus is only to describe the method of implementation, we consider the ideal scenario of 100% photon efficiency and neglect the effect of decoherence for simplicity.

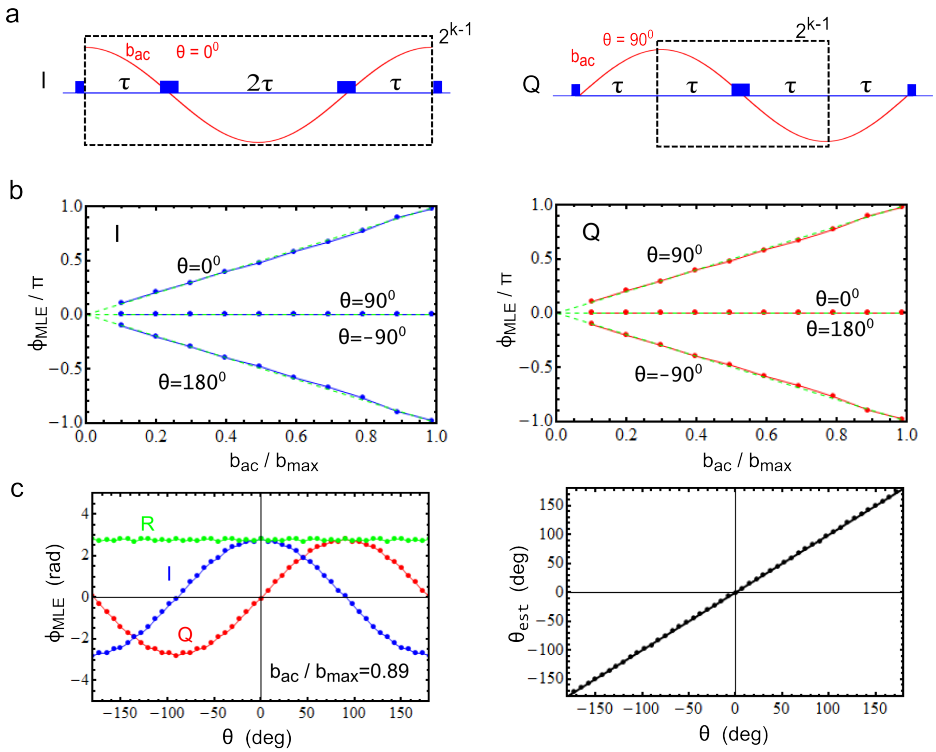

Figure 19: **AC magnetometry with PEA a,** type-I (left) and type-Q (right) MW pulse sequence used for necessary phase accumulations from the AC magnetic field. **b,** PEA readout with type-I (left) and type-Q (right) sequences. **c,** detection of the AC magnetic field phase.

Performing PEA requires the ability to accumulate several phases: $\phi, 2\phi, 4\phi$ etc, where ϕ is the unknown quantum phase to be measured. In DC magnetometry, these phase accumulations are achieved by varying the free evolution time in Ramsey sequence. In order to achieve the required phase accumulations from an AC-field, we can have two types of echo-based pulse sequences referred to as type-I and type-Q (Figure 19a) in this thesis. Type-I sequence is maximally sensitive to magnetic fields with $\theta = 0^0$ or $\theta = 180^0$ whereas completely insensitive (i.e., gives zero phase accumulation) to $\theta = \pm 90^0$. Type-Q sequence on the other hand, is maximally sensitive to magnetic fields with $\theta = \pm 90^0$ and completely insensitive to $\theta = 0^0$ or $\theta = 180^0$ (Figure 19b). Further, a magnetic field with an arbitrary

phase θ could be expanded as:

$$b(t) = b_{ac}\cos(\omega t + \theta) = b_{ac}\cos(\theta)\cos(\omega t) - b_{ac}\sin(\theta)\sin(\omega t)$$

Therefore PEA with type-I and type-Q sequences lead to readout $\phi_I \propto b_{ac}\cos(\theta)$ and $\phi_Q \propto b_{ac}\sin(\theta)$ respectively. Hence, the phase information of the unknown field could be extracted: $\theta_{est} = \tan^{-1}[\phi_Q/\phi_I]$ (Figure 19c). Application of PEA for AC magnetometry is demonstrated in Chapter 5 and these results were recently published in Ref.[47].

3.5 CONCLUSION

In conclusion we have made a detailed investigation of PEA approach for magnetic field sensing via Monte-Carlo simulations and compared with Ramsey magnetometry. The importance of dynamic range for magnetic imaging of unknown samples was also emphasized. The high dynamic range and the linear response to the field amplitude makes PEA useful for many practical applications. When it comes to NAPEA, DUAL and QUAD set of control phases give similar results and have relatively worse sensitivities at working points corresponding to $\phi \sim 0$ or $\pm\pi/2$. This effect can be suppressed by introducing more control phases. In particular, the use of OCT case set of control phase lead to a significant improvement in uniformity of the sensitivity over the full field range. The weighting scheme can play a role in NAPEA but not in QPEA. Even for NAPEA, there is always a choice of non-weighted PEA parameters that can lead to optimum results, but the optimum parameters in general depend on the measurement fidelity. The best results in NAPEA are however guaranteed for measurement fidelity above $\sim 90\%$. QPEA shows a significant variation in the sensitivity across the full field range as a consequence of the binary error in the readout. Further, the best results in QPEA demands extremely high fidelity $\sim 99\%$. Because multiple measurements are not required, the total estimation time for QPEA is much less than in NAPEA. In any case, NAPEA seems to be superior to QPEA due to (a) better sensitivity, (b) consistency in sensitivity throughout the full field range, (c) comparatively less demanding measurement fidelity and (d) for its simplicity in experimental realization. Finally, we have shown that

PEA can also be implemented for detection of unknown AC magnetic fields. Our method allows for the detection of both field amplitudes, and the phase of the field.

4.0 HIGH DYNAMIC RANGE DC MAGNETOMETRY

4.1 INTRODUCTION

The standard measurement technique for magnetic sensing is based on the well-known method of Ramsey interferometry[103, 104, 94] for detecting changes in the frequency of an atomic transition. An external magnetic field B_{ext} shifts the transition frequency by $\delta\nu = \gamma_e B_{ext}$, where $\gamma_e \approx 28$ GHz/T is the NV gyromagnetic ratio. Microwave (MW) pulses prepare a spin superposition state that accumulates a phase $\phi = \delta\nu \times t$ during an interaction time t. This phase determines the probability distribution for subsequent measurement outcomes of the spin state along some axis Φ (see Figure 21b). The goal is then to obtain a phase estimator with the highest precision (smallest phase variance) over as large a dynamic range as possible. Here, 'dynamic range' refers to the maximum field value (B_{max}) that can be accurately detected with high precision; that is, no prior information about the field is known except that it is within this range. This would be a typical situation in most applications of nanoscale magnetometry and imaging, where unknown samples are being probed. In this work, we implement NAPEA with single spins in diamond that simultaneously realize both accurate field sensing and decoherence-limited field precision.

4.2 THE EXPERIMENTAL SETUP

NV centers are identified and imaged using our home-built confocal microscopy system. A high- NA dry microscope objective (Olympus 0.95 NA) is used in this confocal setup for NV excitation and collection of fluorescence emission. Type IIa single crystal diamond

sample (sumitomo with [1 1 1] orientation) is used in these experiments. Phonon-mediated fluorescent emission (630-750 nm) for the single NV center is detected under coherent optical excitation (COHERENT COMPASS 315M 532 nm LASER) using a single photon counting module (PerkinElmer SPCM-AQR-14-FC). Green excitation of the NV center polarizes the electron spin into $|m_S = 0\rangle$ sublevel of the $^3A_2$ ground state due to optical pumping. The rate of fluorescence signal counts varies for the $|m_S = 0\rangle$ and $|m_S = \pm 1\rangle$ states, which enables the optical detection of the electron spin. The photon counting takes place at the both ends of the optical excitation pulse. The counts at the beginning known as "signal"(S_i) is highly dependent on the NV state while the counts at the end of optical excitation known as "reference" (R_i) is not. By taking the percentage change of S_i with respect to R_i, we minimize the effect of laser fluctuations on our experiments.

A static magnetic field of 40 mT is applied along the NV axis by a permanent magnet. Level anti-crossing (LAC) occurs between the $|m_S = -1\rangle$ and $|m_S = 0\rangle$ sublevels in the excited state, which results in dynamic nuclear-spin polarization (DNP) of ^{14}N nuclear spin (I=1) associated with most NV experiments (see Section 2.3.1). MW (Rohde&Schwarz SMIQ03B synchronized to SRS FS725) is delivered via a 20 μm diameter copper wire placed on the diamond sample, which is soldered into a strip-line (50 ohms impedance matched). The resonant MW radiation for the $|m_S = 0\rangle \leftrightarrow |m_S = -1\rangle$ transition leads to coherent manipulation of the spin. A detailed list of components/instruments used in the overall experimental apparatus can be found in Appendix F.

Recall in the Ramsey experiment, the first optical pulse prepares the NV spin in the $|m_s = 0\rangle$ state, and the first $(\pi/2)_y$ pulse creates a superposition state $(|0\rangle + |-1\rangle)/\sqrt{2}$. The state evolves for a time t, creating the state $(|0\rangle + e^{i\phi}|-1\rangle)/\sqrt{2}$, where $\phi = \gamma_e B_{ext} t = \delta\nu \cdot t$. Measurement along the Φ axis are realized by applying a $(\pi/2)_\Phi$ pulse and optical measurement of the S_z spin component, yielding the occupational probability of $|m_s = 0\rangle$ state,

$$P(0) = \frac{1 - D\cos(\phi - \Phi)}{2}$$

$$\equiv \frac{1 - D\cos(\delta\nu \cdot t - \Phi)}{2} \tag{4.1}$$

where $D = \exp\left(-(t/T_2^*)^2\right)$ takes takes the decoherence into effect and $\delta\nu$ is the detuning

of the MW. Due to the finite Rabi frequency of 12.5 MHz relative to the detuning caused by the external magnetic field and the corresponding lengths of the MW pulses, the phase accumulated during the waiting time t is not given exactly by $\phi = \delta\nu \times t$. For small detunings, we may approximate $\phi = \delta\nu \times (t + t_{corr})$. We experimentally measure t_{corr} for various waiting times by measuring the Ramsey oscillations as a function of the detuning $\delta\nu$, fitting the data using Eq. 4.1, and find it to be approximately constant $t_{corr} \approx 28$ ns. Existence of this correction time can also be confirmed via numerical calculations (See Appendix D).

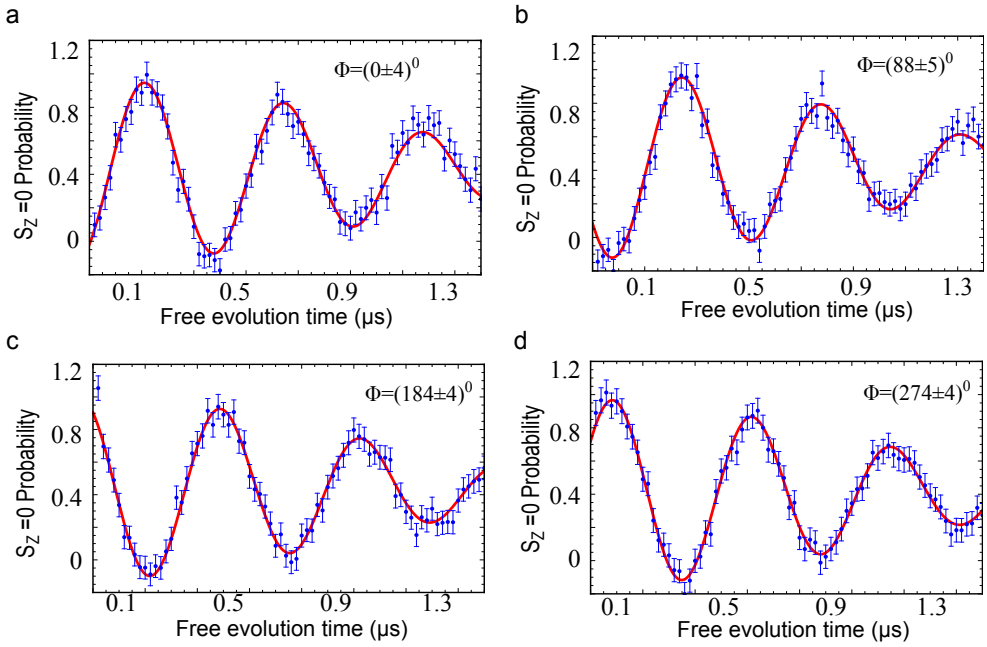

Figure 20: **a, b, c, d,** Ramsey fringes for the control phases of $0, \pi/2, \pi$ and $3\pi/2$. The solid (red) curves give the least-square (χ^2) fit for a function in the form $[(1 - D\cos(\delta\nu(t + t_{corr}) + \Phi)]/2$ where $\delta\nu = 2$ MHz is the detuning of the MW, and $t_{corr} = 28$ ns is the correction due to finite pulse widths. The evaluated control phases of **a-d** from the fit functions are $(0 \pm 4)^0$, $(88 \pm 5)^0$, $(184 \pm 4)^0$, and $(274 \pm 4)^0$ respectively. Error-bars are calculated assuming Poison statistics for the photon counts (See Appendix D for more details). The reduced chi-squared values (χ^2_{red}) of **a-d** are 0.85, 0.69, 0.61, and 0.42 respectively. Each measurement consists of $R = 50k$ repetitions of the MW pulse sequence (See Appendix D). Each data point in each figure is an average of 20 such measurements. With all the delays in the data acquisition process, each plot would approximately take ~ 15 minutes to complete.

In the NAPEA measurements, we have generated the MW pulses of different phases such as $0, \pi/2, \pi$ and $3\pi/2$. Power splitters/combiners and RF switches are used for this

purpose. Overall experimental timing sequence is controlled by a pulse programmer (SpinCore PulseBlasterESR-Pro 400MHz). We determine the feedback phases experimentally using Ramsey fringes, which are shown in Figure 20 . For the magnetic field estimation, a current was applied to a solenoid coil mounted near the diamond sample. Slow drifts in magnetic field during the experiment are compensated (by adjusting the MW frequency) to avoid the experimental imperfections in the variance of a single measurement. This is done by tracking the frequency of electron spin resonance. Figure 21 shows the general experimental scheme used in this chapter.

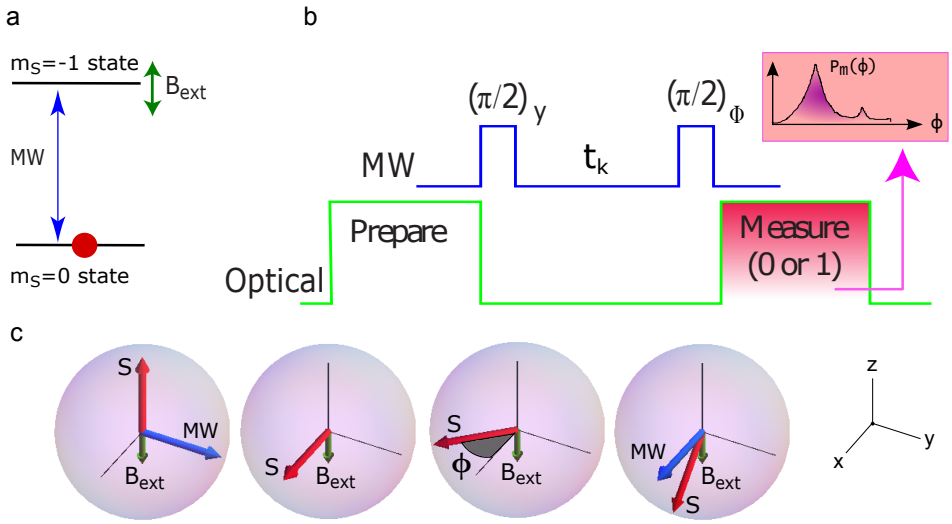

Figure 21: **Experimental scheme: a,** Energy level diagram of the NV center showing the working MW spin transition that is sensitive to the external field (B_{ext}). **b,** Pulse sequence used in standard measurements or PEA to estimate B_{ext}. Blue lines represent microwave (MW) fields used for coherent control of the spin, and green lines the optical fields for preparation and measurement. Standard measurements keep t_k and Φ fixed, whereas PEA vary both. **c,** Illustration of the sensing approach on the Bloch sphere, where the spin vector is labeled **S** and $\mathbf{B_{ext}}$ represents the magnetic field to be sensed. In the rotating frame of the MW field, the spin vector **S** will precess around the field accumulating a phase ϕ, while the MW remains fixed. The second $\pi/2$ pulse, depending on the control phase Φ (set to 90° in this figure and therefore MW field direction is $\hat{n} = \hat{x}$), rotates the spin vector onto the zn-plane. The probability to measure $m_s = 0(-1)$ is provided by the length of the spin vector projected to the z-axis.

4.2.1 Position and resonance tracking

Due to instabilities in the environmental conditions such as temperature fluctuations in the laboratory, the position of the NV relative to the confocal focus as well as the resonance frequency of the working transition can drift over the time of the experiment. Therefore, the LabVIEW program written for the experiment is also featured with the option of automated 'position tracking' as well as 'resonance tracking' routines. Whenever the photon counts in the 'reference' window goes below a certain user input value, the 'position tracking' routine will be called and will search for the NV by wandering the focus until it finds the maximum fluorescing point in the vicinity. In order this to succeed, the NV should be sufficiently isolated; i.e., a second NV should not exist within less than a $\sim$ 300 nm radial distance. The 'resonance tracking' is specially important when it comes to DC magnetometry. This routine is called in the program typically every 10-15 minutes. Under normal conditions, the typical drifts over an hour period in the laboratory temperature, position of the NV, and in the resonance is less than 0.2 ^{0}F, 1 μm, and 0.1 MHz respectively.

4.3 EXPERIMENTAL RESULTS

As described in Chapter 3, the SMS gives the field sensitivity (or precision) $\eta = \sqrt{(\Delta B)^2 T_{int}} = \sqrt{\frac{(\Delta\phi)^2 T_{int}}{\gamma_e^2 t_{min}^2}} \propto \sqrt{B_{max}}$. The trade-off between dynamic range and sensitivity is illustrated by a comparison of magnetic field sensing with short and long evolution times t. Figure 22a shows Ramsey fringes measured with a detuning $\delta\nu = 3$ MHz; the Gaussian coherence decay[105] ($T_2^* = 1.3$ μs) limits the maximum useful interaction time. Using a short interaction time ($t_{min} = 12.5$ ns, Figure 21b) yields a field detection range of approximately ± 0.15 mT, but provides mediocre sensitivity. In contrast, optimal sensitivity is obtained near $t = 800$ ns (Figure 22c), but the fast oscillations in the magnetic field clearly illustrate the limited dynamic range. Equivalently, this may be viewed in the frequency domain: increasing the measurement bandwidth ($\propto 1/t_{min}$) to detect large field-induced shifts results in sampling the wings of the spectral response (Figure 22a inset), thereby reducing the Ramsey sensitivity

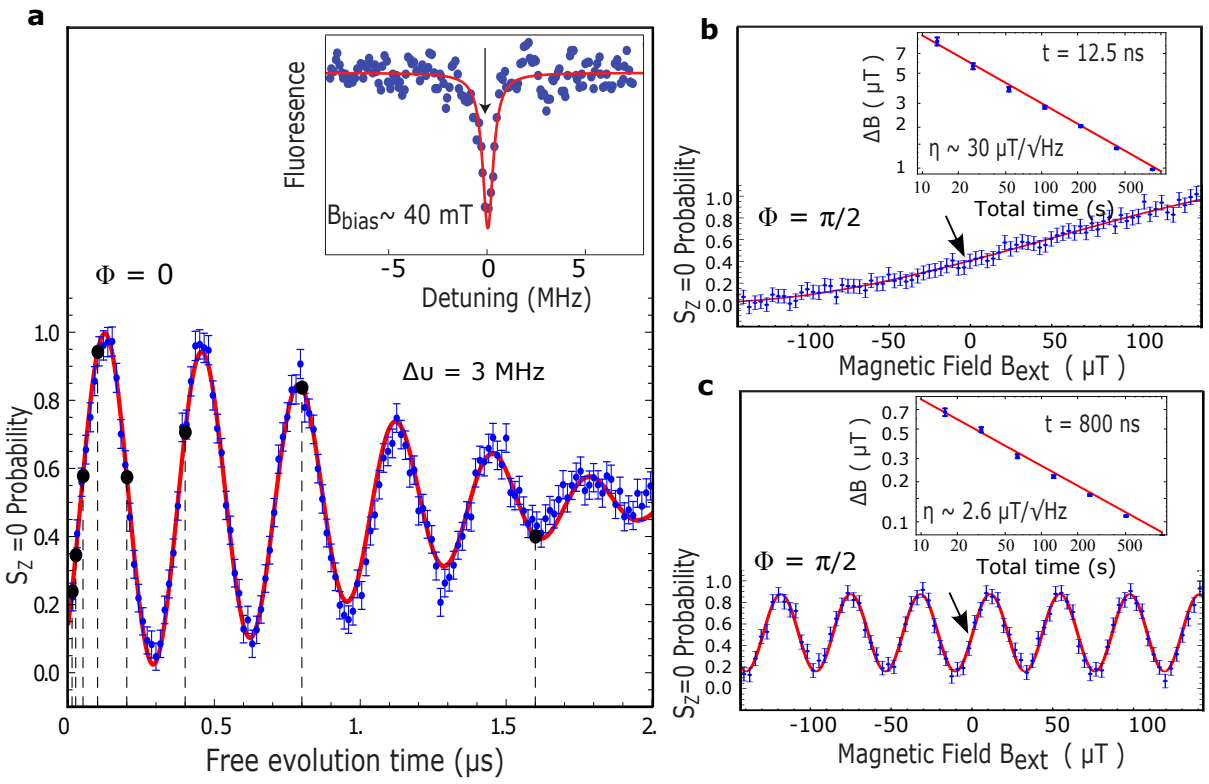

Figure 22: **Magnetic sensing with Ramsey fringes: a,** Ramsey fringes as a function of evolution time for finite detuning (external magnetic field). Error-bars indicate errors due to Poisson statistics and the thick red line is a fit to the data using Equation 4.1. Here $\delta\nu = 3$ MHz, $T_2^* = 1.3\ \mu$s. The goodness of the fit is $\chi^2_{red} = 0.9$. Each measurement consists of $R = 50k$ repetitions of the MW pulse sequence and each data point is an average of 50 such measurements. The black dots (dashed lines) represent the times sampled in the PEA. (right inset) ODMR spectrum showing position of the resonance under an applied bias magnetic field $B_{bias} \sim 40$ mT. **b & c,** Probability as a function of the applied external magnetic field B_{ext} for $t = 12.5, 800$ ns respectively. The arrows denote the field at which the sensitivity was measured. The insets show the scaling of the field precision as a function of the total time (including NV preparation and measurement time) of the experiment, showing that the largest dynamic range corresponds to largest SMS.

as well as that of equivalent absorption or modulation spectroscopy sensing methods.

As explained above, the best sensitivity for standard measurements is obtained with the longest accumulation time (consistent with decoherence), and the best field range with the shortest time; the optimal strategy should therefore coherently accumulate the results

of sampling between the shortest and the longest times. PEAs indeed choose the varying evolution times $t_k = 2^{(k-1)}t_{min}$, where $k = 1, 2, \ldots K$, in such a way as to remove phase ambiguity, combined with an optimal choice of measurements to overcome the SMS. This is done either by feed-forward of measurement phases, thus negating the independence of the measurements, based on Bayesian analysis of measurement results (adaptive PEA)[90, 99], or by carefully weighted measurements $M(K, k)$ that cycle among a pre-defined set of measurement phases (non-adaptive, NAPEA)[89, 90, 88]. Because NAPEA requires no feed-forward, we have chosen to implement it for this work.

4.3.1 Phase likelihood distribution from NAPEA

Every trial of the algorithm yields an *a posteriori* probability distribution function $P_m(\phi)$ for the phase, which is obtained through a Bayesian analysis based on the measurement results and the probability distribution for the Ramsey oscillations. The likelihood function ($\log(P_m(\phi))$ for one trial of the algorithm as K is varied is shown in Figure 23a. Here ϕ is the unknown phase to be estimated, and we use the maximum likelihood estimator (ϕ_{MLE}). The extra peaks in the likelihood function as K is increased represent the phase ambiguity caused by the longer accumulation times when the phase wraps around the fundamental interval. We are able to determine unambiguously ϕ_{MLE}, because these other peaks are greatly suppressed by the NAPEA. The inset to Figure 23a shows how ϕ_{MLE} changes in each trial for a fixed K. Although one trial is sufficient to yield the variance of the MLE from the probability distribution, we increase the number of trials to find this variance directly from experiments, as shown in the histogram of Figure 23b. Figure 23c shows that ϕ_{MLE} is a good estimator: varying B_{ext} causes the MLE to vary linearly over the range $(-\pi, \pi]$ for different choices of t_{min} and fixed choice of K, and allows us to tune the dynamic range of the sensor. The linear response of the sensor may prove useful for practical applications, in contrast to the non-linear (sinusoidal) dependence of the Ramsey signal on the applied field. The slope of the lines is in good agreement with theory, and conversion to B_{MLE} shows that the sensor readout is reliable for fields $B_{ext} \approx \pm 0.3$ mT. The deviation at larger magnetic fields is only due to the technical limitations of our set-up, as discussed in Section 4.3.3.

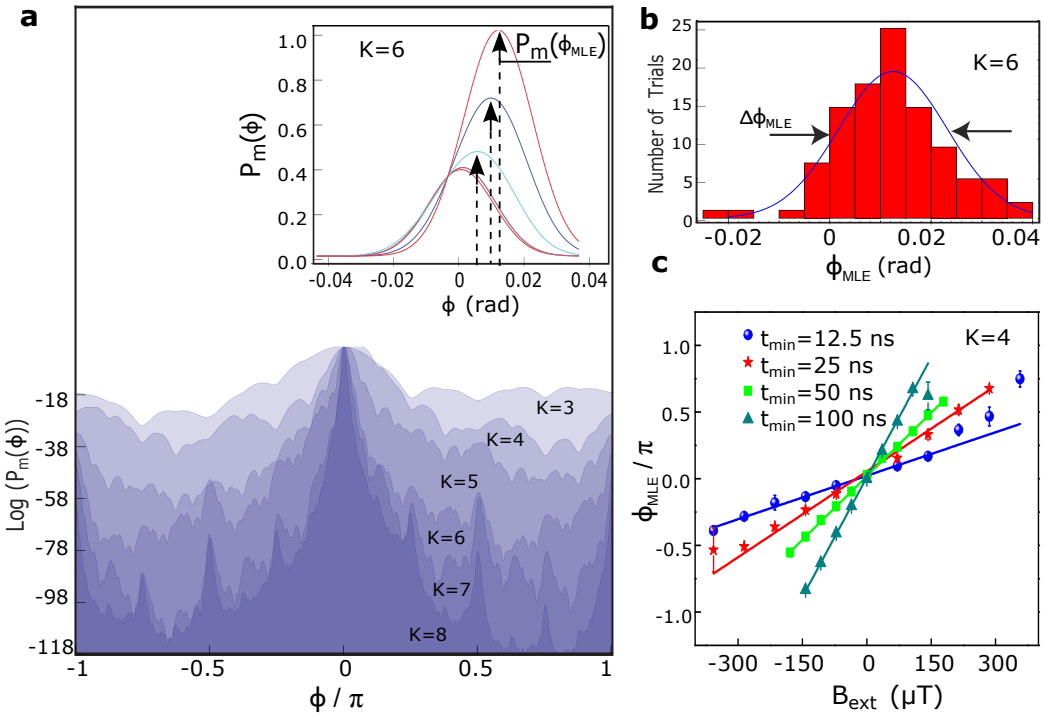

Figure 23: **Non-Adaptive Phase Estimation Algorithm (NAPEA) results: a,** Likelihood function ($\log(P_m(\phi))$) obtained as the number of resources is varied by varying the parameter K. Shaded regions represent evolution of the probability with progressively increasing resources, with the MLE being obtained from the peak of the distribution. (inset) magnified view of the probability distribution for K=6, showing how the MLE is obtained unambiguously for different trials. **b,** Histogram of obtained estimates for $K = 6$ as the number of trials is increased, with a Gaussian distribution parametrized by the mean and variance of the estimates superimposed. **c,** Variation of the MLE as a function of the applied external field for $t_{min} = 12.5, 25, 50, 100$ ns with $K = 4$, demonstrating the expected linear dependence with field and t_{min}.

4.3.2 Scaling of the field variance with resources

We now turn to the scaling of the field variance with the interaction time T_{int}, which depends both on K and $M(K, k)$ for the NAPEA. Figure 24a shows the field sensitivity $\eta^2 = (\Delta B)^2 T_{int}$ as a function of the interaction time (or number of resources N), where the field variance $(\Delta B)^2 = (\Delta\phi)^2/(\gamma_e t_{min})^2$. As expected, the field precision for standard measurements does not change with the interaction time. Furthermore, the theoretical SMS calculated by taking into account our experimental conditions is plotted in Figure 24a and agrees well with the experimental data. The NAPEA clearly shows sub-SMS scaling (with

slope $m = -0.77$), and beats the SMS at the longest interaction times, before starting to increase. The increase occurs because once the longest time in the protocol $2^{(K-1)}t_{min} \sim T_2^*$, no new information about the field is acquired, and thus there is no improvement in the variance as K is increased. This situation is again somewhat analogous to entanglement-based sensing[45, 106], where the greatest improvements are usually obtained for shorter interaction times. Furthermore, in contrast to Ramsey measurements, the inset to Figure 24a illustrates the advantage provided by the NAPEA, which has a constant high precision across a wide dynamic range. Finally, we emphasize that we are comparing the NAPEA results to the SMS, under the same experimental conditions. Although technical improvements such as a higher collection efficiency through the use of nanophotonic devices[33] would thus greatly improve the SMS sensitivity, they would also improve the NAPEA results accordingly.

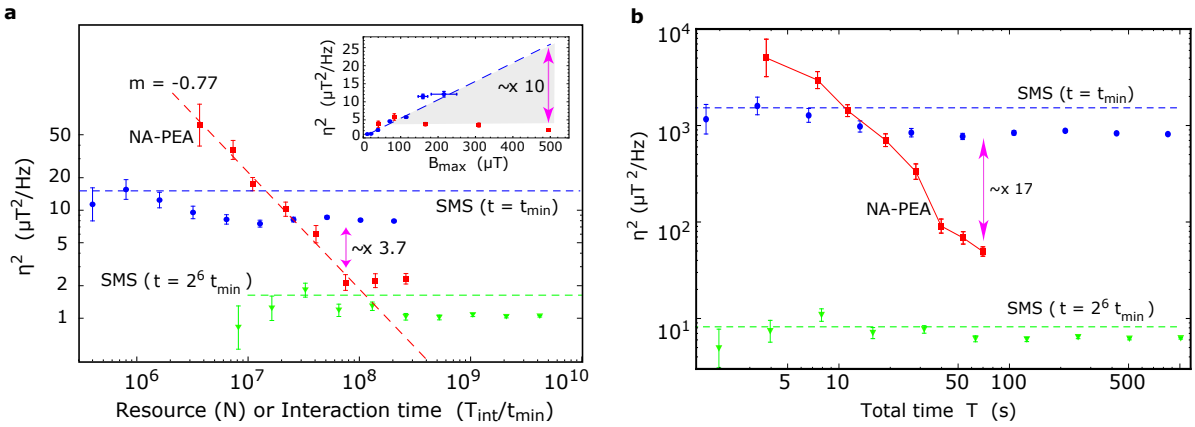

Figure 24: **Comparison of precision scaling with resources:** **a,** Variance of the magnetic field estimates multiplied by the interaction time $\eta^2 = (\Delta B^2)T_{int}$ in units of μT^2/Hz obtained as a function of the resource ($\equiv Nt_{min}$) is shown for Ramsey measurements (blue dots) and NAPEA (red squares) for the same $t_{min} = 12.5$ ns . Blue (green) dashed lines denote the numerical calculation of the SMS for different t. The red dashed line is a fit to the PEA data, showing sub-SMS scaling with slope $m = -0.77$. Green triangles are the data obtained from Ramsey measurements with $t = 2^6 t_{min} = 800$ ns. **b,** Square of the field sensitivity, $\eta^2 = (\Delta B^2)T$, where T is the total time as explained in the text and Methods. The gain for the NAPEA relative to the standard measurement is much greater because the PEA spends more of the total time in sensing when the measurement time is large compared to the interaction time. Error bars, representing one standard deviation of the results, were obtained using the bootstrap method (see Appendix D).

The field sensitivity improvement (η_{SMS}/η_{NA}) obtained as a function of the interaction

time is ~ 2.8 dB with our protocol. However, as shown in Figure 24b, the enhancement can be much greater when the time required for measurements of the spin is a significant fraction of the total time available as a resource. For many practical applications, the relevant time is the total time to reach a given precision, including any overhead required for preparation and measurement of the sensor. The overhead for the NAPEA is then given by T_M, and the total time is $T = T_{int} + T_M$. When the field sensitivity is now calculated using the total time $\eta^2 = (\Delta B^2)T$, Figure 24b shows the improvement $\eta_{SMS}/\eta_{NA} \sim 6.25$ dB. This demonstrates one of the key advantages of the PEA that has already been pointed out[99, 88]: when measurement time is important, the PEA will win because it spends a larger fraction of its time in sensing the field than the standard measurement technique with the same dynamic range. The ratio B_{max}/η can then be seen to improve by nearly an order of magnitude (~ 8.5-fold) with respect to the standard measurement approach.

4.3.3 NAPEA sensor readout

The sensor readout B_{MLE} is calculated using the equation below:

$$B_{MLE} = \phi_{MLE}/(2\pi\gamma_e t_{min}) \tag{4.2}$$

where, $\gamma_e \approx 28$ GHz/T is the gyromagnetic ratio of the NV. B_{MLE} values are in reasonable agreement with B_{ext} fields for $K = 4$ (see Figure 25a). However the deviation of the data for large external fields probably arises from the fact that the detuning of the resonance becomes comparable to the Rabi frequency of the MW pulses, resulting in imperfect rotations of the Bloch vector in our experiments. This is purely a technical limitation, that could be overcome by better MW strip lines or using high power MW amplifiers. Alternatively, we could avoid the finite pulse length effect by using a reduced free precession time interval (t'_k) to compensate the additional correction time due to finite MW pulse length: $t'_k = t_k - t_{corr}$. The minimum free precession interval that we could reach down to ($t'_1 = 12.5$ ns) is merely a technical limitation of the pulse programmer used in our experimental set-up. A sensor readout with this approach for $t_{min} = t_1 = 40$ ns and $K = 5$ is shown in Figure 25b . The readout shows an improved result for higher magnetic fields. However, this does not change the results for small external fields.

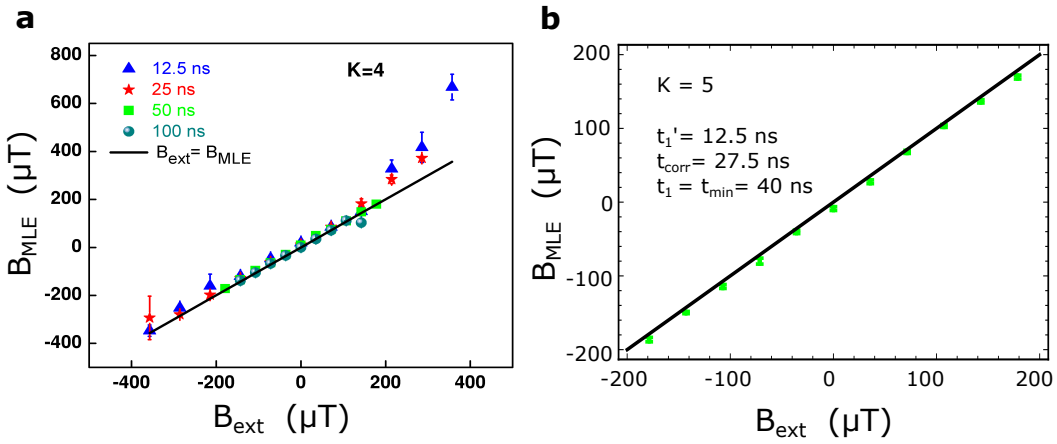

Figure 25: **a,** Sensor readout for $K = 4$ and $t_{min} = 12.5, 25, 50$ and 100 ns. The black line shows the agreement between the external magnetic field and the sensor readout($B_{ext} = B_{MLE}$).**b,** Sensing performed with the corrected free precession time intervals: $t'_k = t_k - t_{corr}$.

4.4 CONCLUSION

In conclusion, we have demonstrated decoherence-limited magnetic sensing with single electronic spin qubits in diamond over a field sensing range of $\sim \pm 0.3$ mT. The results should find immediate application in demonstrated nanoscale magnetic sensing and imaging techniques with the electron spin of the NV center[5, 107], and may also open the way for the application of other quantum feedback and control techniques to magnetometry. Mapping the electron phase onto the nuclear spin before measurement, as demonstrated for quantum memory applications[108], might allow better sensitivity. Although we have carried out static field sensing in this work, it should be possible to extend our methods to fluctuating magnetic fields as well[3], where the longer T_2 times obtainable through dynamic decoupling techniques[109, 110] may allow much better sensitivity.

5.0 DUAL-CHANNEL LOCK-IN MAGNETOMETRY

5.1 INTRODUCTION

The coherent evolution of a quantum state interacting with its environment is the basis for understanding fundamental issues of open quantum systems[111], as well as for applications in quantum information science and technology[112]. Traditionally in these fields, the extreme sensitivity of coherent quantum dynamics to external perturbations has been viewed as a barrier to be surmounted. By contrast, quantum sensors have emerged that instead take advantage of this sensitivity; recent examples include electrometers and magnetometers based on superconducting qubits[1], quantum dots[2], spins in diamond[3, 4, 5, 6] and trapped ions[18].

5.1.1 Dynamical decoupling for sensitive Magnetometry

Magnetometry with diamond spin sensors detects the frequency shift of the NV spin resonance caused by the magnetic field via the Zeeman effect. Highly sensitive quantum sensing techniques use multi-pulse dynamical decoupling (DD) sequences[4, 18, 19, 20, 1, 23] that are tuned to the frequency of a time-dependent field. The resulting fluctuating frequency shift is rectified and integrated by the pulse sequence to yield a detectable quantum phase, while effectively filtering out low frequency noise from the environment (Figure 26b). Another advantage of these DD sequences is that they make the magnetometer less sensitive to instabilities such as drifts in temperature or applied bias magnetic field as described below.

5.1.1.1 Robustness of dynamical decoupling against instabilities

In order to investigate the effect of instabilities such as fluctuations in the temperature and/or bias magnetic fields, let's consider the Hamiltonian for the NV interacting with an external DC bias magnetic field B_0, and the microwave field B_{MW}.

$$H = DS_z^2 - \gamma_e B_0 S_z + \gamma_e S_x B_{MW} \cos(\omega_{MW} t) \tag{5.1}$$

where, $D \approx 2.87$ GHz and $\gamma_e \approx 28$ GHz/T are the zero-field splitting and the gyromagnetic ratio of the spin respectively. In the rotating frame picture and rotating wave approximation (RWA), the effective Hamiltonian is simplified to,

$$H = \delta S_z + \Omega S_x \tag{5.2}$$

where $\delta = \omega_S - \omega_{MW}$ is the detuning of the MW with respect to the working transition and $\Omega = \gamma_e B_{MW}/\hbar$ is the Rabi frequency of the transition. Consequently, a MW spin-echo pulse, $-\tau/2 - \pi - \tau/2-$ will bring a superposition state $|+\rangle = (|0\rangle + |1\rangle)/\sqrt{2}$ to $(e^{-i\delta_1\tau/2}|0\rangle - e^{-i\delta_2\tau/2}|1\rangle)/\sqrt{2}$ where the $\delta_{1(2)}$ are constant detuning before (after) the MW π pulse. Therefore, the spin always ends up in the same state $|-\rangle = (|0\rangle - |1\rangle)/\sqrt{2}$ provided that the detuning remains constant through out the spin-echo sequence. In other words, spin-echo can remove the effect of a detuning as long as the detuning is constant within a spin-echo sequence. DD shares the same robustness of spin-echo.

The temperature dependence of the zero-field splitting is approximately $\epsilon \approx -74$ kHz/K and effectively changes the detuning[13].

$$\delta = \delta_0 + \epsilon(\Theta - \Theta_0) \tag{5.3}$$

However within the time of a spin-echo sequence, the temperature (Θ) remains essentially a constant and has no effect on the final spin state. This is because the typical time scale for spin-echo sequence here is several micro-seconds while the temperature fluctuations occur on minute time scale.

The temperature fluctuations can affect the spin-echo but only in an indirect fashion. The effective Rabi frequency in the presence of a MW detuning is given by,

$$\Omega_{eff} = \sqrt{\Omega^2 + \delta^2} \approx \Omega\Big(1 + \frac{\delta^2}{2\Omega^2}\Big) \tag{5.4}$$

Therefore, although the MW was originally tuned to the resonance, the temperature can cause a second order effect on the π pulses.

$$\Omega_{eff} \approx \Omega\Big(1 + \frac{\epsilon^2(\Theta - \Theta_0)^2}{2\Omega^2}\Big) \tag{5.5}$$

For a 1^0C change in temperature (which is typical in laboratory conditions) the effective Rabi frequency differs only by $\sim 1.7 \times 10^{-5}$ from the working Rabi frequency of $\Omega = 12.5$ MHz.

5.1.2 AC magnetometry with PEA

The state of the art quantum sensing methods have significant drawbacks: the dynamic range is limited by the quantum phase ambiguity[86, 90], the sensitivity is a highly non-linear function of field amplitude requiring prior knowledge of a working point for accurate deconvolution, and the classical phase of the field has to be carefully controlled to obtain accurate field amplitude[4]. In this work, we present an experimental method that incorporates the DD sequences with phase estimation algorithms (PEA) to address these fundamental problems. Our dual-channel lock-in magnetometer has linearized field readout and nearly decoherence-limited constant sensitivity, while offering significantly greater dynamic range. We demonstrate unambiguous reconstruction of the amplitude and phase of the magnetic field without prior knowledge of either value. Finally, we show that our technique can be applied to measure random phase jumps in the magnetic field, and to obtain phase-sensitive field frequency readout.

As demonstrated by conventional electronic lock-in techniques, phase information is often extremely useful in measuring important physical processes such as relaxation lifetimes[113], spectral and spatial diffusion[114, 115]. Dynamic range and constant sensitivity may be helpful in accurate measurements of small magnetic fields due to spins in nanoscale volumes[40, 41], in quantitative high-speed imaging of time-dependent magnetic field profiles[98], and in measuring spin density of heterogeneous samples at low magnetic fields, where different magnetic species are not well resolved in frequency space. Observables like the field phase and frequency may also be useful in situations where the target spins are hard to polarize or to drive[66, 116]. Random phase and spin configuration approximations are often made to theoretically deal with this problem and thereby retrieve the field

amplitude[117, 19, 41, 40], but it remains to be verified if these approximations are valid experimentally in samples of interest[118]. Thus, our methods open up the potential for new modes of magnetometry with NV spin sensors, as well as for other quantum sensors.

The important feature of PEAs that permits this reconstruction is reminiscent of a Fourier series in the quantum phase ϕ. Indeed, PEAs were first introduced for the purpose of performing a quantum Fourier transform in Shor's algorithm. The quantum circuit representation of our PEA is shown in Figure 8b in Chapter 2. The spin qubit is first initialized into the $|+\rangle = (|0\rangle + |1\rangle)/\sqrt{2}$ state, while the auxiliary qubit is initialized into the state $|\phi\rangle$ where ϕ is the quantum phase to be estimated. The action of the controlled-U^n gate on the auxiliary qubit register is $U^n|\phi\rangle = e^{in\phi}|\phi\rangle$, resulting in the combined state

$$\frac{|0\rangle + e^{in\phi}|1\rangle}{\sqrt{2}}|\phi\rangle$$

Measurements are carried out in the set of basis states $\{|\Phi\rangle\}$ and the resulting probability distributions are combined using Bayesian analysis to obtain an estimate for the state $|\phi\rangle$. Since the auxiliary registers are not measured, they can be replaced by a classical drive field that causes the phase shift shown above on the control qubit, and the corresponding quantum phase allows us to estimate the classical drive field. Our implementation of the PEA is discussed below, after we introduce our experimental system and quantum sensing with DD sequences.

Our magnetometry set-up is shown schematically in Figure 26a. As stated in Chapter 4, a static magnetic field B_0 oriented along the NV centers z-axis is applied, allowing us to form a pseudo-spin $\sigma = 1/2$ qubit system with the $|m_s = 0\rangle \leftrightarrow |m_s = -1\rangle$ spin states.

5.1.3 Quantum phase in AC magnetometry

The Hamiltonian for a spin-1/2 qubit interacting with an external magnetic field $b_z(t)$, while being driven with on-resonance electromagnetic fields is given in the rotating frame by $H = \gamma_e b_z(t)\sigma_z + \Omega(\sigma_x \cos\Phi + \sigma_y \sin\Phi)$. Here $\gamma_e \approx 28$ GHz/T is the gyromagnetic ratio of the spin, Ω is the Rabi frequency of the on-resonance drive field and Φ is an adjustable control phase of the microwave. An oscillating magnetic field $b_z(t) = b_{ac}\cos(2\pi f_{ac}t - \theta)$ can be

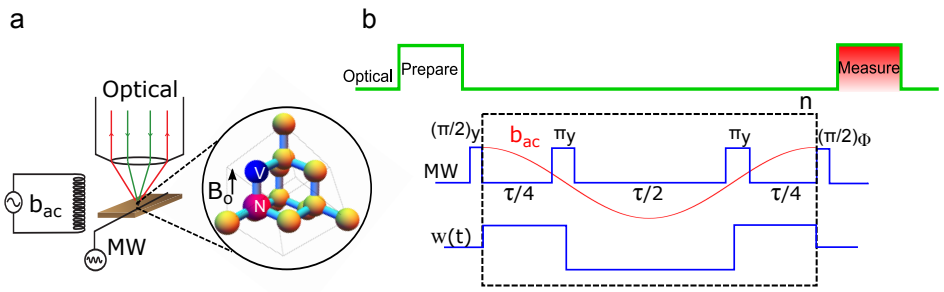

Figure 26: **a,** Illustration of experimental setup for NV magnetometry. A solenoid magnet coil with inductance $\approx 0.3mH$ is placed near the sample. A signal generator connected to this coil provides the AC magnetic field to be measured. (See Appendix E for more details) **b,** Carr-Purcell (CP) sequences with even number $2n$ ($n = 1, 2, \ldots$) of π pulses, are used to detect oscillating magnetic fields $b_z(t) = b_{ac}\cos(2\pi f_{ac}t)$ where f_{ac} is the AC field frequency. Here, $\pi/2$ (π) microwave pulses cause corresponding rotations of the spin vector, Φ is an adjustable control phase and $w(t)$ represents the CP filter function with reference frequency $\omega_0 = 2\pi/\tau$.

measured by the Carr-Purcell CP-$2n$ ($n = 1, 2, \ldots$) sequence, as shown in Figure 26b. Here, $w(t)$ is the DD filter function of the CP sequence[4, 119, 120, 121] with reference frequency $\omega_0 = 2\pi/\tau$.

The collapses and revivals in the signals due to ^{13}C nuclear spins in our sample, shown later in this chapter, restricts the allowable values of the filter reference frequency $\omega_0 = \omega_L/(2p)$ where $p = 1, 2, \ldots$ is an integer, $\omega_L = \gamma_n B_0$ is the ^{13}C Larmor frequency, $\gamma_n = 10.705$ MHz/T is the ^{13}C nuclear gyromagnetic ratio. We can then detect the in-phase magnetic field ($b_I = b_{ac}\cos\theta$) by measuring the probability $P(0)$ to be in $|m_s = 0\rangle$;

$$S(b_I) = 2P(0) - 1 = D(n\tau)\cos(n\phi_I - \Phi) \tag{5.6}$$

and the quantum phase

$$\phi_I = \int_0^\tau \gamma_e b_z(t) w(t) dt = 2\gamma_e b_I \tau/\pi \tag{5.7}$$

where $D(n\tau) = \exp(-(n\tau/T_2^{(2n)})^3)$ is the decoherence function, and $T_2^{(2n)}$ is the effective coherence time under the DD pulse sequence[4, 19, 20].

The quantum phase ϕ_I is ambiguous due to the multi-valued inverse sine or cosine functions, requiring us to restrict its range to $(-\pi/2n, \pi/2n)$. We also need to know the classical phase θ to obtain b_{ac} or vice-versa. Furthermore, even if the classical phase is known, the dynamic range is limited by the above restriction on ϕ_I, as shown in Figure 29a. The sensitivity improves with higher number n of π pulses, but correspondingly only a small range of fields can be sensed. As shown by the data in Figure 29b, when the classical phase θ is allowed to vary, magnetic field values that differ by factors of 2 (or even 10) could yield the same signal.

In a conventional electronic single channel lock-in amplifier, simply tuning the phase of the reference channel to minimize or maximize the signal would allow us to find the amplitude and phase of the input signal. However, that requires a linear readout of the quantum phase ϕ_I which is not available directly for the CP sequences. Further, in quantum sensing, the relevant reference phase corresponds to that of the DD filter function $w(t)$, and one must adjust the timing offset of the sequence for each frequency that has to be detected. Previous works such as Refs.[18, 4, 3, 19, 20] carried out this phase adjustment, usually by carefully modulating the signal AC field, to $0(\pi/2)$ prior to measurement. Practical situations where the magnetic field arises from unknown samples may prevent this phase adjustment and result in inaccurate measurements which we address here.

Linearizing the signal could be accomplished under the assumption that both b_{ac} and θ are small, and by choosing the control phase $\Phi = \pi/2$. Alternately, one can choose a working point with finite b_{ac} and $\theta = 0$ (see Figure 29a) and look for deviations from this point. By recording and averaging the fluorescence measurements separately at these carefully adjusted working points we get the sensitivity,

$$\eta = \frac{1}{V\sqrt{\xi}} \frac{\pi}{2\gamma_e \sqrt{n\tau} D(n\tau) |\cos(n\phi_I)|} \tag{5.8}$$

where $V \sim 0.3$ is the fringe visibility, and ξ is a factor that depends on the photon collection efficiency in our system [4, 16]. Through prior knowledge of the working point, it is assumed that $n\phi_I \approx 2m\pi$ and this requirement will be more stringent as n increases [4]. Thus, the minimum detectable field and corresponding deconvolution of the target spin positions will depend on this knowledge. Lastly, we note (and show below) that the dependence on

the frequency of $b_z(t)$ for the CP pulse sequences is symmetric around the lock-in reference frequency $\omega_0 = 2\pi/\tau$, implying that frequency changes of the field are also ambiguous.

Overcoming the multiple ambiguities of the quantum phase caused by uncertainty in the parameters of the external magnetic field is thus an important step. Recently, phase estimation algorithms (PEAs) were introduced for DC magnetic field sensing with single spins in diamond[88, 16, 122]. We first extend these results and demonstrate significant improvement in the dynamic range and linearization of the field readout, by combining the DD pulse sequence ($CP-2n$) with PEA.

5.2 EXPERIMENTAL RESULTS

In our application, the DD pulse sequence times are first increased in powers of 2 (i.e. $n = 2^{k-1}$ with $k = 1, \ldots, K$) starting with an initial time that is determined by the fundamental reference frequency (ω_0) that one wishes to sense. This results in phase accumulations $\phi_k = 2^{k-1}\phi$ at each step of the PEA. Secondly, measurements with the smallest times, and therefore poorer sensitivity are corrected by repeating them several times. This is analogous to the coefficients in a Fourier series with weighting factors $M(K,k) = M_K + F(K-k)$, where M_K, F are optimized through numerical simulations (see Appendix E and Refs.[90, 88]). Finally, the control phase of the readout pulse is cycled through several values to measure along different basis vectors, thus allowing to differentiate between quantum phases that differ by fractions of π. These steps are combined with digitization of the signal levels, and Bayesian maximum likelihood estimation (MLE) to obtain unambiguous knowledge of the field value. See Appendix E for description of the Bayesian estimation process[88, 16, 122].

5.2.1 Larmor revivals due to ^{13}C nuclear spin bath

The ^{13}C nuclear spin bath that has a natural abundance of $\approx 1.1\%$ effectively produces a random field with frequency set by the nuclear gyromagnetic ratio $\gamma_n = 2\pi(10.75)$ MHz/T and the DC bias field B_0. This random field causes collapses and revivals in the CP signals

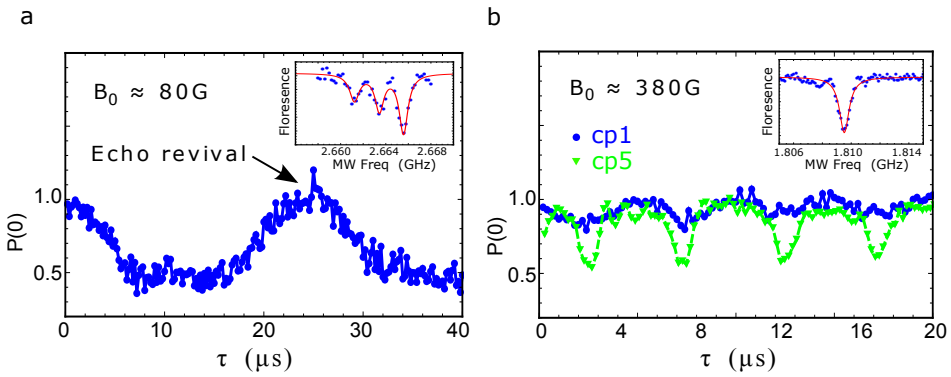

Figure 27: Larmor revivals at **a**, $B_0 \approx 80$ G and **b**, $B_0 \approx 380$ G. These revivals occur due to the effective random magnetic fields arising from Larmor precession of the ^{13}C nuclear bath that has a natural abundance of $\approx 1.1\%$. The insets show the corresponding ODMR spectrum for those bias fields. Magnetic fields near excited state level anti-crossing causes dynamic nuclear polarization of ^{14}N. For best results in AC magnetometry, it is required to operate on a revival point and this constrains the applicable AC field frequencies. Echo-revivals occur when $\tau = 2pT_L$ where, $p = 1, 2, 3 \ldots$ is an integer and T_L is the Larmor period of the nuclear bath field. Note that no external AC magnetic field was given here.

(Figure 27). For best results in AC magnetometry, it is required to operate on a revival point and this constrains the workable AC field frequencies to be $f_{ac} = \frac{1}{2pT_L}$ where, $p = 1, 2, 3 \ldots$ is an integer and T_L is the Larmor period of the nuclear bath field. Having a larger bias magnetic fields could be useful for AC magnetometry due to the fast revival rates and thus giving more flexibility in terms of workable AC magnetic field frequencies.

5.2.2 Coherence time enhancement due to dynamical decoupling

The enhancement of the coherence time with DD sequences has been extensively studied[109, 110, 20, 21] and not a main scope of this thesis. We use a fitting function,

$$(1 + D(T, T_2^{(m)}))/2 \tag{5.9}$$

where the $D(T, T_2^{(m)}) = \exp(-(T/T_2^{(m)})^\alpha)$ is the decay due to decoherence, $T_2^{(m)} = T_2 m^s$, and both α and s are sample dependent numbers which turn out to be $\alpha = 3$ and $s \approx 0.5$ in our case (Figure 28).

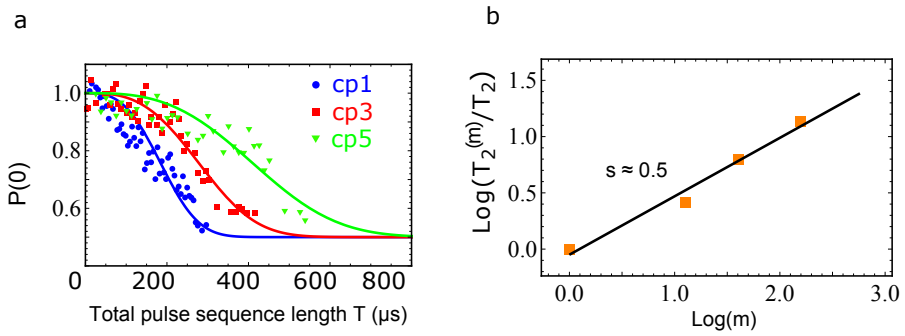

Figure 28: **a**, Due to dynamical decoupling an enhancement in the coherence time is observed. This in turn could be employed for better sensitivity in AC magnetometry. The solid lines are the best fitted curves for the function $[1 + D(T, T_2^{(m)})]/2$ where $D(T, T_2^{(m)}) = \exp[-(T/T_2^{(m)})^3]$ is the decay due to decoherence. **b**, The enhancement of coherence obeys a power law dependence: $T_2^{(m)} = T_2 m^s$, where $T_2 \approx 211$ μs is the coherence time of spin-echo (CP-1), m is the number of π pulses in the CP sequence and s is a sample-dependent number which turned out to be $s \approx 0.5$ in our case.

5.2.3 Readout of the AC magnetic field

The data in Figure 29c shows that our PEA unambiguously measures the value of the magnetic field with a linear readout over a wide range, and is also able to resolve phase shifts of π. We now turn to the comparison of the minimum detectable field $\Delta b = \eta/\sqrt{T}$ obtained in both approaches for some fixed averaging time T, where we chose $T = 150$ s as a typical time used in sensitive experiments[17, 40, 41]. As expected from Equation 5.8, the CP sequences show rapid degradation in Δb as soon as we deviate from the working point, for instance due to imperfect knowledge of θ. By contrast, Figure 29d shows that the sensitivity achieved by PEA remains almost a constant over a wide range of b_{ac} and is comparable to the longest CP sequence used in our work. The maximum detectable field ($\pm b_{ac,max}$) of the PEA is obtained by setting $\phi_I = \pm\pi$ in Equation 5.7,

$$b_{ac,max} = \frac{\pi\omega_0}{4\gamma_e} \tag{5.10}$$

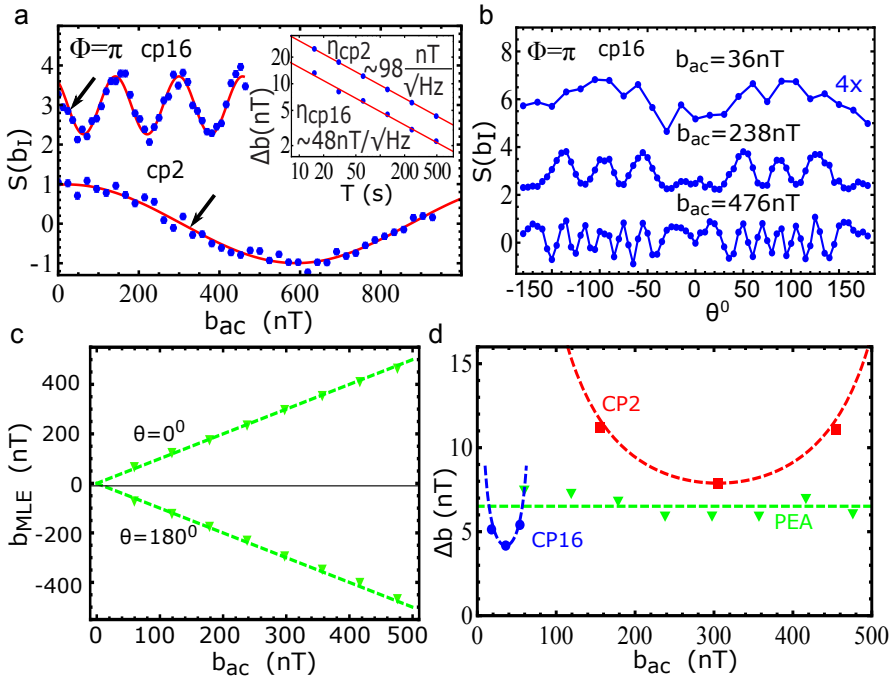

Figure 29: **a**, Magnetic field dependence of signal from CP-2 (CP-16) sequences, showing the trade-off between dynamic range and sensitivity. Arrows indicate the working points for the precision scaling plots in the inset. **b**, Variation in signal as function of θ from CP-16 sequences for different magnetic fields b_{ac}. Data has been offset and scaled for clarity. **c**, Maximum likelihood field estimate b_{MLE} from PEA vs. the applied drive field b_{ac} for $\theta = 0°, 180°$. Dashed lines represent ideal estimation $b_{MLE} = b_{ac}$. **d**, Variation in the minimum detectable field $\Delta b = \eta/\sqrt{T}$ vs. b_{ac} for CP sequences and PEA. Here $T = 150$ s. Dashed lines for CP sequences are fits to Equation 5.8. Data in this and all subsequent figures was taken with AC magnetic field frequency $f_{ac} = 20.83$ kHz while the applied DC bias magnetic field is $B_0 \approx 470$ G.

which in principle has no fundamental limit except for the restriction $\omega_0 = \omega_L/(2p)$ mentioned previously for our samples. The dynamic range (DR) is given by,

$$DR = \frac{b_{ac,max}}{\Delta b} \tag{5.11}$$

and from the data in Figure 29c, we obtain $\mathrm{DR}^{CP-16} \sim 3.4$, while $\mathrm{DR}^{PEA} \sim 90$. As shown in Appendix E, DR^{PEA} keeps increasing at higher frequencies, while by contrast, the DR^{CP} is essentially unchanged. High dynamic range can be especially important in imaging of unknown samples, as it allows for quantitative mapping of the magnetic field in a single run,

as shown recently for DC magnetic fields [98]. In Appendix E, we also discuss the potential importance of dynamic range to nanoscale magnetic sensing, and to recent work reported in Refs.[41, 40].

5.2.4 Dual-channel quantum lock-in scheme

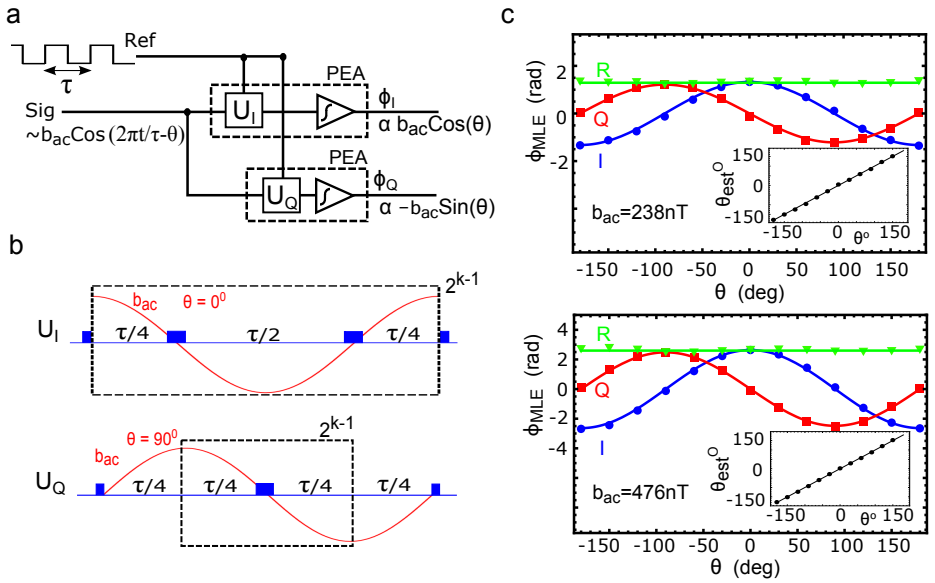

Figure 30: **a**, Schematic illustration of the quantum dual-channel lock-in magnetometer. Via unitary evolution of the single spin, the applied magnetic field is multiplied with the lock-in reference signal set by the DD pulse sequences. The PEA is implemented for each channel as before to linearize the readout and yield the I and Q quantum phases. **b**, DD pulse sequences for U_I and U_Q. **c-d**, Data for ϕ_I and ϕ_Q as θ is varied for different values of $b_{ac} = 238(476)$ nT. The estimator ϕ_R remains constant throughout, solid lines represent ideal sensing. (inset) Data for θ_{est} as function of θ, solid line represents ideal case $\theta_{est} = \theta$.

Our dual-channel quantum lock-in magnetometer scheme, shown schematically in Figure 30a, detects both in-phase $b_I = b_{ac}\cos\theta$ and quadrature components $b_Q = -b_{ac}\sin\theta$ of the magnetic field. As noted above, using CP sequences alone does not allow us to obtain both components unless we have excellent knowledge of both b_{ac} and θ. We further modify the PEA algorithm for lock-in detection by using both the CP-$(2n-1)$ and CP-$2n$ pulse sequence depicted in Figure 30b to obtain unambiguous information about the magnetic field quadratures. The former case is sensitive to $\theta = \pm 90°$, whereas the latter case is sensitive

to $\theta = 0(180)^\circ$. As shown in Figure 30c, we can determine for various b_{ac}, the estimators

$$\theta_{est} = \tan^{-1}(-\phi_Q/\phi_I) \tag{5.12}$$

$$\phi_R = \sqrt{\phi_I^2 + \phi_Q^2} \tag{5.13}$$

where $\phi_Q = 2\gamma_e b_Q \tau/\pi$ and thus reconstruct $b_{ac}^{MLE} = \frac{\pi\phi_R}{2\gamma_e\tau}$ independent of the value of θ.

The phase resolution of our lock-in magnetometer is given by the sample standard error of our estimator θ^{est} from the actual value θ used in the experiment,

$$\Delta\theta_{min} = \sqrt{\frac{1}{N(N-1)}\sum_{i=1}^{N}(\theta_{est,i} - \theta)^2} \tag{5.14}$$

which evaluates to $\Delta\theta_{min} = 0.3^\circ(0.6^\circ)$ for $b_{ac} = 476(238)$ nT respectively, for $N = 65$ samples. For ease of data analysis in our experiments, we carried out I and Q PEA routines successively, however this can easily be modified to have both sequences alternated within one PEA routine for near-simultaneous detection of the quadratures.

5.2.5 Applications

We now demonstrate two important applications of our dual-channel lock-in magnetometer. Earlier work has studied the effect of random classical phase on the magnetometry performance of DD sequences[117, 19]. However, these methods require theoretical assumptions on the nature of the random phase e.g. uniformly or normally distributed. In Figure 31a, we show that by monitoring the ϕ_I channel of our lock-in, we can observe random telegraph phase flips $0 \leftrightarrow \pi$ of the magnetic field. One physical scenario where such jumps might occur in the phase would be for measurements of single electron or nuclear spins where the spins cannot be easily polarized, but will be present in one state or the other for each measurement shot. Similarly, when nanoscale volumes of spins are measured experimentally[40, 41], one could use this protocol to verify that we sample all possible spin configurations by either periodically randomizing the ensemble or simply by waiting for long enough durations[118]. See Appendix E for data similar to such situations.

Our second application is for measurement of the frequency changes from the central working frequency $\omega_0 = 2\pi/\tau$. As shown in the inset to Figure 31b, the in-phase response of

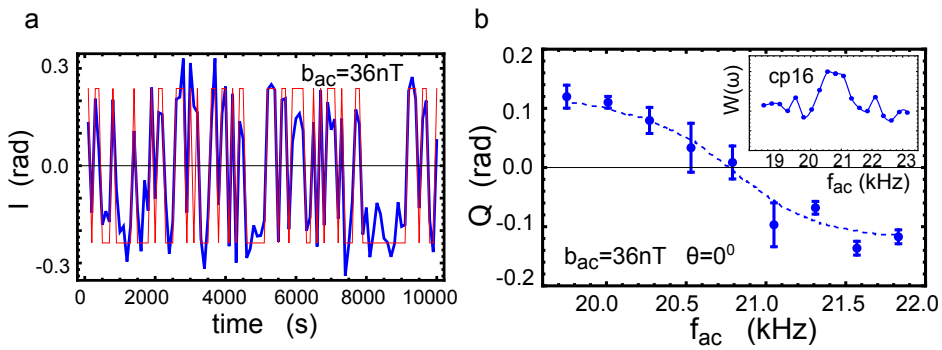

Figure 31: **a**, Observation of random telegraph phase jumps $0 \leftrightarrow \pi$ by monitoring the I channel of the lock-in. The time constant of the lock-in was set to ~ 100 sec, and the phase was held constant over this time but allowed to vary randomly between measurements. Thick (blue) lines represent observed phase, and thin (red) lines represent actual phase. **b**, Phase sensitive readout of frequency change in the magnetic field. (inset) Frequency response of CP-16 sequence.

the CP sequences is symmetric around ω_0. This is a fundamental feature of the corresponding filter functions $W(\omega) = \mathcal{F}\{w(t)\}$ of these sequences in the frequency domain[4, 19, 20]. However, when the frequency of the magnetic field changes, we can monitor the quadrature field component and obtain phase-sensitive readout of the change. This occurs because for small changes in frequency $\delta\omega$, the field $b_z(t) = b_{ac}\cos(\omega_0 t - \delta\omega t)$, and the corresponding quadrature component $b_Q = b_{ac}\sin(\delta\omega t)$ changes linearly with $\delta\omega$. Normally as t increases in the longest CP sequences, this phase change and corresponding component would be unrecoverable (see Figure 29b), but the excellent dynamic range of our method allows us to track the frequency as seen in Figure 31b. See Appendix E for simulations of the PEA when signals with equal amplitude but slightly different frequencies are used; demonstrating in principle that the PEA can distinguish such signals.

The typical relaxation time for target nuclear spins in fluid samples at room temperature is $T_1 \sim 1 - 40$ secs[123]. The time constant T for our lock-in magnetometer can be adjusted through different choices of parameters to fall within this range, as shown in Appendix E. However, previously demonstrated technical improvements such as nano-fabricated photonic structures can greatly improve collection efficiency[33, 37] and allow us to tune the time constant down to milleseconds, as discussed in Appendix E.

Lastly, we discuss again the importance of linear readout and dynamic range improvements of our technique. In nanoscale magnetometry and imaging, it may be possible to have some prior knowledge on the field amplitude b_{ac}, from estimates of the average number of spins and the distance from the NV sensor. Recently, Refs.[41, 40] have reported breakthrough results in detecting nanoscale volumes of nuclear spins through DD noise spectroscopy with NV quantum sensors. These authors have estimated rms field amplitudes $b_{ac} \sim 70 - 400$ nT for their samples and compared the estimates with NV sensor field measurements. Ref.[40] observed significant discrepancy between the measured field compared to the estimate ($\sim 700\%$), while Ref.[41] used numerical modeling of the nuclear spin volumes with "typical" proton concentrations and other assumptions and obtained agreement at the $\sim 70\%$ level. It is still unclear what causes the discrepancies, although the authors postulate uncertainty in either the NV position or the number of nuclear spins in the target volume leading to imperfect knowledge of the working point. While a direct comparison between our work and these results is not possible, the estimated fields are close to the maximum field amplitudes sensed in our work (see Figure 29d), and certainly well above that of the much longer DD sequences used by those authors. Since the sensitivity of the sequences crucially depends on this knowledge of the working point, we speculate that our methods might help in resolving some of these uncertainties. Further, since there is no restriction on the phase θ of the magnetic field, the reconstruction of the field amplitude may also have significant error if the dynamic range is limited, as we showed in Figure 29b. Our method simultaneously resolves both the working point and phase measurement problem.

5.3 CONCLUSION

In conclusion, we have reported a new quantum sensing method for magnetometry with phase estimation algorithms. Our results show significantly improved dynamic range and linearity of the readout for time-dependent magnetic fields, while preserving the increased sensitivity of DD pulse sequences. Our method also allows for unambiguous reconstruction of the amplitude, phase, and frequency of the oscillating field, and allows us to track the phase

in each measurement shot. This may open up the capability to study the spin configuration changes of nanoscale volumes of spins with unprecedented resolution. Additionally, when combined with scanned probe microscopy, the high dynamic range of our technique may permit imaging of oscillating magnetic field profiles in a single run over an unknown sample, as recently demonstrated with DC fields[98].

6.0 SUMMARY AND CONCLUSION

6.1 SUMMARY OF THESIS

Diamond spin megnetometry has emerged a promising candidate for nanoscale magnetic imaging. The two most critical aspects of nanoscale magnetometry are the magnetic field sensitivity and the probe-sample distance. In chapter 1, a brief survey on currently explored techniques for nanoscale magnetometry was presented in spite of these aspects.

In chapter 2, the basic physics of our experimental system is discussed. This includes discussion of the physics of NV centers, the experimental apparatus, and the use of NV centers for magnetometry. Application of PEA for magnetometry is also introduced in brief.

In chapter 3, we discussed the importance of dynamic range for magnetic imaging applications. A detailed study of PEA was performed via Monte-Carlo simulations. The role of control phases in NAPEA was studied and the DUAL and QUAD set of control phases were shown to be equivalent. Although a weighting scheme can play a role in NAPEA, existence of a non-weighted choice of PEA parameters for optimum results was also explored. Optimum parameters, in general, depend on the measurement fidelity. The best results in NAPEA are, however, shown to be guaranteed for measurement fidelity above $\sim 90\%$. On the other hand, QPEA showed a significant variation in the sensitivity across the full field range as a consequence of the binary bit-error in the readout. The best results in QPEA demands extremely high fidelity $\sim 99\%$. Because multiple measurements are not required, the total estimation time for QPEA is less, compared to in NAPEA. However, NAPEA is superior to QPEA due to (a) better sensitivity on average, (b) consistency in sensitivity throughout the full field range, (c) comparatively less demanding measurement fidelity, and (d) for simplicity in its experimental realization.

In chapter 4, we have demonstrated decoherence-limited magnetic sensing with single electronic spin qubits in diamond over a field sensing range of $\sim \pm 0.3$ mT. The results should find immediate application in demonstrated nanoscale magnetic sensing and imaging techniques with the electron spin of the NV center[5, 107], and may also open the way for the application of other quantum feedback and control techniques to magnetometry.

In chapter 5, we have reported a quantum sensing method for AC-magnetometry with PEA. Our results show significantly improved dynamic range and linearity of the readout for time-dependent magnetic fields, while preserving the increased sensitivity of DD pulse sequences. Our method also allows for unambiguous reconstruction of the amplitude, phase, and frequency of the oscillating field, and allows us to track the phase in each measurement shot. This may open up the capability to study the spin configuration changes of nanoscale volumes of spins with unprecedented resolution, and also allow for the study of systems where the spins are hard to polarize and drive due to spectral and spatial diffusion.

6.2 FUTURE WORK

Due to room-temperature workability and potential atomic resolution, diamond spin probe technique has become a promising candidate for nanoscale magnetometry. This thesis explored several methods of improvements for magnetometry which will be useful for practical applications. Implementation of these methods on a nanoscale magnetic imaging apparatus is yet to be performed. An example of such an apparatus would be a combination of a confocal microscope and an AFM with a diamond spin probe tip. The diamond spin probe tip could either be fabricated out of diamond[17, 37] or simply formed by attaching a diamond nano-crystal onto an AFM tip[38]. Building the hybrid-SPM in practice could be challenging and will require a careful plan in the design. Special protocols will have to be implemented in order to correct for the probe-to-target drifts[17]. Requirement of long data integration times per pixel could also be an issue when it comes to micrometer length scale image scans[17]. By sacrificing spatial resolution or field sensitivity, it is possible to greatly reduce the total scan time for the magnetic imaging. In Ref.[43] for example, magnetic

imaging with NV ensembles was demonstrated by the use of a diamond chip with an array of NV's along with charged-coupled device (CCD) detection for simultaneous measurements. However, engineering such diamond sensor arrays with precise positioning of NV's can be challenging[25, 26, 27]. Nevertheless, diamond spin based magnetic imaging may open a new tool for fruitful research on nanoscale systems. This includes exploring the spin physics of 2D materials like graphene, novel magnetic nano-particles, single molecule magnets and nanoscale biological systems.

APPENDIX A

GROUP THEORETICAL APPROACH TO NV CENTER

A.1 SYMMETRY GROUP OF THE HAMILTONIAN

Consider the Hamiltonian of a system H, a state vector $|\psi\rangle$, and a linear unitary operator U_j. The expectation of the Hamiltonian could be given as:

$$\langle\psi|H|\psi\rangle = \langle\psi^T|H^T|\psi^T\rangle \tag{A.1}$$

where, $H^T = U_j H U_j^{-1}$ and $|\psi^T\rangle = U_j|\psi\rangle$ defines the active transformation of the system under the operation of U_j. If H^T is the same as H (i.e., $H = U_j H U_j^{-1}$), U_j is said to leave H invariant. Moreover, any operator which leaves H invariant commutes with H. The set of all operators which leave the Hamiltonian invariant form a group known as the group of the Schrödinger equation (G_S) or the symmetry group of the Hamiltonian. Because of the commuting property, applying any of these operators to a solution of the Schrödinger equation $H|\psi_n\rangle = E_n|\psi_n\rangle$ leads to,

$$U_j H|\psi_n\rangle = E_n U_j|\psi_n\rangle = H(U_j|\psi_n\rangle) = E_n(U_j|\psi_n\rangle) \tag{A.2}$$

This implies that the state under the transformation $U_j|\psi_n\rangle$ must have the same energy E_n as the original state $|\psi_n\rangle$. Moreover, given any energy eigenfunction we could obtain other degenerate eigenfunctions by the application of the symmetry operators which commute with H. If this procedure gives all the degenerate functions $|\psi_n\rangle$ the degeneracy is said to be "normal". In this case, the set of eigenfunctions $|\psi_n\rangle$ form a basis for an irreducible

T_d	E	$8C_3$	$3C_2$	$6\sigma_d$	$6S_4$
A_1	1	1	1	1	1
A_2	1	1	1	-1	-1
E	2	-1	2	0	0
T_1	3	0	-1	-1	1
T_2	3	0	-1	1	-1

C_{3V}		E	$2C_3$	$3\sigma_v$
A_1	$\hat{z}$	1	1	1
A_2		1	1	-1
E	$\{\hat{x}, \hat{y}\}$	2	-1	0

Table 3: Character tables for T_d and C_{3V} symmetry groups

matrix representation (IR) of the symmetry group G_S whose dimension is equal to the given degeneracy[124].

A.2 SYMMETRY OF THE NV CENTER

The diamond lattice structure contains four carbon atoms at the vertices and one in the center of a tetrahedron. Each adjacent carbon atom pair is σ-bonded by the sp^3 orbitals. Therefore, removal of the center carbon atom leaves four sp^3 atomic orbitals (AO) from adjacent atoms to be pointing towards the vacancy. Hence, the electronic system around a vacancy shows T_d symmetry which can form a_1 and t_2 molecular orbitals (MO) with A_1 and T_2 symmetry respectively. Replacing an adjacent carbon by a nitrogen atom breaks down the T_d into C_{3V} symmetry. Hence, the electronic states of the NV center are determined by how they transform under C_{3V} group operations. When the symmetry is reduced from $T_d \rightarrow C_{3V}$, the t_2 orbital as well reduces to: $t_2 \rightarrow a_1 + e$. Since the NV system we are interested in contains altogether six electrons, it is equally valid to regard this as a system with two holes and makes the analysis much simpler. By charge overlap consideration it is known that the e electronic orbital occupies more energy than the a_1 electronic orbital and vice versa for the hole. Therefore, for the two hole system the ordering of the energy

lies as follows: $e^2 < ea_1 < a_1^2$. The spin-orbit wave functions of hole-e^2 can take the form $^3A_2$, $^1A_1$ or ^1E while hole-ea_1 can take either ^3E or ^1E. Here, the superscript refers to the spin state $(2S+1)$ whereas the rest of the symbols are borrowed from standard group theoretical notations. One could further work out the ordering of e^2 hole states by analyzing the Coulomb interaction; and the result turns out to be $^3A_2 <^1 E <^1 A_1$[125]. Optical transition is associated with triplets and therefore, the excited state is attributed to the ^3E state.

A direct approach of obtaining the MOs from the AOs is to use 'projector operators' constituted by IRs of C_{3V} group[124]. This essentially gives a basis transformation from $\{n, c_1, c_2, c_3\}$ to $\{a_1^N, a_1^C, e_x, e_y\}$:

$$\begin{aligned} a_1^N &= n \\ a_1^C &= c_1 + c_2 + c_3 \\ e_x &= 2c_1 - c_2 - c_3 \\ e_y &= c_2 - c_3 \end{aligned} \tag{A.3}$$

where, n and c_i are sp^3 AOs of nitrogen and carbon atoms respectively. Due to the Coulomb interaction between electrons, a_1^N and a_1^C get further mixed, leading to a new basis of MOs: $\{a_1', a_1, e_x, e_y\}$. Furthermore, because the a_1' MO is always fully occupied and its energy lies in the diamond valence band[70], it is sufficient to consider only the a_1 and e orbitals to describe the overall energy levels of NV. For instance, the electronic configuration of the ground state ($^3A_2$) and the first excited state (^3E) can be recognized as $a_1^2e^2$ and $a_1^1e^3$ respectively (Figure 32b). The explicit form of the wavefunctions are summarized in Table 4.

We may also include the effect of spin-orbit and spin-spin coupling which makes the total Hamiltonian $H = V + V_{so} + V_{ss}$ where $V_{so} = \lambda L_z S_z + \lambda'(L_x S_x + L_y S_y)$ and $V_{ss} = \rho S_z^2 + \rho'(S_x^2 + S_y^2)$. Clearly, V_{so} and V_{ss} do not affect the spin singlets. The ground state spin triplet $^3A_2$ is unaffected by V_{so}; however, it is affected by V_{ss}, causing further reduction to a doublet $\{|A_2, S_x\rangle, |A_2, S_y\rangle\}$ with symmetry E and a singlet $|A_2, S_z\rangle$ with symmetry A_1[69].

In the presence of a strong strain field Δ perpendicular to the symmetry axis, such as laser excitation, the excited state ^3E will divide into two states E_x and E_y. Then each E_i $(i = x, y)$

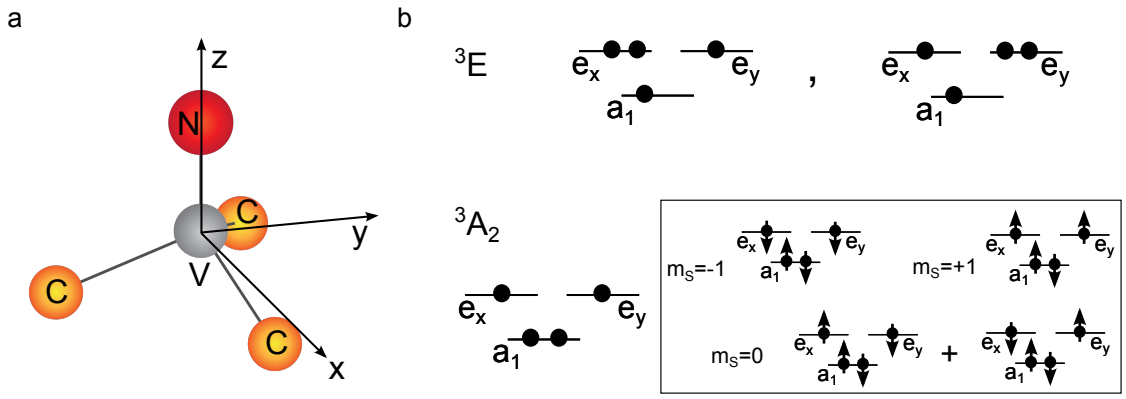

Figure 32: **a,** Schematic of the NV center showing C_{3V} symmetry. The geometry is used to derive the MOs. NV symmetry axis is chosen to be along $\hat{z}$, and one of the carbon atoms lies in the xz-plane. **b,** Schematic for six electron configuration of ground state ($^3A_2$) and excited state (^3E). The two electrons in a_1' MO is not shown in the figure. The inset box gives the different spin configurations in $^3A_2$. Note that the ground state, $^3A_2$, is an orbital singlet but a spin triplet.

will further reduce due to V_{so} into a doublet $\{|E_i, S_x\rangle, |E_i, S_y\rangle\}$ with symmetry E and a singlet $|E_i, S_z\rangle$ with symmetry A_1. Here, we assume $\Delta >> V_{so} >> V_{ss}$. This leads to the presently accepted energy level structure for the NV system particularly at low temperature[69, 73, 125, 70]. The energy level structure at room temperature, however, is different in the ^3E excited state and is accounted for by phonon mediated orbital averaging[126].

A.3 OPTICAL SELECTION RULES

It is the electric dipole interaction that governs the optical cyclic transitions between NV electronic levels. Therefore, the selection rules can be determined by simply finding the non-zero matrix elements:

$$\langle \psi_f | \vec{d}.\vec{E} | \psi_i \rangle \neq 0 \tag{A.4}$$

where ψ_i and ψ_f are the initial and the final electronic wavefunctions respectively. Because $\vec{d}.\vec{E}$ must change one of the single-electron orbitals in order for the dipole moment to exist, ψ_i and ψ_f must belong to different electronic configurations. Another important selection

Config.	C_{3V} term	Spin, S	m_s	Wavefunction
$a_1^2e^2$	$^3A_2$	1	0	$\|111001\rangle + \|110110\rangle$
			-1	$\|110101\rangle$
			+1	$\|111010\rangle$
	^1E	0	0	$\|111100\rangle - \|110011\rangle$
				$\|110110\rangle - \|111001\rangle$
	$^1A_1$	0	0	$\|111100\rangle + \|110011\rangle$
$a_1^1e^3$	^3E	1	0	$\|100111\rangle + \|011011\rangle$
			-1	$\|010111\rangle$
			+1	$\|101011\rangle$
			0	$\|101101\rangle + \|011110\rangle$
			-1	$\|011101\rangle$
			+1	$\|101110\rangle$
	^1E	0	0	$\|100111\rangle - \|011011\rangle$
				$\|101101\rangle - \|011110\rangle$

Table 4: The ground state ($a_1^2e^2$) and excited state ($a_1^1e^3$) electronic states. In the wavefunctions, "0" ("1") denote non-occupation (occupation) of an electron in orbital-spin states in the order of $|a_1\bar{a_1}e_x\bar{e_x}e_y\bar{e_y}\rangle$, where bars (no bars) refer to spin down (up) with respect to NV symmetry axis.

rule is that electronic spin S and its axial projection m_s must be conserved, provided that the spin-orbit coupling is negligible. This holds true for most operating conditions in which either phonon-induced orbital averaging in the ^3E excited state or strain shifts due to local environment overwhelm the spin-orbit coupling[127, 128].

Group theory can be used to identify the rest of the non-zero matrix elements in Eq. A.4. For instance, suppose $\vec{d}.\vec{E}$, ψ_i, and ψ_f transform under C_{3V} irreducible P, Q and R respectively. Then the Eq. A.4 will be satisfied only if the tensor product $P \otimes Q \otimes R$ includes the

symmetric representation A_1. This can be realized intuitively, because the integration over all space of an odd function inner product leads to zero net contribution. For C_{3V} symmetry, the position operator $\hat{z}$ (Along NV symmetry axis) transforms as A_1 and $\{\hat{x}, \hat{y}\}$ transform as E[129, 130].

APPENDIX B

CALIBRATION AND TEST SCHEMES

B.1 CONFOCAL SETUP

The principle of the confocal system is to collect light originated within a infinitesimal volume in the sample around the focus of the green excitation laser. In order to ensure this, we perform the following strategy. First we introduce 650 nm red laser light from the collection fiber and align this beam with of the excitation beam. Red laser is specifically chosen for this purpose, because its wavelength is within the NV spectrum. When the red beam meets the green beam after passing the dichroic beam splitter, they both are made to go coincidently and this guarantees that the both beams get focused at the same azimuthal axis. Also, both beams are made to be collimated just before the objective. This will ensure the depth of focus is the same, provided that the objective is 'apochromatic'. These tricks constitute the coarse adjustments for the alignment, and are usually sufficient to get an initial image out of the confocal system. Other tests and calibrations are explained below. In the final stage of alignment, we remove the red laser from the system and instead hook up the other end of collection fiber to the photon counter. Final alignment is performed by confocal imaging the diamond sample itself. Fine tuning of the lens mounts is made until the photon counts is maximized while in focus at a bright spot in the image. Finally, confocal imaging of a commercial resolution target (EDMUND OPTICS NT59-206) is performed for the calibration of image length scales (Figure 33).

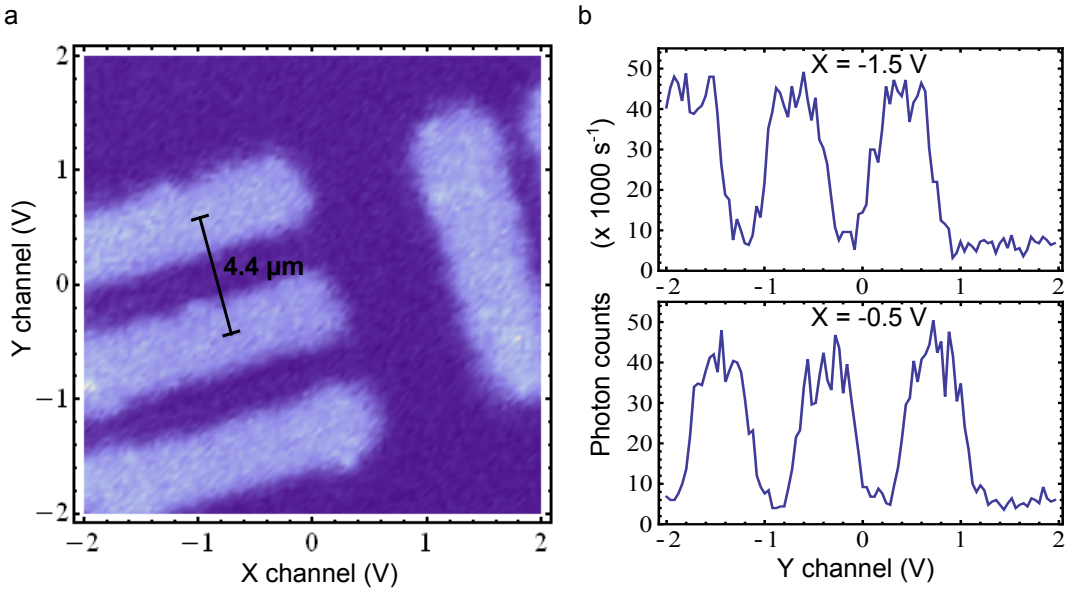

Figure 33: **a,** Confocal image of a EDMUND OPTICS NT59-206 resolution target. The line separation in 'element 6 of group 7' is 4.4 μm. The scale factor for confocal images then turns out to be 4.2 μm/V. **b,** 'Line-cuts' of the above image at X=-1.5V (top) and X=-0.5V (bottom).

B.1.1 Imaging conditions for the confocal

In order to be possible to generate a 2D image, it is necessary to ensure that light passes through the objective at all operating angles caused by the galvanometer scanner mirrors. This demands the imaging condition between the scanner mirrors and the objective to be satisfied; i.e, the galvanometer mirrors have to be imaged at the back aperture of the objective (Figure 34). Meanwhile, it is also necessary to protect the collimation of the light entering the objective. Because these conditions should be satisfied for a wide range of wavelengths, we only use optical lenses known as 'achromatic-doublets' that are corrected for chromatic aberration for the relevant wavelength range. A useful test is to use a mirror at the focus of the objective to reflect back the excitation light. Now, scanning of the galvanometer mirrors should not move the reflected light when it reaches the collection fiber, in order to make sure the fiber coupling of back reflected light is still maintained. This could be checked by introducing a pellicle beam splitter near the collection fiber. A movement of the reflected

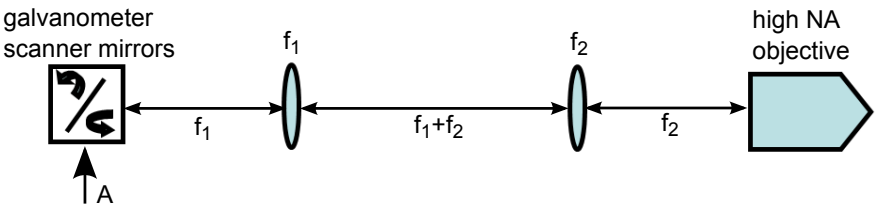

Figure 34: By satisfying the condition for imaging the scanner mirrors on back of the objective, it is ensured that all light at A enters the objective. Also, since the lenses form a telescope system, a collimated beam at A will still be collimated when it enters the objective. To avoid achromatic aberration, we use an 'apocromatic' objective and lenses.

light spot can occur if the galvanometer mirrors are not imaged exactly at the principle plane of the objective.

Another consideration for imaging is, ensuring that all the light accepted from the diffraction limited volume in the sample (by the sample objective) is delivered to the collection fiber. We have a second objective near the collection fiber to focus the light from the sample into the fiber core. Starting from the sample objective we can use the ray matrix formalism (ABCD matrix analysis) to obtain the final focusing angle (after passing all the optical elements in the way), which has to be compatible with the numerical aperture of the collection fiber.

B.1.2 Waist size of the laser beam

As described in section 2.2, the optimal size for the excitation laser beam is when its waist matches the aperture size of the objective[76]. In order to accurately measure the waist of a collimated Gaussian beam, we perform a simple test as shown in figure 35a. Here, we have razor blade fixed to a stage to have control on the amount of blockade of the laser beam. The total power of the unblocked fraction of the beam is measured with a photo detector (light power meter). Figure 35b shows the profile of measured power as we move the stage.

An accurate calculation of the total transmitted light energy can be made by considering the two-dimensional integral:

$$P(x) = P_{Tot} - I_0 \int_{-\infty}^{x} e^{-2x^2/w^2} dx \int_{-\infty}^{+\infty} e^{-2y^2/w^2} dy \tag{B.1}$$

where P_{Tot}, I_0 and w are the total power, peak intensity and waist of the Gaussian beam. The above integral can be simplified to:

$$P(x) = \frac{P_{Tot}}{2}\left[1 - erf\left(\frac{\sqrt{2}x}{w}\right)\right] \tag{B.2}$$

Hence, fitting the data in figure 35b to equation B.2 allows to extract the waist size of the beam accurately. A short-cut method of finding the waist would be to get the two coordinates that correspond to 90% (x_{90}) and 10% (x_{10}) power transmissions. By using equation B.2, it can be shown that the waist is approximately given by $w \approx (x_{90} - x_{10})/1.28$.

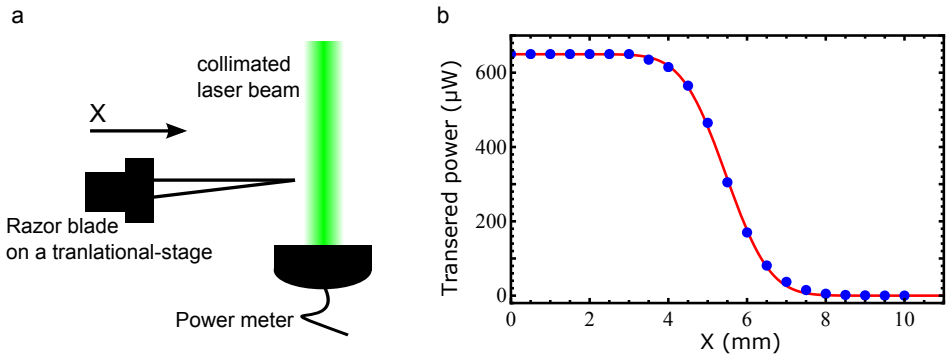

Figure 35: **a,** Schematic of knife-edge test for estimating the waist size of 532 nm laser. **b,** Power transfer at different position of the razor-blade beam block. Red solid line is a the best fit for a fit function as in equation B.2. The waist size from the fit function is $w \approx 1.76$ mm.

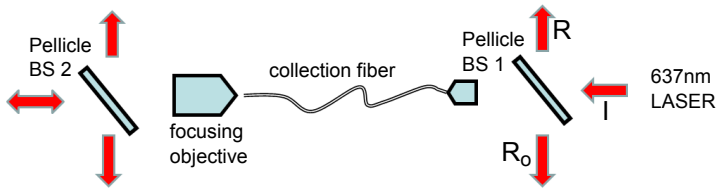

Figure 36: The procedure for the measurement of the confocal coupling efficiency

B.1.3 Coupling efficiency of the confocal

Coupling efficiency of the confocal can be estimated by introducing pellicle beam splitters near both ends of the collection fibre. This measurement is performed while red laser light is introduced to the collection fiber in the initial alignment stage. It is important to use pellicle beam splitters rather than regular beam splitters in order to avoid any deflection of the original light path.

Figure 36 shows the schematic for such a test. For instance, power measurements of original red light I and reflected (from BS-1) portion R allows to estimate the coupled light C_o coming out of the collection fibre: $C_o = R_o I/R$, where R_o is the reflected portion of the coupled light. Similarly, by suitable power measurements around the second beam splitter (BS-2), we can estimate the light input towards the collection fibre C_i from the confocal setup. The coupling efficiency is given by C_o/C_i and is approximately $\sim 90\%$ in our confocal setup.

B.2 EXCITATION LASER SETUP

For pulsed ESR experiments, it is necessary to have the ability to pulse the laser in a controlled fashion. This is achieved by a use of an acoustic-optic modulator (AOM). Figure 37 shows the schematic of the 532 nm excitation laser set-up. When the AOM modulation input

is driven with a RF wave (ON condition), the laser light is subject to a diffraction pattern. The pinhole selects only the first order deflection and therefore in the absence of RF at the modulation input (OFF condition), no light will be passed. The RF is generated by an AOM driver upon a TTL input (not shown in the figure). Neutral density (ND) filters are used for attenuation of the laser intensity. The focal length of the lens to be introduced before the AOM is determined by the equation below.

$$f = \frac{\pi d_i d_o}{4\lambda} \tag{B.3}$$

where λ is the optical wave length, d_i is the input optical beam diameter, and d_o is the waist diameter inside the modulator[131].

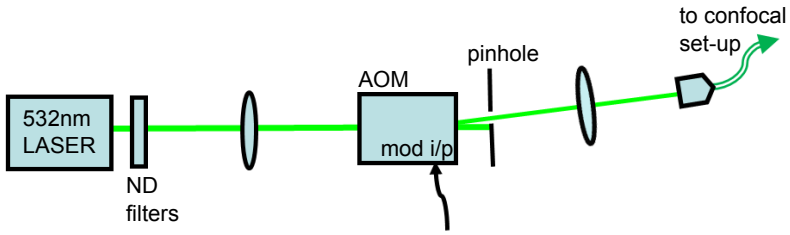

Figure 37: The schematic of excitation laser set-up. ND filters are used for laser attenuation. The pinhole selects out only the first order deflected light when AOM is driven.

B.2.1 Contrast ratio of the excitation laser

An insignificant amount of light can still pass through in the green laser setup even under 'light-off' state. The contrast ratio (CR) characterizes the amount of this leakage.

$$CR = 10\ log\left(\frac{leakage\ light\ power\ when\ AOM\ is\ OFF}{transmitted\ light\ power\ when\ AOM\ is\ ON}\right) \tag{B.4}$$

The leakage light when the AOM is off is usually very weak and cannot be measured with regular light power meters. Therefore, we use the photon counters for this purpose. In order to avoid any instrumental errors as well as complications in unit conversions, we may use the

same photon counter detector to measure the amount of light under ON condition. However, because this light is too high and can damage the photon counters, it is very important to introduce a significant attenuation before performing this measurement. Knowing the amount of attenuation used, we can estimate the contrast ratio, which turns out to be ≈ -54 dB in our confocal laser set-up.

B.2.2 Optimum power for the excitation laser

The optimum operating power for the excitation laser can be determined by a simple test wherein we obtain a florescence signal as a function of the laser excitation power as shown in figure 38. Here, we use the signal which is purely due to NV florescence, i.e., we subtract the photon counter detector reading when focused at the bright spot (due to the single NV) from that of the background (away from the spot). The optimum operating power corresponds to the point when the curve starts to saturate. At this point the NV is operated at its maximum rate of excitation. Increasing the laser power further will only cause an increment in the laser shot noise.

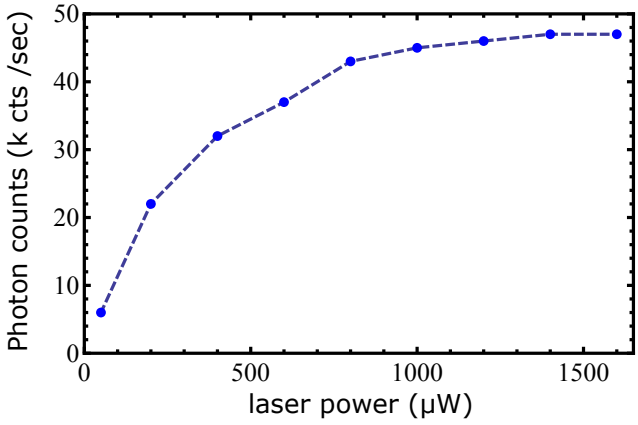

Figure 38: The photon counts due to NV (excluding the background counts) with varying power of the excitation laser.

B.3 CALIBRATION OF DELAY TIMES

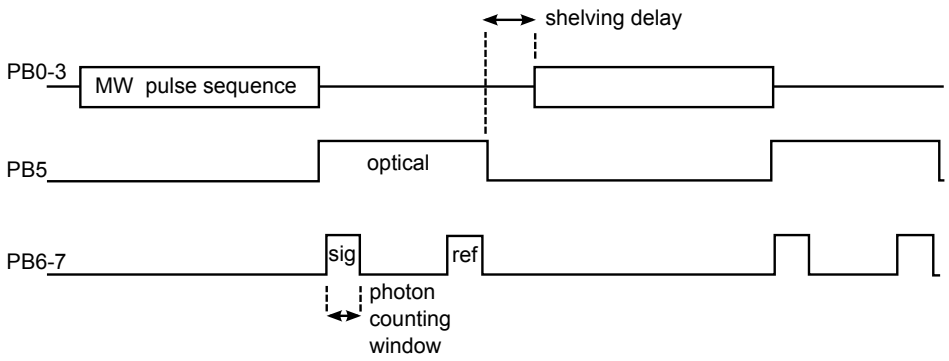

Figure 39: Overall pulse scheme for ESR experiments: Channel 0-3 of the pulse programmer drives the MW switches. Channel 5 drives the AOM. Channel 6(7) drives the 'signal'('reference') counter gates. The typical photon counting window, optical pulse length and shelving delay used in our experiments are 300 ns, 2 μs and 1.5 μs respectively.

Pulsed-ESR experiments require careful synchronization in timings of MW/optical pulses, photon counting windows etc. Therefore, it is necessary to measure the delay/response times in all signal sources and transmission lines. The response time of the AOM including the cable delays can be obtained from the data in figure 40 where the x-axis indicates the time with respect to the generation of TTL pulse given to the AOM driver. For instance, the pulsing of green laser here is observed after ~ 1 μs since the AOM is driven. In other words, in order to have a laser pulse at a certain time, it would be necessary to initiate the TTL drive to the AOM ~ 1 μs earlier. A pulse programmer (SpinCore PulseBlasterESR-Pro) generates all the necessary TTL pulses and controls the overall experimental timing sequence.

The MW pulsing is achieved by controlling the MW switches with TTL pulses. The delay between the time of TTL pulse and when the sample sees the MW primarily depends on the cable length. We can monitor this delay simply by use of an oscilloscope (Agilent MSO7104A). However, since the MW frequencies are typically beyond the bandwidth of oscilloscopes, we use a converter element known as an RF-detector (Narda 4503A-03 0.01-18 GHz) to convert the MW into a DC voltage.

Another critical timing element in our experiments is the generation of AC magnetic

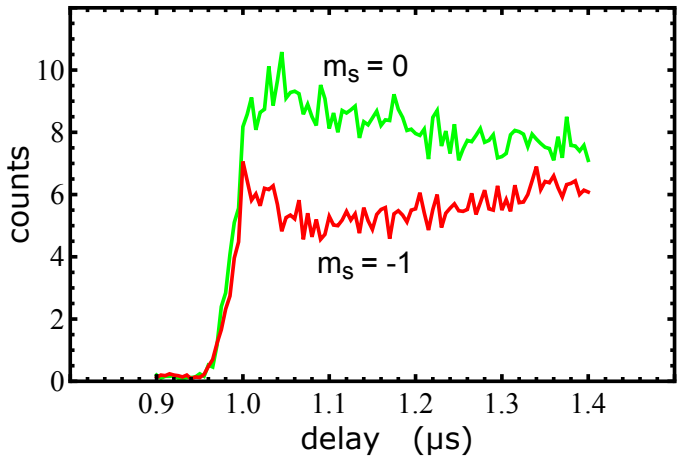

Figure 40: Photon counts profile for $m_S = 0$ and $m_S = -1$ levels. X-axis gives the time delay between TTL signals for photon counter and AOM driver.

field. The AC magnetic field is produced by a signal generator (Agilent 33250A), and is externally triggered with a TTL pulse. The time delay between the TTL trigger pulse and Agilent signal output also depends on the signal frequency an is approximately 5 μs for a frequency of 21 kHz.

Other timing issues include the length of the window for photon counting, length of optical excitation pulse, and the time in between consecutive ESR pulse schemes known as the 'shelving delay'. Data in Figure 40 also allows estimation of the optimum counting window width. We use a 300 ns counting window in our experiments. A narrower window gives a low value for the integrated counts while an overly wider window lowers the SNR. The optical excitation pulse length is determined such that NV completely polarizes to the steady state. This is confirmed by ensuring the same average photon counts in the 'reference' window for both initial spin states. The typical optical pulse length in our experiment is 2 μs. It is not useful to have a longer excitation pulse, because it only increases the measurement time of the experiment.

At the end of optical excitation, the NV is in a steady state between $m_s = 0$ and the metastable states. The use of 'shelving delay' is to give sufficient time for the steady state NV to relax completely into the ground state. The shelving delay in our experiments is

typically set to 1.5 μs.

B.4 CALIBRATION OF π-PULSES

The characterizing π-pulse length is normally achieved by a Rabi experiment. For instance, data in Figure 7 of Chapter 2 implies a π-pulse of ≈ 50 ns. One of the technical limitations in our pulse programmer (2.5 ns of pulse resolution) limits pulses that can be generated only to 47.5, 50, 52.5 ns etc but not in between[132]. The limited pulse resolution can result in a pulse error. In a 40 ns expected π-pulse for instance, there could be a $2.5/40 \approx 6\%$ of a pulse error. The test scheme below allows to achieve highly accurate MW pulses.

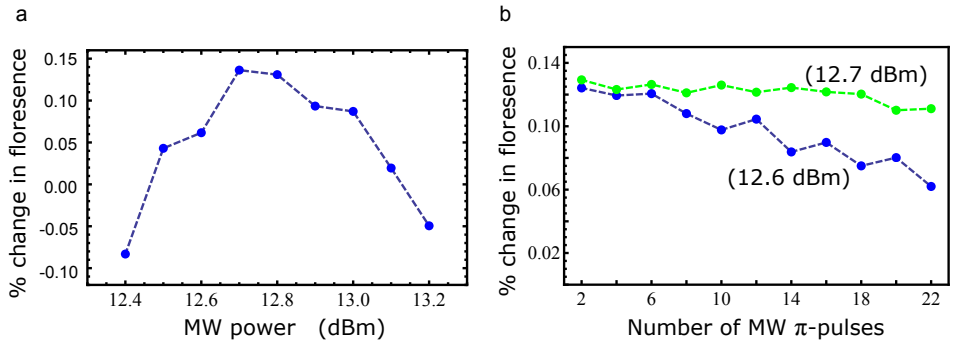

Figure 41: **a,** Signal after 20 consecutive MW π-pulses is plotted for MW power slightly varied about the operating point. The length of π-pulse here is 40 ns. The most accurate pulses are achieved here for MW power of 12.7 dBm. **b,** The signal after applying an even number of π-pulses. A slightly inaccurate power ($\sim$ 0.1 dBm) can lead to a significant difference when many pulses are involved.

We apply an even number (20) of π-pulse and plot the signal while varying the MW power slightly around the working point (Figure 41). The power that corresponds to the maximum signal gives the most accurate pulses. The pulse error here can be estimated by noting that $t_\pi \propto 1/P^2$ where P is the MW power given. The power resolution in the MW synthesizer is 0.1 dBm. This correspond to a $\sim 2\%$ change in power and consequently $\sim 1\%$ change in t_π. Therefore, the maximum pulse error can be brought down to $\sim 1\%$ by this approach.

APPENDIX C

SUPPORTING MATERIAL FOR CHAPTER 3

C.1 DERIVATION OF PHASE VARIANCE IN THE RAMSEY EXPERIMENT

We begin with the initial state $\rho_0 = |0\rangle\langle 0| = (I + \sigma_x)/2$. The time evolution of this state leads to

$$\begin{aligned}\rho_1 &= U\rho_0 U^\dagger \\ &= (I + U\rho_0 U^\dagger)/2 \\ &= (I + \sigma_x \cos(\phi) - \sigma_y \sin(\phi))/2\end{aligned}$$

where, $U = \exp(-i\phi\sigma_z)$, and σ_i are Pauli matrices. To be more precise, we may also introduce the decay factor D, in order to take the decoherence into effect.

$$\rho_1 = (I + D\sigma_x \cos(\phi) - D\sigma_y \sin(\phi))/2$$

Action of the second $(\pi/2)_y$ pulse brings the state to

$$\begin{aligned}\rho_f &= R_y(\pi/2)\rho_1 R_y(\pi/2)^\dagger \\ &= (I + D\sigma_z \cos(\phi) - D\sigma_y \sin(\phi))/2\end{aligned}$$

The measurement signal of this state is given by $S = Tr[M\rho_f]$, where $M = a|0\rangle\langle 0| + b|1\rangle\langle 1|$ is the optical measurement operator and $a(b)$ is a Poisson random variable with mean α_0 (α_1) that represents our experimental counts per optical measurement when the qubit is in the $|0\rangle$ ($|1\rangle$) state.

Also note that $Tr[M] = a+b$, $Tr[M\sigma_z] = a-b$, and $Tr[M\sigma_y] = 0$. Therefore the average signal per optical measurement is given by,

$$\langle S\rangle = \frac{1}{2}[(\alpha_0 + \alpha_1) + D(\alpha_0 - \alpha_1)\cos(\phi)] \tag{C.1}$$

In order to find the variance of the signal, we first note that $M^2 = a^2|0\rangle\langle 0| + b^2|1\rangle\langle 1|$. Moreover due to Poisson statistics, we have $\langle a^2\rangle = \alpha_0^2 + \alpha_0$ and $\langle b^2\rangle = \alpha_1^2 + \alpha_1$. This leads to

$$\langle S^2\rangle = \frac{1}{2}[(\alpha_0^2 + \alpha_0 + \alpha_1^2 + \alpha_1) + D(\alpha_0^2 + \alpha_0 - \alpha_1^2 - \alpha_1)\cos(\phi)] \tag{C.2}$$

From Eq. C.1 and C.2 we get for the variance of the signal

$$\begin{aligned}(\delta S)^2 &= \langle S^2\rangle - \langle S\rangle^2 \\ &= \frac{1}{4}\{(\alpha_0 - \alpha_1)^2 + 2(\alpha_0 + \alpha_1)\} + \frac{D}{2}(\alpha_0 - \alpha_1)\cos(\phi) - \frac{D^2}{4}(\alpha_0 - \alpha_1)^2\cos^2(\phi)\end{aligned}$$

Differentiating Eq. C.1 with respect to ϕ we get,

$$\frac{d\langle S\rangle}{d\phi} = \frac{D(\alpha_0 - \alpha_1)\sin(\phi)}{2} \tag{C.3}$$

The phase variance can now be obtained as,

$$\begin{aligned}(\delta\phi)^2 &= (\delta S)^2/|\frac{d\langle S\rangle}{d\phi}|^2 \\ &= \frac{1}{D^2\sin^2(\phi)}\Big[1 + 2\frac{\alpha_0 + \alpha_1}{(\alpha_0 - \alpha_1)^2} + \frac{2D\cos(\phi)}{\alpha_0 - \alpha_1} - D^2\cos^2(\phi)\Big]\end{aligned}$$

The expression inside the square brackets above, is in fact the κ_{th} defined in Chapter 3.

C.2 MATHEMATICA CODES FOR THE SIMULATIONS

Definitions

```
one := {0, 1};                    (* 1 state *)
zero := {1, 0};                   (* 0 state *)
Dagger[A_] := Conjugate[Transpose[A]];

(* Decoherence *)
DecayEnvilope[t_, T2_] := Exp[-( t/ T2)^2  ]; (* Decoherence *)
Decohere[{{a_, b_}, {c_, d_}}, t_,  T2_] :=
          {{a, b*DecayEnvilope[t, T2]}, {c*DecayEnvilope[t, T2], d}};

(* Rotation operators *)
Ry[Theta_] := {{Cos[Theta/2], -Sin[Theta/2]}, {Sin[Theta/2], Cos[Theta/2]}};
Rx[Theta_] := {{Cos[Theta/2], -I*Sin[Theta/2]}, {-I*Sin[Theta/2], Cos[Theta/2]}};
Rz[Theta_] := {{1, 0}, {0, Exp[I*Theta}};
U[phi_] := {{1, 0}, {0, Exp[-(I*phi)]}};

(* Measurement operators *)
M0[xx_, yy_] := {{xx, 0}, {0, yy}};
M1[xx_, yy_] := {{1 - xx, 0}, {0, 1 - yy}};
```

Simulation of Ramsey

```
(*Initialization*)
alpha = 0.010;   beta = 0.007;  (* average photons per optical measurement *)
T2star = 1200;                  (* ns *)
Samples = 20000;
NumOfTrials = 50;
TempDataPoints = Array[0 &,  NumOfTrials];
TimePoints = Table[kk, {kk, 5, 2000, 5}];           (* ns *)
DataPoints = Array[{0, 0} &, Length[TimePoints]];
gB = 2 Pi*(0.003);           (* 2Pi times detuning in GHz *)

For[dd = 1, dd < Length[TimePoints] + 1, dd++, {

    v = Rx[Pi/2].zero;
    rhostart = KroneckerProduct[v, Conjugate[v]];
    Ud = U[gB*TimePoints [[dd]]];
    rhostart = Ud.rhostart.Dagger[Ud];
    rhostart = Decohere[rhostart, TimePoints [[dd]], T2star];

    For[rr = 1, rr < NumOfTrials + 1, rr++, {
       rho = rhostart;
       RandomChooseAlpha =
```

```
        RandomReal[
         NormalDistribution[alpha*Samples, Sqrt[alpha*Samples]]];

       RandomChooseBeeta =
        RandomReal[
         NormalDistribution[beta* Samples, Sqrt[beta* Samples]]];

       ImpMeasurement = M0[RandomChooseAlpha, RandomChooseBeeta];
       rho = Rx[Pi/2].rho.Dagger[Rx[Pi/2]];
       photoncounts = Abs[Tr[ImpMeasurement.rho]];
       TempDataPoints[[rr]] = photoncounts;
       };
     ];
    DataPoints[[dd]] = {TimePoints [[dd]], Mean[TempDataPoints]}
    };
  ];

  ListPlot[DataPoints]
```

Generation of NAPEA data

```
(*Initialization*)
MK = 8; mu = 8; K = 7;
phi = Pi/9.789;
NumOfTrials = 100;  (* number of files *)
T2star = 1200;   (*ns*)
tmin = 20;         (*ns*)
Samples = 2000;                (* Samples *)
(* threshold for determining the bit *)
threshold = (alhpa+beta)*Samples/2 ;

Un = U[phi];
SeedRandom[1982];
For[tt = 1, tt < NumOfTrials + 1, tt++, {
    v = Rx[Pi/2].zero;
    rhostart = KroneckerProduct[v, Conjugate[v]];
    PhiIndex = 0; count = 0;
    entries = Sum[MK + (K - i)*mu, {i, 1, K}];
    Data = Array[{0, 0, 0} &, entries];
    entryIndex = 1;
    For[k = K, k > 0, k-- , {
      runs = MK + (K - k)*mu;
     (* deltaPhi = Pi/runs; Phi = 0; *)    (* Need only for VAR *)
      For[r = 0, r < runs, r++, {
        rho = rhostart;
        For[j = 0, j < 2^(k - 1), j++, rho = Un.rho.Dagger[Un];];
        rho = Decohere[rho, (2^(k - 1)) *tmin, T2star];
```

```
        rho = Rz[PhiIndex*Pi/2].rho.Dagger[Rz[PhiIndex*Pi/2]];
         RandomChooseAlpha =
         RandomReal[
          NormalDistribution[alpha*Samples, Sqrt[alpha*Samples]]];

        RandomChooseBeeta =
         RandomReal[
          NormalDistribution[beta* Samples, Sqrt[beta* Samples]]];

        ImpMeasurement = M0[RandomChooseAlpha, RandomChooseBeeta];
         rhotemp = Rx[Pi/2].rhotemp.Dagger[Rx[Pi/2]];
        photoncounts = Abs[Tr[ ImpMeasurement. rhotemp]];
        Um = If[photoncounts > threshold, 1, 0];
        Data[[entryIndex++]] = {k, PhiIndex, Um };
        PhiIndex = Mod[++PhiIndex, 4];          (* QUAD *)
        (* PhiIndex = N[Mod[++count, 8]/2]; *)  (* OCT *)
        (* PhiIndex = Mod[++PhiIndex, 2]; *)    (* DUAL *)
        (* Phi = Phi + deltaPhi; *)             (* VAR *)
        }
       ];
      }
     ];
    Export["NAPEA-blah-blah.txt", Data, "Table"];
    };
  ];
```

Generation of QPEA data

```
Un = U[phi];
SeedRandom[1982];
For[tt = 1, tt < NumOfTrials + 1, tt++, {
    v = Ry[Pi/2].zero;
    rhostart = KroneckerProduct[v, Conjugate[v]];
    entries = Sum[MK + (K - i)*mu, {i, 1, K}];
    Data = Array[{0, 0, 0} &, entries];
    OverallBitData = Array[0 &, K];
    entryIndex = 1;
    For[k = K, k > 0, k-- , {
       rhotemp = rhostart;
       Phi = 0;
       For[n = K, n > k, n--,
        Phi += (OverallBitData[[n]])*Pi*N[Power[2, (k - n)]];];
       For[j = 0, j < 2^(k - 1), j++,
        rhotemp = Un.rhotemp.Dagger[Un];];
       rhotemp = Decohere[rhotemp, (2^(k - 1)) *tmin, T2star];
       rhotemp = Rz[Phi].rhotemp.Dagger[Rz[Phi]];
       runs = MK + (K - k)*mu;
       TempBitData = Array[0 &, runs];
```

```
      For[r = 0, r < runs, r++, {
         rho = rhotemp;

         RandomChooseAlpha =
          RandomReal[
           NormalDistribution[alpha*Samples, Sqrt[alpha*Samples]]];


         RandomChooseBeeta =
          RandomReal[
           NormalDistribution[beta* Samples, Sqrt[beta* Samples]]];

         ImpMeasurement = M0[RandomChooseAlpha, RandomChooseBeeta];
         rho = Ry[Pi/2].rho.Dagger[Ry[Pi/2]];
         photoncounts = Abs[Tr[ ImpMeasurement. rho]];
         Um = If[photoncounts > threshold, 1, 0];
         Data[[entryIndex++]] = {k, Phi*2./Pi, Um };
         TempBitData[[r + 1]] = Um;
         };
        ];
       overallbit =
        If[Total[TempBitData] > Length[TempBitData]/2., 1, 0];
       OverallBitData[[k]] = overallbit;
       };
     ];
    Export["QPEA-blah-blah.txt", Data, "Table"];
    };
  ];
```

Analysis routines for PEA data

```
tmin = 20*^-9; t2star = 1.2*^-6; contrast = 1;

(* Phase probability function for a given measurement *)

probphicondm[ph_, um_, contrast_, t_, T2star_, bitindex_, phi0_] :=
 Block[{$MinPrecision = 15, prec = 20},
  Module[{c, tau, phi, t2star, PHI},
   c = SetPrecision[contrast, prec];
   tau = SetPrecision[t, prec];
   t2star = SetPrecision[T2star, prec];
   phi = SetPrecision[ph, prec];
   PHI = SetPrecision[phi0, prec];
   1/2 + 1/2*c*Exp[-(2^(bitindex - 1)*tau/t2star)^2]*(1 - 2*Sign[um])*
     Cos[2^(bitindex - 1)*(phi) - PHI]
   ]
  ]
```

```
(* Coarse search for MLE *)

findTempMLE[trial_, res_, zoom_, guess_, K_] := (
   Module[{trialNumber, PhaseResolution, ZoomRange, GuessMLE,
     xAxisPhase, arrayForPlot, NumberOfBits},
     trialNumber = trial;
     PhaseResolution = res;
     ZoomRange = zoom;
     GuessMLE = guess;
     ResultData = Import[ResultFileNames[[trialNumber]], "Table"];
     xAxisPhase =
      Table[N[kk], {kk, GuessMLE - Pi/(ZoomRange),
        GuessMLE + Pi/(ZoomRange), 2 Pi/PhaseResolution}];
     arrayForPlot = Array[{0, 1} &, Length[xAxisPhase]];
     Table[
      arrayForPlot[[kk, 1]] = xAxisPhase[[kk]], {kk, 1,
       Length[xAxisPhase]}];
     entries = Length[ResultData];
     For[ee = 1, ee < entries + 1, ee++, {
        For[jj = 0, jj < Length[xAxisPhase], jj++, {
           arrayForPlot[[jj + 1, 2]] = arrayForPlot[[jj + 1, 2]]*
              probphicondm[xAxisPhase[[jj + 1]], ResultData[[ee, 3]],
               contrast, tmin, t2star,
                ResultData[[ee, 1]], ResultData[[ee, 2]]*Pi/2];
           }
          ];
        };
      ];
      MLE =
      xAxisPhase[[Flatten[Position[Table[arrayForPlot[[kk, 2]],
       {kk, 1, Length[arrayForPlot]}],
          Max[Table[arrayForPlot[[kk, 2]],
           {kk, 1, Length[arrayForPlot]}]]][[1]]] ];
      Return[MLE];
     ];
   );

(* Fine search for MLE *)

findFineMLE[file_, guess_, K_] := (
   Module[{fileNumber, tolerance, guessMLE, tempMLE, resTemp,
      zoomTemp},
     tolerance = 0.0000000000000001;
     guessMLE = guess;
     fileNumber = file;
     For[i = 0, i < 22, i++, {
```

```
    (*use this for scaling plot*)
    resTemp = 512*4^i;
    zoomTemp = 4^(i + 0);
    (*use this for detuning scan plot*)
    (* resTemp=1024*4^i;
    zoomTemp=4^(i+2); *)
    (*Print[i+1];*)
    tempMLE = findTempMLE[fileNumber, resTemp, zoomTemp, guessMLE, K];
    If[Abs[guessMLE - tempMLE] < tolerance, Break[];, 1];
    guessMLE = tempMLE;
    };
  ];
 Return[guessMLE];
 ];
);
```

APPENDIX D

SUPPORTING MATERIAL FOR CHAPTER 4

D.1 DETERMINING THRESHOLD FOR STATE DISCRIMINATION

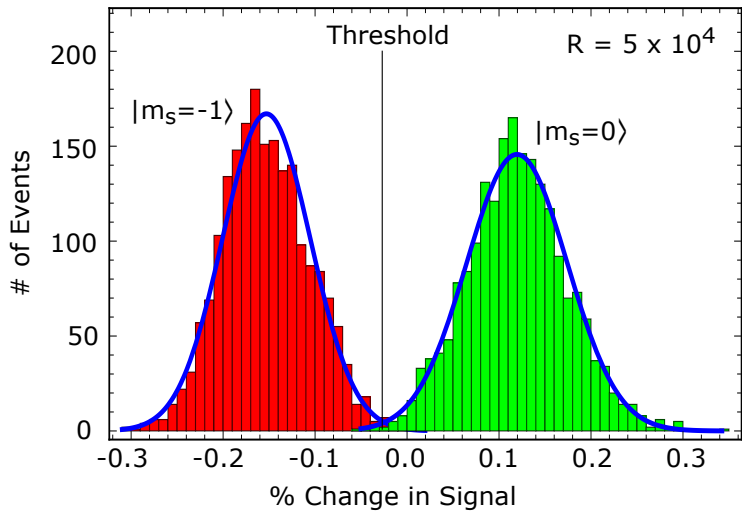

Figure 42: Histograms of percentage change in signal counts for $|m_S = 0\rangle$ and $|m_S = -1\rangle$ states.

In order to achieve high fidelity readout for distinguishing between $|m_S = 0\rangle$ and $|m_S = -1\rangle$ states, we repeated each pulse sequence for R=5 $\times 10^4$ times, which is equivalent to one measurement in our case. The initial green excitation (532 nm) of each pulse sequence polarizes the NV into $|m_s = 0\rangle$ state. Hence by immediately performing the measurement scheme, the percentage change in signal counts is obtained for the $|m_S = 0\rangle$ state. The initialization of

$|m_S = -1\rangle$ is achieved by applying a microwave π pulse followed by the Green excitation.

The histograms are made for the percentage change in signal counts for $|m_S = 0\rangle$ and $|m_S = -1\rangle$ states by performing the measurements repeatedly for 2000 times. In Figure 42 , the blue curves are the Gaussian fits and the black line in the middle shows the "threshold" value which distinguishes between the $|m_S = 0\rangle$ and $|m_S = -1\rangle$ states. The area of the overlapped region as a fraction of total area covered by the individual curves gives the probability of making a false conclusion about the spin state. Therefore subtracting this value from unity gives a measure of the fidelity. For $R = 5 \times 10^4$ as shown in Figure 42 , we achieved fidelity $\approx 99\%$.

D.2 CALCULATING ERRORS FOR RAMSEY

Poisson statistics and the central limit theorem (CLT) are assumed, in analysing the data for the calculation of errors and scaling of the phase (field) variance, in the standard Ramsey technique.

The percentage change in signal after N number of averages (U_N) is defined as,

$$U_N = \frac{S_N - R_N}{R_N} \tag{D.1}$$

where,

$$S_N = \sum_{i=1}^{N} \frac{S_i}{N} \text{ and } R_N = \sum_{i=1}^{N} \frac{R_i}{N}$$

By error propagation theory,

$$(\delta U_N)^2 = \left(\frac{\partial U_N}{\partial S_N}\right)^2 (\delta S_N)^2 + \left(\frac{\partial U_N}{\partial R_N}\right)^2 (\delta R_N)^2 = \frac{1}{R_N^2}\frac{V(S)}{N} + \frac{S_N^2}{R_N^4}\frac{V(R)}{N}$$

where, $V(S)$ and $V(R)$ are variance of S_i and R_i respectively. The CLT is assumed in the last step above. Assuming Poisson statistics for photon counts gives $V(S) = S_N$ and $V(R) = R_N$.

The above noise in U_N can be converted into a noise in the magnetic field detection.

$$\Delta B_{sens} = \left|\frac{(\delta U_N)}{(\gamma e \frac{dU_N}{d\nu})}\right| \tag{D.2}$$

Here, $(\frac{dU_N}{d\nu})$ is simply obtained from the slope of a Ramsey experiment in which the detuning $(\delta\nu)$ is varied, but the free precession time interval (t) is kept constant.

D.3 BOOTSTRAP METHOD FOR ERRORS

The bootstrap method was implemented in order to obtain error bars for the scaling plots in Figure 24. Here, the idea is to repeatedly sample with replacement (re-sample) from the original data sample, and use these re-samples to compute the sampling distribution of the statistic of interest[133]. In NAPEA for instance, we have a sample of 100 ϕ_{MLE} values which was eventually used to calculate the variance of MLE for each case of resource N. The original sample of ϕ_{MLE}'s was then re-sampled 5000 times, each time leading to a unique bootstrap variance of MLE. The standard deviation of these bootstrap variances is used for the errorbars.

D.4 GOODNESS OF FITTING FUNCTIONS

Consider a set of data $\{x_i, y_i \pm \sigma_i\}$ assumed to follow a function $y = f(x; \mu_1, \mu_2 ... \mu_n)$ where μ_i $(i = 1, 2, ..., n)$ are the fitting parameters that need to be evaluated. The least-square approach of obtaining the best fitted curve is to find the set of $\{\mu_i\}$ that minimizes the function,

$$\chi^2 = \sum_{i=1}^{N} \left(\frac{y_i - f(x_i)}{\sigma_i} \right)^2 \tag{D.3}$$

As a measure of the goodness of the fit, we report the reduced Chi-squared value defined as $\chi^2_{red} = \frac{\chi^2}{N-n-1}$ where, N is the number of data points and n is the number of fitting parameters. In all our data, we typically obtain a χ^2_{red} between 0.5-1.2 ensuring the reliability of our statistical approach.

D.5 NUMERICAL ESTIMATION OF THE FINITE PULSE EFFECT

In order to observe the effect of finite pulse width on the Ramsey experiment, we perform a numerical calculation by using 3×3 matrix representation of the Rotation operators. Given a unit vector $\hat{u} = (u_x, u_y, u_z)$, where $u_x^2 + u_y^2 + u_z^2 = 1$, the matrix for a rotation by an angle of α about an axis in the direction of $\hat{u}$ is,

$$R_u(\alpha) = \begin{pmatrix} \cos\alpha + u_x^2(1-\cos\alpha) & u_x u_y(1-\cos\alpha) - u_z \sin\alpha & u_x u_z(1-\cos\alpha) + u_y \sin\alpha \\ u_y u_x(1-\cos\alpha) + u_z \sin\alpha & \cos\alpha + u_y^2(1-\cos\alpha) & u_y u_z(1-\cos\alpha) - u_x \sin\alpha \\ u_z u_x(1-\cos\alpha) - u_y \sin\alpha & u_z u_y(1-\cos\alpha) + u_x \sin\alpha & \cos\alpha + u_z^2(1-\cos\alpha) \end{pmatrix}$$

The qubit rotation about $\hat{x}$-axis in the experiment, is performed with a MW field. If the MW is slightly detuned by δ from the qubit resonance, the effective Rabi frequency becomes $\Omega_{eff} = \sqrt{\Omega^2 + \delta^2} \approx \Omega\left(1 + \frac{\delta^2}{2\Omega^2}\right)$ where, Ω is the on-resonance Rabi frequency. Furthermore, the presence of the detuning corresponds to a magnetic field in the $\hat{z}$ direction. Hence, a $(\pi/2)_x$ pulse in this case, will effectively correspond to a rotation of $\frac{\pi}{2}\left(1 + \frac{\delta^2}{2\Omega^2}\right)$ about a slightly deviated axis $\hat{x'} = (\frac{\Omega}{\sqrt{\Omega^2+\delta^2}}, 0, \frac{\delta}{\sqrt{\Omega^2+\delta^2}})$, and leads to the simplified rotation matrix,

$$R_{x'}(\pi/2) = \begin{pmatrix} \frac{\Omega^2}{\Omega^2+\delta^2}(1 + \frac{\pi\delta^2}{4\Omega^2}) - \frac{\pi\delta^2}{4\Omega^2} & -\frac{\delta}{\sqrt{\Omega^2+\delta^2}} & \frac{\Omega\delta}{\Omega^2+\delta^2}(1 + \frac{\pi\delta^2}{4\Omega^2}) \\ \frac{\delta}{\sqrt{\Omega^2+\delta^2}} & -\frac{\pi\delta^2}{4\Omega^2} & -\frac{\Omega}{\sqrt{\Omega^2+\delta^2}} \\ \frac{\Omega\delta}{\Omega^2+\delta^2}(1 + \frac{\pi\delta^2}{4\Omega^2}) & \frac{\Omega}{\sqrt{\Omega^2+\delta^2}} & \frac{\delta^2}{\Omega^2+\delta^2}(1 + \frac{\pi\delta^2}{4\Omega^2}) - \frac{\pi\delta^2}{4\Omega^2} \end{pmatrix}$$

Free precession for a time t in a Ramsey experiment, is simply a rotation about $\hat{z}$-axis given by the matrix,

$$R_z(t) = \begin{pmatrix} \cos(2\pi\delta t) & -\sin(2\pi\delta t) & 0 \\ \sin(2\pi\delta t) & \cos(2\pi\delta t) & 0 \\ 0 & 0 & 1 \end{pmatrix}$$

The action of a Ramsey sequence $R_{x'}(\pi/2).R_z(t).R_{x'}(\pi/2)$ on an initial vector (0,0,1) is shown in Figure 43. We consider only the z-coordinate of the final vector state which is equivalent to $2P(S_z = 0) - 1$ in the experiment. By fitting the data to a function in the form $\cos\left(2\pi\delta(t + t_{corr}^{th}) + \Phi\right)$ we obtain a $t_{corr}^{th} \approx 25.44$ ns for a Rabi frequency $\Omega = 12.5$ MHz. This is comparable to the value obtained through experiments $t_{corr} \approx 28$ ns. The discrepancy of ~ 2.5 ns in the experimental observation could be arising due to an unaccounted single time resolution step.

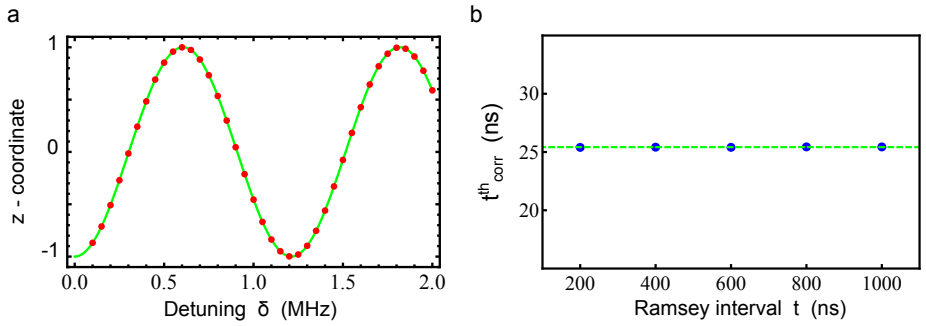

Figure 43: **a,** The z-coordinate after the action of a Ramsey sequence $R_{x'}(\pi/2).R_z(t).R_{x'}(\pi/2)$ on an initial vector (0,0,1). The normalized z-coordinate is equivalent to $2P(S_z = 0) - 1$ in the experiment. Rabi frequency $\Omega = 12.5$ MHz and the precession time $t = 800$ ns. Red dots are the numerical calculations and the green solid line is the best fit for a function $\cos\left(2\pi\delta(t + t^{th}_{corr}) + \Phi\right)$. This leads to a $t^{th}_{corr} \approx 25.44$ ns and is comparable with the observed $t_{corr} \approx 28$ ns in the experiment. **b,** The correction time t^{th}_{corr} remains fairly a constant irrespective of the free precession interval t. Blue dots are the numerical calculations and the green dashed line shows the $t^{th}_{corr} = 25.44$ ns level.

APPENDIX E

SUPPORTING MATERIAL FOR CHAPTER 5

E.1 THE EXPERIMENTAL SETUP

The experimental setup is similar to that of DC magnetometry experiments in Chapter 4. However, a different laser (LASERGLOW IIIB 532nm laser) was used for excitation of NV. A DC bias magnetic field $B_0 \approx 470$ G is applied along the NV axis by a permanent magnet. The AC magnetic field in the experiment is generated by Agilent (33250A) signal generator connected to a solenoid coil (with inductance ≈ 0.3 mH) mounted near the diamond sample. The complete experimental procedure is shown in Figure 44.

E.2 PEA: LIKELIHOOD FOR THE UNKNOWN QUANTUM PHASE

The probability $P(0)$ to be in $|m_s = 0\rangle$ and $P(-1)$ to be in $|m_s = -1\rangle$ is related to the signal due to the in-phase magnetic field $b_I = b_{ac}\cos\theta$ by :

$$S(b_I) = 2P(0) - 1 = 1 - 2P(-1) = D(n\tau)\cos(n\phi_I - \Phi) \tag{E.1}$$

where $\phi_I = 2\gamma_e b_I \tau/\pi$. Thus, given a quantum measurement result u_m the likelihood distribution for the ϕ_I is given by:

$$P(u_m|\phi_I) = \frac{\pm S(b_I) + 1}{2} \tag{E.2}$$

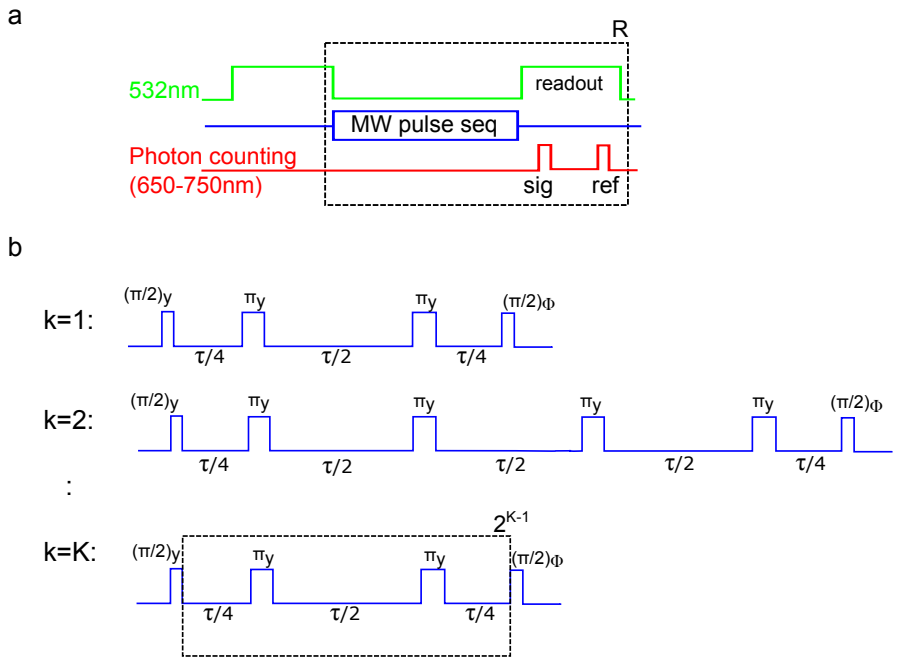

Figure 44: Experimental procedure **a**, General scheme of pulse mode ESR experiments with NV. The initial optical pulse polarizes the NV to $|m_S = 0\rangle$ state while the second optical pulse is for the readout of the spin state. Due to low phonon efficiency, the scheme has to be repeated many (R) number of times. The readout optical pulse is also the spin polarizing pulse for the next measurement. Photon counting takes place at the both ends of the readout optical excitation pulse in-order to minimize the effect of laser fluctuations on our experiments . **b**, The type-I MW pulse sequences used for PEA. For a given k (k=1,2,..K), measurements are performed with different control phases, $\Phi = 0, \pi/2, \pi$ and $3\pi/2$. Experiments in this work were performed with K=4.

where $u_m = \pm$ represents measuring $|m_s = 0\rangle(|m_s = -1\rangle)$ state on the m^{th} measurement. Since our aim is to find the unknown phase ϕ_I given the measurement results, we can use Bayes' theorem, $P(\phi_I|u_m) = P(u_m|\phi_I)P(\phi_I)/P(u_m)$. If the *a priori* distribution of the phase $P(\phi_I)$ is assumed to be flat, then $P(\phi_I|u_{m+1}) \propto P(u_m|\phi_I)$, and we multiply together the probability distributions after each measurement result followed by a normalization step to obtain the conditional probability $P_m(\phi_I)$ after all the measurements. The MLE is found from the likelihood function ($\log P_m(\phi_I)$).

Figure 45a shows the distribution of 1000 measurement results of each state $|m_s = 0\rangle$ and $|m_s = -1\rangle$ when a single pulse sequence is repeated R=15000 times. This leads to a

fidelity $\sim$ 97% in distinguishing the two states. Figure 45b,c shows the phase likelihood distribution for unknown quantum phase ϕ_I for field amplitudes b_{ac} : 44 nT and 264 nT respectively. Here, magnetic field phase $\theta = 0^0$ and frequency f_{ac}=12.55 kHz. Figure 45d show the distributions of MLE's when the experiment is repeated 50 times for the above field amplitudes.

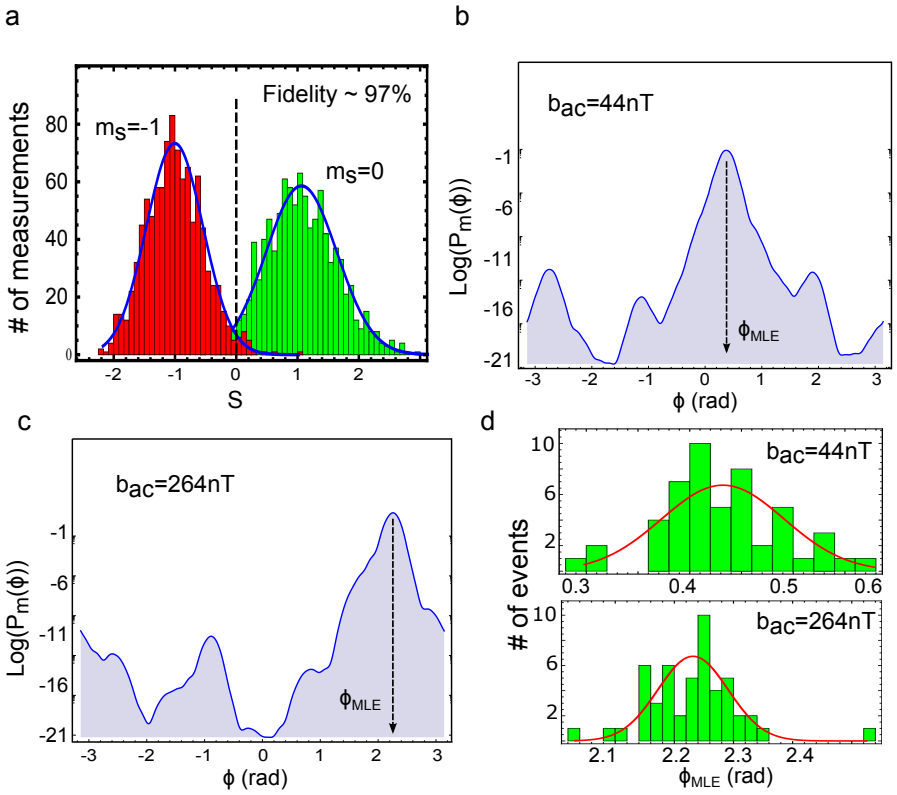

Figure 45: **a**, A repetition of R=15000 times of the pulse sequence in our setup leads to fidelity $\sim$ 97% in distinguishing between the $|m_s = 0\rangle$ and $|m_s = -1\rangle$ states. **b-c**, A trial of the likelihood distribution for the unknown phase is shown for two different magnetic field amplitudes b_{ac} : 44 nT and 264 nT respectively. The magnetic field phase and frequency are $\theta = 0^0$ and $f_{ac} = 12.55$ kHz. The peak of the distribution ϕ_{MLE} gives the maximum likelihood estimate for the unknown phase. **d**, The histograms of ϕ_{MLE}'s when the experiment is repeated many (50) times for the above field amplitudes illustrates the fact that the variance of the experimental results for ϕ_{MLE} is more or less the same for a wide range of field amplitudes. Note that the red solid curves are Gaussian curves parametrized by the experimental results.

E.3 LOCK-IN MAGNETOMETER: DETECTION OF RANDOM PHASE JUMPS OF ANY MAGNITUDE

The PEA parameters set here were $M_K = F = 4$ and leads to a time constant ~ 200 s of the lock-in, and the phase θ was held constant over this time but allowed to vary randomly between measurements. The red curve in Figure 46 shows the history of θ while the blue curve is the estimated phase θ_{est} from the lock-in. The average of the phase jumps from the estimates turned out to be 1.28^0 with a smallest jump of 0.95^0.

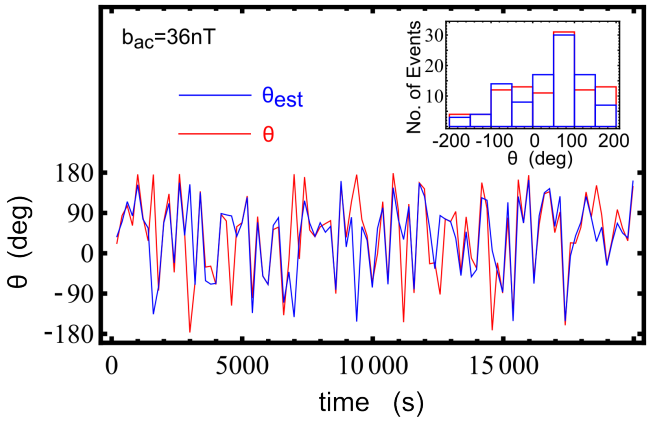

Figure 46: By monitoring both ϕ_I and ϕ_Q channels of our lock-in, we can observe any arbitrarily distributed random phase changes of the magnetic field. The time constant of the lock-in was set to ~ 200 s, and the phase was held constant over this time but allowed to vary randomly between measurements. The inset histogram compares the distribution of the given external phase θ (Red) with the phase estimated θ_{est} from the lock-in (Blue)

E.4 LOCK-IN MAGNETOMETER: TIME CONSTANTS

The relationship between the time constant of our lockin magnetometer and the parameters of the PEA are governed by the equations,

$$T = \sum_{k=1}^{K} M(K,k)\,(2^{(k-1)}\,\tau + t_M)\,R = R\,\tau[M_K(2^K-1)+F(2^K-K-1)]+Rt_M[2M_K+F(K-1)]K/2 \tag{E.3}$$

where, R is the number of times the pulse sequence is repeated and $t_M \sim 2$ μs is the measurement time.

The above equation is plotted in Figure 47a for our experiments as a function of f_{ac} for different choices of K, M_K, F, while keeping the longest pulse sequence length $2^{(K-1)}\tau = 256$ μs a constant. The longest sequence ultimately limits the sensitivity of the quantum sensing, though of course various choices of PEA parameters may result in not attaining this limit. Therefore fixing this value gives us a good way to controllable change the parameters and observe the effect on the dynamic range DR and the minimum detectable field Δb. These have to be obtained through numerical Monte-Carlo simulations, and some results are displayed in Figure 47b,c. As we can see there, above certain threshold measurement fidelity and choices of PEA parameters M_K, F, we obtain close to the decoherence limited sensitivity. By contrast, although CP can attain the decoherence limit, the DR is extremely limited.

A second factor that limits our time constant above is the factor R. As shown in Figure 45a, the number of repetitions of our pulse sequence will govern the fidelity with which we can make the bit measurements $u_m = \pm$. This factor $R = 1.5 \times 10^4$ in our experiments is in turn governed by the photon collection efficiency ξ and visibility V of the fringes in our setup. Recent improvements in these factors, e.g. through photonic nanostructures [33, 37] or resonant excitation [134] can result in decreasing $R \to 1$, while increasing the measurement time $t_M \approx 20$ μs. Correspondingly our time constant can thus be reduced by almost three orders of magnitude. We also note that to integrate for longer durations, our PEA can simply be repeated more times, and the results averaged to obtain the usual improvement $\sim 1/\sqrt{T}$ in Δb.

E.5 LOCK-IN MAGNETOMETER: MULTIPLE AC FREQUENCIES

Two different cases have been simulated. PEA lock-in performed on a shifted frequency relative to the lock-in frequency $f_0 = 20.83$ kHz is shown in Figure 48a. The shift is given as percentage of f_0. The field amplitude was set to $b_{ac}/b_{max} = 0.296$ while the phase $\theta = 0^0$. In

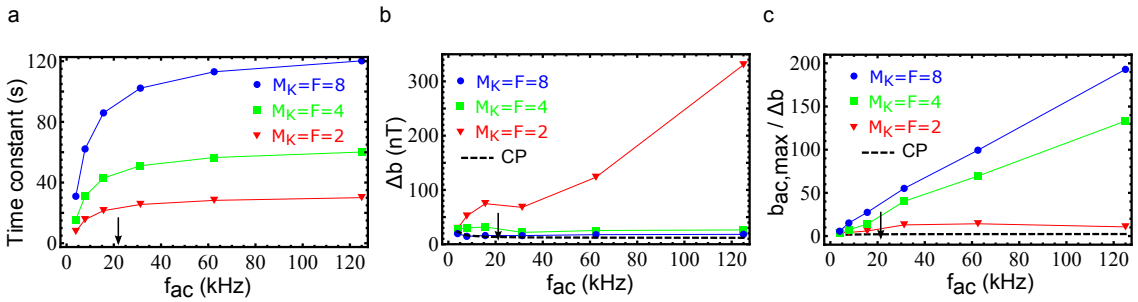

Figure 47: **PEA time constants**: **a**, The total time for the lock-in detection as a function of magnetic field frequency $f_{ac} = 1/\tau$. The parameter K is chosen such that the longest pulse sequence length is always the same (256 μs). **b**, Simulation of minimum detectable field amplitude difference $\Delta b = \pi\sigma_\phi/2\gamma_e\tau$ as a function of f_{ac} where σ_ϕ is the standard deviation of the simulated quantum phase readouts with measurement fidelity $\sim 93\%$ obtained from $R = 8000$ in our experiments. The black dashed line is the theoretical limit with multi-pulse CP $\Delta b = \eta/\sqrt{T}$ for the same experimental conditions. Here, η is obtained from Eq(5.8) while the total time for PEA with $M_K = F = 8$ is used for T. However note that the R=8000 is different from the actual experiments we carried out (R=15000) and also we have not taken into account the coherence enhancement due to DD in these simulations. Despite these differences, the simulation reasonably agrees with the experiments. **c**, Corresponding dynamic range defined by $b_{ac,max}/\Delta b$. Arrow shows the working point frequency (20.83 kHz) carried out in our experiments.

this condition, the Q-channel can detect a frequencies upto $\sim 4\%$ shift. Figure 48b shows the case of two different signals one with a shifted frequency while the other on lock-in frequency given by expression: $b_{ac}(\cos(2\pi f_0 t) + \cos(2\pi(f_0 + df_0)t))$ where df_0 is the frequency shift. The two in-phase signals with no frequency shift (0% shift) adds up to give a single signal with twice the amplitude. Further we can see from the figure that the Q channel clearly shows the shift in the quadrature phase ϕ_Q that is caused by the shifted frequency component.

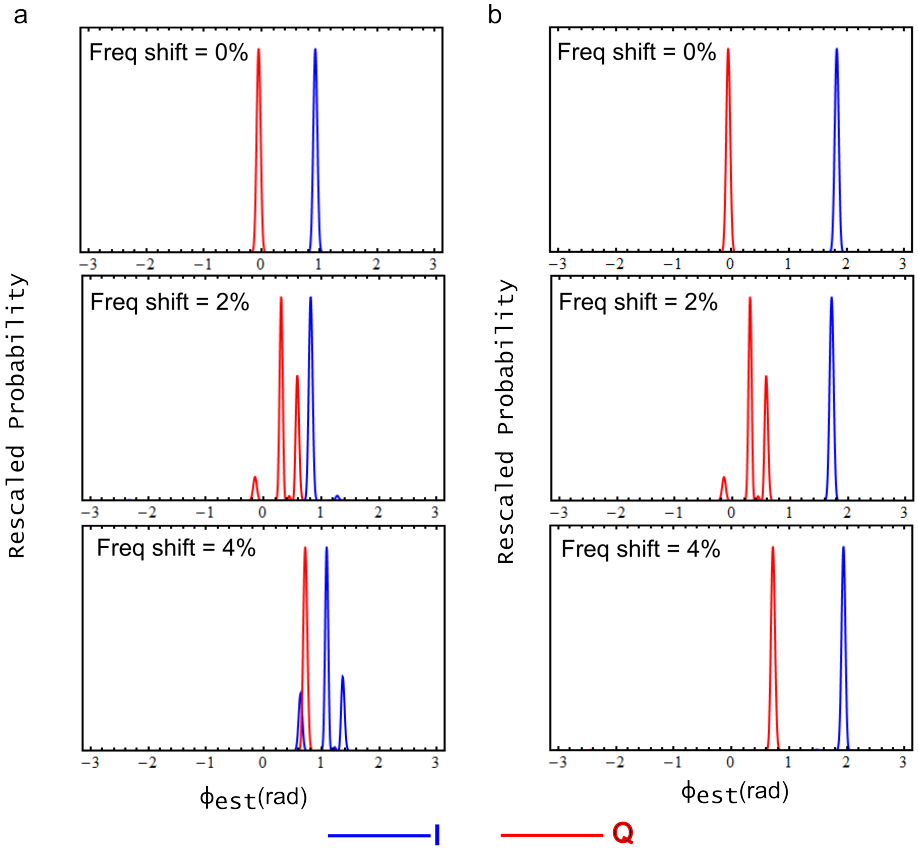

Figure 48: **Shifted frequency simulation**: **a**, The only signal is a shifted frequency relative to the lock-in frequency f_0=20.83 kHz. **b**, Two signals, one with a shifted frequency while the other on lock-in frequency. Blue (Red) curve plots the phase likelihood distribution obtained in I(Q) channel. All signals are set to $b_{ac}/b_{max} = 0.296$ and $\theta = 0^0$.

APPENDIX F

LIST OF INSTRUMENTS AND COMPONENTS

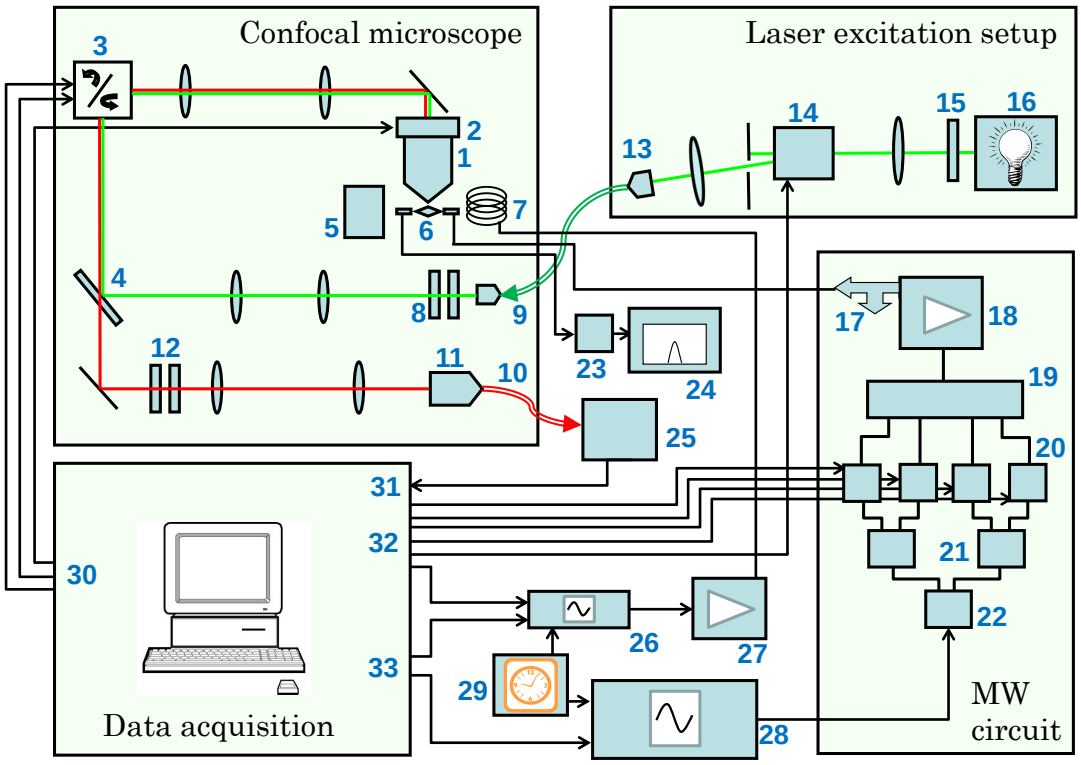

Figure 49: **Complete experimental apparatus:** The experimental apparatus consists of a confocal fluorescence microscope, the 532 nm laser excitation setup, the MW circuit, and the data acquisition system. Arrow heads indicate the direction of the signal flow. The labeled instruments/components in the figure are described in Table 5.

Figure 49 summarizes the complete apparatus for most of the experiments described in this thesis. Table 5 describe the instruments/components labeled in Figure 49. Note that during the course of research, some components (eg. the laser source) have been replaced few times and therefore the table may contain multiple choices for those entries. Furthermore, some labeled elements in the figure may represent a bunch of different components used either together or separately depending on the context. Other major instruments used but not shown in Figure 49, are listed in the end of the Table 5.

#	Component	Comments
1	OLYMPUS MPLAPON 50X	0.95 NA, 0.35 mm WD
	NIKON PlanApo 100X	1.4 NA, 0.13 mm WD
2	MADCITYLABS Nano-F100	Piezo, 100 μm range, closed-loop
3	CAMBRIDGE TECH. 6215H Optical Scanner	MicroMax 673 Driver Board
4	SEMROCK LPD01-532RS-25	RazorEdge Dichroic BS
5	K&J NdFeB Magnet	Grade N52
6	SUMITOMO $2 \times 2 \times 0.5$ single crystal diamond sample	Type IIa, [1 1 1] cut, double polished
	GOODFELLOW CU005171 Cu wire	20 μm diameter, 99.99% purity
7	Magnet coil	Home-made, 0.3 mH
8	$\lambda/2$-wave plate + Linear polarizer	Fine control of excitation power
9	THORLABS P3-460A-FC-1	Single mode fibre, 0.13 NA
10	THORLABS P5-630A-FC-1	Single mode fibre, 0.13 NA
	THORLABS P5-630A-PCAPC-1	Single mode fibre, 0.13 NA
	THORLABS M67L02	Multi mode fibre, 0.10 NA
	THORLABS M31L05	Multi mode fibre, 0.275 NA
11	OLYMPUS Plan N Achromat 10X	0.25 NA, 10.6 mm WD
12	SEMROCK LPD01-532RS-25	StopLine Notch Filter
	THORLABS FELH0650	Premium Long Pass
	THORLABS FES0800	Short Pass

#	Component	Comments
13	THORLABS F240APC-A THORLABS F240FC-A f	fibre coupler, 0.51 NA fibre coupler, 0.51 NA
14	NEOS 15210 AOM	Driver Model 21210-1DM
15	THORLABS ND Filters	OD 0.3, 0.5, 1, 2, 3
16	AIX-532-200 COHERENT COMPASS315M LASERGLOW LLS-0532-CFM	Nd:Yag doubled, 532 nm, IIIb TEM00
17	NARDA 4913 Isolator NARDA 4923 Circulator SONOMA SCIENTIFIC OFR27 C2XP4 09357 NARDA 374 NF Termination	2-4 GHz 2-4 GHz Circulator DC-12 GHz, 20 W
18	MINICIRCUITS ZHL-16W-43 OPHIR 58003084-28 MW Amp.	1.8-4 GHz, 16 W 0.5-3 GHz, 50 W
19	MINICIRCUITS ZN4PD1-50-S+ Power Combiner	0.5-5 GHZ
20	MINICIRCUITS ZASWA-2-50DR+ High Isolation Switch CMC CMCS0947A MW Switches	DC-5 GHz 0.1-12 GHz, switching speed 3 ns, transition time < 1 ns
21	MINICIRCUITS ZX10Q-2-19S+ Power Splitter MINICIRCUITS ZAPDJ-2-S Power Splitter	2-Way-90^0 , 1.1-1.9 GHz 2-Way-90^0 , 1-2 GHz
22	MINICIRCUITS ZAPDQ-2-S Power Splitter	2-Way-180^0 , 1-2 GHz
23	NARDA 766-10 Attenuator NARDA 25425 Directional Coupler	DC-4 GHz, 20 W 1-12.5 GHz, 20 dB

#	Component	Comments
	MINICIRCUITS VAT-20W2+ 20 dB Attenuator	DC-6 GHz, 2 W
	MINICIRCUITS BLK-89-S+	DC Block
	NARDA 4503A-03 Detector	0.01-18 GHz
24	AGILENT 8596E Spectrum Analyzer	9 kHz-12.8 GHz
25	PERKIN-ELMER SPCM-AQR-14-FC	Dark counts 53, pulse width 17 ns, dead time 30 ns
	MPD APD	Dark counts 13, pulse width 17 ns, dead time 79 ns
26	AGILENT 33250A AWG	80 MHz
	TEKTRONIX AFG3102 AWG	100 MHz
	SPINCORE DDS-II USB AWG	300 MHz
27	TECHRON 7541 Audio Amplifier	DC-30 kHz
28	HP 8350B Sweep Oscillator + HP 86235A plug-in	1.7-4.3 GHz
	ROHDE&SCHWARZ SMIQ03B Signal Generator	300 kHz - 3.3 GHz
29	SRS FS725 Rubedium Frequency Standard	5 MHz, 10 MHz reference clock
30	NI PCI-6229 DAQMx	Analogue outputs, counters etc.
31	NI PCI-6601	Counter board
32	SPINCORE PulseBlaster ESR-Pro	400 MHz, 2.5 ns time resolution
	ANDOR iDus DU401A-BV	Spectrometer camera
	PICOHARP PH300	Co-incident counter for the photon anti-bunching experiment
	HP 6621A DC Power Supply	Driving the Helmholtz coils for low magnetic fields

#	Component	Comments
	HP 8753D Network Analyzer	30 kHz - 6 GHz, Impedance measurement

Table 5: List of instruments and components

The specific wire configuration within our data acquisition system is listed below. The labels 'Dev1', 'Dev2', and 'PB' here refer to NI PCI-6229, NI PCI-6601, and SPINCORE ESR-Pro respectively.

SPCM $\longrightarrow$ Dev1 CTR0 source, Dev1 CTR1 source

Dev2 CTR0 out $\longrightarrow$ Dev1 PFI0

PB BNC 0-3 $\longrightarrow$ MW switch 1-4

PB 5 $\longrightarrow$ AOM Mod input

PB 6 $\longrightarrow$ Dev1 CTR0 gate (PFI9)

PB 7 $\longrightarrow$ Dev1 CTR1 gate (PFI4)

PB 8 $\longrightarrow$ Dev1 PO8

Dev1 AO0 $\longrightarrow$ CAMBRIDGE Scanner mirror Y channel

Dev1 AO1 $\longrightarrow$ CAMBRIDGE Scanner mirror X channel

Dev1 AO2 $\longrightarrow$ MADCITYLABS Piezo stage

Dev1 AO3 $\longrightarrow$ HP 8350B Sweep input

BIBLIOGRAPHY

[1] J. Bylander, S. Gustavsson, F. Yan, F. Yoshihara, K. Harrabi, G. Fitch, D. G. Cory, Y. Nakamura, J.-S. Tsai, and W. D. Oliver, Nat. Phys. **7**, 565 (2011).

[2] A. N. Vamivakas, Y. Zhao, S. Fält, A. Badolato, J. M. Taylor, and M. Atatüre, Phys. Rev. Lett. **107**, 166802 (2011).

[3] J. R. Maze, P. L. Stanwix, J. S. Hodges, S. Hong, J. M. Taylor, P. Cappellaro, L. Jiang, M. V. G. Dutt, E. Togan, A. S. Zibrov, A. Yacoby, R. L. Walsworth, and M. D. Lukin, Nature **455**, 644 (2008).

[4] J. M. Taylor, P. Cappellaro, L. Childress, L. Jiang, D. Budker, P. R. Hemmer, A. Yacoby, R. Walsworth, and M. D. Lukin, Nature Phys. **4**, 810 (2008).

[5] G. Balasubramanian, I. Y. Chan, R. Kolesov, M. Al-Hmoud, J. Tisler, C. Shin, C. Kim, A. Wojcik, P. R. Hemmer, A. Krueger, T. Hanke, A. Leitenstorfer, R. Bratschitsch, F. Jelezko, and J. Wrachtrup, Nature **455**, 648 (2008).

[6] F. Dolde, H. Fedder, M. W. Doherty, T. Nöbauer, F. Rempp, G. Balasubramanian, T. Wolf, F. Reinhard, L. C. L. Hollenberg, F. Jelezko, and J. Wrachtrup, Nature Physics **7**, 459 (2011).

[7] C. Bradac, T. Gaebel, N. Naidoo, M. J. Sellars, J. Twamley, L. J. Brown, A. S. Barnard, T. Plakhotnik, A. V. Zvyagin, and J. R. Rabeau, Nat Nano **5**, 345 (2010).

[8] G. Balasubramanian, P. Neumann, D. Twitchen, M. Markham, R. Kolesov, N. Mizuochi, J. Isoya, J. Achard, J. Beck, J. Tissler, V. Jacques, P. R. Hemmer, F. Jelezko, and J. Wrachtrup, Nature Mater. **8**, 383 (2009).

[9] C.-C. Fu, H.-Y. Lee, K. Chen, T.-S. Lim, H.-Y. Wu, P.-K. Lin, P.-K. Wei, P.-H. Tsao, H.-C. Chang, and W. Fann, Proc. Natl Acad. Sci. USA **104**, 727732 (2007).

[10] L. P. McGuinness, Y. Yan, A. Stacey, D. A. Simpson, T. L. Hall, D. Maclaurin, S. Prawer, P. Mulvaney, J. Wrachtrup, F. Caruso, E. R. Scholten, and L. C. L. Hollenberg, Nat Nano **6**, 358 (2011).

[11] F. Jelezko, T. Gaebel, I. Popa, M. Domhan, A. Gruber, and J. Wrachtrup, Phys. Rev. Lett. **93**, 130501 (2004).

[12] M. V. G. Dutt, L. Childress, L. Jiang, E. Togan, J. Maze, F. Jelezko, A. S. Zibrov, P. R. Hemmer, and M. D. Lukin, Science **316**, 1312 (2007).

[13] V. M. Acosta, E. Bauch, M. P. Ledbetter, A. Waxman, L.-S. Bouchard, and D. Budker, Phys. Rev. Lett. **104**, 070801 (2010).

[14] D. M. Toyli, C. F. de las Casas, D. J. Christle, V. V. Dobrovitski, and D. D. Awschalom, Proceedings of the National Academy of Sciences **110**, 8417 (2013).

[15] P. Neumann, I. Jakobi, F. Dolde, C. Burk, R. Reuter, G. Waldherr, J. Honert, T. Wolf, A. Brunner, J. H. Shim, D. Suter, H. Sumiya, J. Isoya, and J. Wrachtrup, Nano Letters **13**, 2738 (2013).

[16] N. M. Nusran, M. U. Momeen, and M. V. G. Dutt, Nature Nanotech. **7**, 109 (2012).

[17] M. S. Grinolds, S. Hong, P. Maletinsky, L. Luan, M. D. Lukin, R. L. Walsworth, and A. Yacoby, Nat Phys **9**, 215 (2013).

[18] S. Kotler, N. Akerman, Y. Glickman, A. Keselman, and R. Ozeri, Nature **473**, 61 (2011).

[19] G. de Lange, D. Ristè, V. V. Dobrovitski, and R. Hanson, Phys. Rev. Lett. **106**, 080802 (2011).

[20] B. Naydenov, F. Dolde, L. T. Hall, C. Shin, H. Fedder, L. C. L. Hollenberg, F. Jelezko, and J. Wrachtrup, Phys. Rev. B **83**, 081201 (2011).

[21] L. M. Pham, N. Bar-Gill, C. Belthangady, D. Le Sage, P. Cappellaro, M. D. Lukin, A. Yacoby, and R. L. Walsworth, Phys. Rev. B **86**, 045214 (2012).

[22] N. Bar-Gill, L. Pham, A. Jarmola, D. Budker, and R. Walsworth, Nat Commun **4**, 1743 (2013).

[23] A. Cooper, E. Magesan, H. N. Yum, and P. Cappellaro, Nat Commun **5**, (2014).

[24] B. Naydenov, R. Kolesov, A. Batalov, J. Meijer, S. Pezzagna, D. Rogalla, F. Jelezko, and J. Wrachtrup, Applied Physics Letters **95**, (2009).

[25] I. Aharonovich, J. C. Lee, A. P. Magyar, B. B. Buckley, C. G. Yale, D. D. Awschalom, and E. L. Hu, Advanced Materials **24**, OP54 (2012).

[26] K. Ohno, F. Joseph Heremans, L. C. Bassett, B. A. Myers, D. M. Toyli, A. C. Bleszynski Jayich, C. J. Palmstrm, and D. D. Awschalom, Applied Physics Letters **101**, (2012).

[27] L. M. Pham, N. Bar-Gill, D. Le Sage, C. Belthangady, A. Stacey, M. Markham, D. J. Twitchen, M. D. Lukin, and R. L. Walsworth, Phys. Rev. B **86**, 121202 (2012).

[28] D. Le Sage, L. M. Pham, N. Bar-Gill, C. Belthangady, M. D. Lukin, A. Yacoby, and R. L. Walsworth, Phys. Rev. B **85**, 121202 (2012).

[29] J. P. Hadden, J. P. Harrison, A. C. Stanley-Clarke, L. Marseglia, Y.-L. D. Ho, B. R. Patton, J. L. O?Brien, and J. G. Rarity, Applied Physics Letters **97**, (2010).

[30] P. Siyushev, F. Kaiser, V. Jacques, I. Gerhardt, S. Bischof, H. Fedder, J. Dodson, M. Markham, D. Twitchen, F. Jelezko, and J. Wrachtrup, Applied Physics Letters **97**, (2010).

[31] L. Marseglia, J. P. Hadden, A. C. Stanley-Clarke, J. P. Harrison, B. Patton, Y.-L. D. Ho, B. Naydenov, F. Jelezko, J. Meijer, P. R. Dolan, J. M. Smith, J. G. Rarity, and J. L. O'Brien, Applied Physics Letters **98**, (2011).

[32] B. J. Hausmann, M. Khan, Y. Zhang, T. M. Babinec, K. Martinick, M. McCutcheon, P. R. Hemmer, and M. Loncar, Diamond and Related Materials **19**, 621 (2010).

[33] T. Babinec, B. Hausmann, M. Khan, Y. Zhang, J. Maze, P. Hemmer, and M. Loncar, Nature Nanotech. **5**, 195 (2010).

[34] B. J. M. Hausmann, T. M. Babinec, J. T. Choy, J. S. Hodges, S. Hong, I. Bulu, A. Yacoby, M. D. Lukin, and M. Loncar, New Journal of Physics **13**, 045004 (2011).

[35] J. T. Choy, B. J. M. Hausmann, T. M. Babinec, I. Bulu, M. Khan, P. Maletinsky, A. Yacoby, and M. Loncar, Nat Photon **5**, 738 (2011).

[36] S. Hong, M. S. Grinolds, L. M. Pham, D. Le Sage, L. Luan, R. L. Walsworth, and A. Yacoby, MRS Bulletin **38**, 155 (2013).

[37] P. Maletinsky, S. Hong, M. S. Grinolds, B. Hausmann, M. D. Lukin, R. L. L., Walsworth, M. Loncar, and A. Yacoby, Nat Nano **7**, 320 (2012).

[38] L. Rondin, J.-P. Tetienne, P. Spinicelli, C. Dal Savio, K. Karrai, G. Dantelle, A. Thiaville, S. Rohart, J.-F. Roch, and V. Jacques, Applied Physics Letters **100**, (2012).

[39] M. S. Grinolds, M. Warner, K. D. Greve, Y. Dovzhenko, L. Thiel, R. L. Walsworth, S. Hong, P. Maletinsky, and A. Yacoby, Nat Nano (2014).

[40] H. J. Mamin, M. Kim, M. H. Sherwood, C. T. Rettner, K. Ohno, D. D. Awschalom, and D. Rugar, Science **339**, 557 (2013).

[41] T. Staudacher, F. Shi, S. Pezzagna, J. Meijer, J. Du, C. A. Meriles, F. Reinhard, and J. Wrachtrup, Science **339**, 561 (2013).

[42] D. Le Sage, K. Arai, D. R. Glenn, S. J. DeVience, L. M. Pham, L. Rahn-Lee, M. D. Lukin, A. Yacoby, A. Komeili, and R. L. Walsworth, Nature **496**, 486 (2013).

[43] L. M. Pham, D. L. Sage, P. L. Stanwix, T. K. Yeung, D. Glenn, A. Trifonov, P. Cappellaro, P. R. Hemmer, M. D. Lukin, H. Park, A. Yacoby, and R. L. Walsworth, New Journal of Physics **13**, 045021 (2011).

[44] L. Rondin, J. P. Tetienne, S. Rohart, A. Thiaville, T. Hingant, P. Spinicelli, J. F. Roch, and V. Jacques, Nat Commun **4**, (2013).

[45] D. Budker and M. Romalis, Nature Phys. **3**, 227234 (2007).

[46] R. S. Schoenfeld and W. Harneit, Phys. Rev. Lett. **106**, 030802 (2011).

[47] N. M. Nusran and M. V. G. Dutt, Phys. Rev. B **88**, 220410 (2013).

[48] N. M. Nusran and M. V. G. Dutt, http://arxiv.org/abs/1403.4506 (To be published).

[49] V. Shah, S. Knappe, P. D. D. Schwindt, and J. Kitching, Nat Photon **1**, 649 (2007).

[50] V. Shah, G. Vasilakis, and M. V. Romalis, Phys. Rev. Lett. **104**, 013601 (2010).

[51] D. Sheng, S. Li, N. Dural, and M. V. Romalis, Phys. Rev. Lett. **110**, 160802 (2013).

[52] J. Sinha, S. Mohan, S. S. Banerjee, S. Kahaly, and G. R. Kumar, Phys. Rev. E **77**, 046118 (2008).

[53] T. Sebastian, A. Conca, G. Wolf, H. Schultheiss, B. Leven, and B. Hillebrands, Journal of Applied Physics **110**, (2011).

[54] J. Zweck, M. Schneider, M. Sessner, T. Uhlig, and M. Heumann, in *Advances in Solid State Physics*, Vol. 41 of *Advances in Solid State Physics Volume 41*, edited by B. Kramer (Springer Berlin Heidelberg, New York, 2001), pp. 533–545.

[55] S. Gusev, V. Petrov, and E. Skorokhodov, Journal of Surface Investigation. X-ray, Synchrotron and Neutron Techniques **4**, 582 (2010).

[56] R. M. Reeve, C. Mix, M. Knig, M. Foerster, G. Jakob, and M. Klui, Applied Physics Letters **102**, (2013).

[57] J. Cumings, E. Olsson, A. K. Petford-Long, and Y. Zhu, MRS Bulletin **33**, 101 (2008).

[58] M. Tanase and A. K. Petford-Long, Microscopy Research and Technique **72**, 187 (2009).

[59] C. Degen, Nature Nanotech. **3**, 643 (2008).

[60] J. R. Kirtley, M. B. Ketchen, K. G. Stawiasz, J. Z. Sun, W. J. Gallagher, S. H. Blanton, and S. J. Wind, Applied Physics Letters **66**, 1138 (1995).

[61] B. W. Gardner, J. C. Wynn, P. G. Bjrnsson, E. W. J. Straver, K. A. Moler, J. R. Kirtley, and M. B. Ketchen, Review of Scientific Instruments **72**, 2361 (2001).

[62] M. E. Huber, N. C. Koshnick, H. Bluhm, L. J. Archuleta, T. Azua, P. G. Bjornsson, B. W. Gardner, S. T. Halloran, E. A. Lucero, and K. A. Moler, Rev Sci Instrum **79**, 053704 (2008).

[63] A. Finkler, Y. Segev, Y. Myasoedov, M. L. Rappaport, L. Ne?eman, D. Vasyukov, E. Zeldov, M. E. Huber, J. Martin, and A. Yacoby, Nano Letters **10**, 1046 (2010).

[64] G. Boero, M. Demierre, P. A. Besse, and R. S. Popovic, Sensors and Actuators A: Physical **106**, 314 (2003).

[65] J. A. Sidles, J. L. Garbinin, K. J. Bruland, D. Rugar, O. Zuger, S. Hoen, and C. S. Yannoni, Rev. Mod. Phys. **67**, 249 (1995).

[66] D. Rugar, R. Budakian, H. J. Mamin, and B. W. Chui, Nature **430**, 329332 (2004).

[67] H. J. Mamin, T. H. Oosterkamp, M. Poggio, C. L. Degen, C. T. Rettner, and D. Rugar, Nano Letters **9**, 3020 (2009).

[68] A. Vinante, G. Wijts, O. Usenko, L. Schinkelshoek, and T. Oosterkamp, Nat Commun **2**, 572 (2011).

[69] N. B. Manson, J. P. Harrison, and M. J. Sellars, Phys. Rev. B **74**, 104303 (2006).

[70] M. W. Doherty, N. B. Manson, P. Delaney, and L. C. L. Hollenberg, New Journal of Physics **13**, 025019 (2011).

[71] M. W. Doherty, F. Dolde, H. Fedder, F. Jelezko, J. Wrachtrup, N. B. Manson, and L. C. L. Hollenberg, Phys. Rev. B **85**, 205203 (2012).

[72] M. W. Doherty, N. B. Manson, P. Delaney, F. Jelezko, J. Wrachtrup, and L. C. Hollenberg, Physics Reports **528**, 1 (2013).

[73] A. Gali, M. Fyta, and E. Kaxiras, Phys. Rev. B **77**, 155206 (2008).

[74] L. Childress, J. Taylor, A. Sørensen, and M. Lukin, Phys. Rev. Lett. **96**, 070504 (2006).

[75] B. E. A. Saleh and M. C. Teich, *FUNDEMENTALS OF PHOTONICS* (Wiley, New Jersey, 2007).

[76] R. H. Webb, Rep. Prog. Phys. **59**, 427 (1996).

[77] *Introductory Quantum Optics*, edited by C. C. Gerry and P. L. Knight (Cambridge University Press, Cambridge, 2005).

[78] B. Smeltzer, J. McIntyre, and L. Childress, Phys. Rev. A **80**, 050302 (2009).

[79] S. Felton, A. M. Edmonds, M. E. Newton, P. M. Martineau, D. Fisher, D. J. Twitchen, and J. M. Baker, Phys. Rev. B **79**, 075203 (2009).

[80] G. D. Fuchs, V. V. Dobrovitski, R. Hanson, A. Batra, C. D. Weis, T. Schenkel, and D. D. Awschalom, Phys. Rev. Lett. **101**, 117601 (2008).

[81] P. Neumann, R. Kolesov, V. Jacques, J. Beck, J. Tisler, A. Batalov, L. Rogers, N. B. Manson, G. Balasubramanian, F. Jelezko, and J. Wrachtrup, New Journal of Physics **11**, 013017 (2009).

[82] V. Jacques, P. Neumann, J. Beck, M. Markham, D. Twitchen, J. Meijer, F. Kaiser, G. Balasubramanian, F. Jelezko, and J. Wrachtrup, Phys. Rev. Lett. **102**, 057403 (2009).

[83] L. Jiang, J. S. Hodges, J. R. Maze, P. Maurer, J. M. Taylor, D. G. Cory, P. R. Hemmer, R. L. Walsworth, A. Yacoby, A. S. Zibrov, and M. D. Lukin, Science **326**, 267 (2009).

[84] P. Neumann, R. Kolesov, B. Naydenov, J. Beck, F. Rempp, M. Steiner, V. Jacques, G. Balasubramanian, M. L. Markham, D. J. Twitchen, S. Pezzagna, J. Meijer, J. Twamley, F. Jelezko, and J. Wrachtrup, Nature Physics **6**, 249 (2010).

[85] A. Y. Kitaev, Electr. Coll. Comput. Complex. **3**, (1996).

[86] B. L. Higgins, D. W. Berry, S. D. Bartlett, H. M. Wiseman, and G. J. Pryde, Nature **450**, 393 (2007).

[87] R. Griffiths and C.-S. Niu, Phys. Rev. Lett. **98**, (2007).

[88] R. S. Said, D. W. Berry, and J. Twamley, Phys. Rev. B **83**, 125410 (2011).

[89] B. L. Higgins, D. W. Berry, S. D. Bartlett, M. W. Mitchell, H. M. Wiseman, and G. J. Pryde, New J. Phys. **11**, 073023 (2009).

[90] D. W. Berry, B. L. Higgins, S. D. Bartlett, M. W. Mitchell, G. J. Pryde, and H. M. Wiseman, Phys. Rev. A **80**, 052114 (2009).

[91] R. Cleve, A. Ekert, C. Macchiavello, and M. Mosca, Proceedings of the Royal Society of London. Series A: Mathematical, Physical and Engineering Sciences **454**, 339 (1998).

[92] B. Yurke, S. L. McCall, and J. R. Klauder, Phys. Rev. A **33**, 4033 (1986).

[93] S. F. Huelga, C. Macchiavello, T. Pellizzari, A. K. Ekert, M. B. Plenio, and J. I. Cirac, Phys. Rev. Lett. **79**, 3865 (1997).

[94] V. Giovannetti, S. Lloyd, and L. Maccone, Science **306**, 1330 (2004).

[95] V. Giovannetti, S. Lloyd, and L. Maccone, Phys. Rev. Lett. **96**, 010401 (2006).

[96] S. Massar and S. Popescu, Phys. Rev. Lett. **74**, 1259 (1995).

[97] C. A. Meriles, L. Jiang, G. Goldstein, J. S. Hodges, J. Maze, M. D. Lukin, and P. Cappellaro, The Journal of Chemical Physics **133**, (2010).

[98] T. Häberle, D. Schmid-Lorch, K. Karrai, F. Reinhard, and J. Wrachtrup, Phys. Rev. Lett. **111**, 170801 (2013).

[99] G. Giedke, J. M. Taylor, D. D'Alessandro, M. D. Lukin, and A. Imamoğlu, Phys. Rev. A **74**, 032316 (2006).

[100] D. W. Berry and H. M. Wiseman, Phys. Rev. Lett. **85**, 5098 (2000).

[101] J. Tuorila, M. Silveri, M. Sillanpää, E. Thuneberg, Y. Makhlin, and P. Hakonen, Phys. Rev. Lett. **105**, 257003 (2010).

[102] G. D. Fuchs, V. V. Dobrovitski, D. M. Toyli, F. J. Heremans, and D. D. Awschalom, Science **326**, 1520 (2009).

[103] W. M. Itano, J. C. Bergquist, J. J. Bollinger, J. M. Gilligan, D. J. Heinzen, F. L. Moore, M. G. Raizen, and D. J. Wineland, Phys. Rev. A **47**, 3554 (1993).

[104] D. J. Wineland, J. J. Bollinger, W. M. Itano, F. L. Moore, and D. J. Heinzen, Phys. Rev. A **46**, R6797 (1992).

[105] L. Childress, M. V. G. Dutt, J. M. Taylor, A. S. Zibrov, F. Jelezko, J. Wrachtrup, P. R. Hemmer, and M. D. Lukin, Science **314**, 281 (2006).

[106] V. Giovannetti, S. Lloyd, and L. Maccone, Nature Photon. **5**, 222 (2011).

[107] M. S. Grinolds, P. Maletinsky, S. Hong, M. D. Lukin, R. L. Walsworth, and A. Yacoby, Nature Phys. **7**, 687 (2011).

[108] L. Jiang, J. S. Hodges, J. R. Maze, P. Maurer, J. M. Taylor, D. G. Cory, P. R. Hemmer, R. L. Walsworth, A. Yacoby, A. S. Zibrov, and M. D. Lukin, Science **326**, 267 (2009).

[109] G. de Lange, Z. H. Wang, D. Ristè, V. V. Dobrovitski, and R. Hanson, Science **330**, 60 (2010).

[110] C. A. Ryan, J. S. Hodges, and D. G. Cory, Phys. Rev. Lett. **105**, 200402 (2010).

[111] W. H. Zurek, Rev. Mod. Phys. **75**, 715 (2003).

[112] *The physics of quantum information: quantum cryptography, quantum teleportation, quantum computation*, edited by D. Bouwmeester, A. K. Ekert, and A. Zeilinger (Springer-Verlag, New York, 2000).

[113] J. R. Lakowicz, *Principles of Fluorescence Spectroscopy* (Springer, New York, 2006), pp. 157 – 204.

[114] W. B. Mims, K. Nassau, and J. D. McGee, Phys. Rev. **123**, 2059 (1961).

[115] J. R. Klauder and P. W. Anderson, Phys. Rev. **125**, 912 (1962).

[116] M. Poggio and C. L. Degen, Nanotechnology **21**, 342001 (2010).

[117] A. Laraoui, J. S. Hodges, and C. A. Meriles, Applied Physics Letters **97**, 143104 (2010).

[118] C. L. Degen, M. Poggio, H. J. Mamin, and D. Rugar, Phys. Rev. Lett. **99**, 250601 (2007).

[119] N. Zhao, J. Honert, B. Schmid, M. Klas, J. Isoya, M. Markham, D. Twitchen, F. Jelezko, R.-B. Liu, H. Fedder, and J. Wrachtrup, Nat Nano **7**, 657 (2012).

[120] T. H. Taminiau, J. J. T. Wagenaar, T. van der Sar, F. Jelezko, V. V. Dobrovitski, and R. Hanson, Phys. Rev. Lett. **109**, 137602 (2012).

[121] S. Kolkowitz, Q. P. Unterreithmeier, S. D. Bennett, and M. D. Lukin, Phys. Rev. Lett. **109**, 137601 (2012).

[122] G. Waldherr, J. Beck, P. Neumann, R. S. Said, M. Nitsche, M. L. Markham, D. J. Twitchen, J. Twamley, F. Jelezko, and J. Wrachtrup, Nat Nano **7**, 105 (2012).

[123] T. Farrar, S. Druck, R. R. Shoup, and E. D. Becker, Journal of the American Chemical Society **94**, 699 (1972).

[124] M. Tinkham, *Group Theory and Quantum Mechanics* (Dover, New York, 2003).

[125] J. R. Maze, A. Gali, E. Togan, Y. Chu, A. Trifonov, E. Kaxiras, and M. D. Lukin, New Journal of Physics **13**, 025025 (2011).

[126] L. J. Rogers, R. L. McMurtrie, M. J. Sellars, and N. B. Manson, New Journal of Physics **11**, 063007 (2009).

[127] A. Batalov, V. Jacques, F. Kaiser, P. Siyushev, P. Neumann, L. J. Rogers, R. L. McMurtrie, N. B. Manson, F. Jelezko, and J. Wrachtrup, Phys. Rev. Lett. **102**, 195506 (2009).

[128] K.-M. C. Fu, C. Santori, P. E. Barclay, L. J. Rogers, N. B. Manson, and R. G. Beausoleil, Phys. Rev. Lett. **103**, 256404 (2009).

[129] L. I. Childress, Ph.D. thesis, Harvard University Cambridge, 2007.

[130] V. M. Acosta, Ph.D. thesis, University of California Berkeley, 2011.

[131] *NEOS AOM 15210 Operating Manual*.

[132] *PulseBlasterESR-Pro Owner's Manual*.

[133] H. Varian, The Mathematica Journal **9**, (2005).

[134] L. Robledo, L. Childress, H. Bernien, B. Hensen, P. F. A. Alkemade, and R. Hanson, Nature **477**, 574578 (2011).